

A Numerical and Experimental Study of a Two-Stage Microwave Electrothermal Thruster for Spacecraft Propulsion

Vincent P. Chiravalle

**A DISSERTATION
PRESENTED TO THE FACULTY
OF PRINCETON UNIVERSITY
IN CANDIDACY FOR THE DEGREE
OF DOCTOR OF PHILOSOPHY**

**RECOMMENDED FOR ACCEPTANCE
BY THE DEPARTMENT OF
MECHANICAL AND AEROSPACE ENGINEERING**

June, 2003

A Numerical and Experimental Study of a Two-Stage Microwave Electrothermal Thruster for Spacecraft Propulsion

Prepared by:

Vincent P. Chiravalle

Approved by:

Professor Richard B. Miles
Dissertation Advisor

Professor Edgar Y. Choueiri
Dissertation Advisor

Professor Alexander Smits
Dissertation Reader

Professor Szymon Suckewer
Dissertation Reader

© Copyright by Vincent P. Chiravalle, 2003. All rights reserved.

Abstract

Radiative energy absorption and deposition and their impact on the internal flow properties of an experimental two-stage microwave electrothermal thruster (MET), which incorporates a novel supersonic energy addition stage, are investigated numerically and experimentally. For the first time supersonic energy addition involving a microwave-sustained plasma is demonstrated in a thruster geometry. Laser induced fluorescence (LIF) is used to make measurements of temperature and velocity in the exhaust plume of this thruster, running on argon, with and without the supersonic energy addition. For the case without supersonic energy addition LIF measurements in the plume reveal much lower than expected temperatures, suggesting that heat transfer to the thruster wall is an important process in the overall energy balance. LIF measurements with supersonic energy addition suggest that most of the supersonic energy addition is deposited in the laminar boundary layer as explained by a numerical simulation.

A numerical model is created to simulate microwave-sustained discharges in helium and argon. This numerical model includes equations for the components of the electric field inside the thruster, and the Navier-Stokes equations for the case of distinct electron and heavy species temperatures with finite rate ionization and excitation kinetics. Numerical simulations of two single-stage METs, running on helium, are performed representing vastly different operating regimes, and the results are compared with existing thrust data in both cases.

The calculations for the single-stage thrusters suggest that the electron and heavy particle temperatures in the plenum are not the same, even in case where the pressure exceeds several hundred Torr. In addition the measured values of electron temperature in this kind of discharge compare well with the predictions from the model. The computed gas temperature and electron number density profiles inside the plenum of these thrusters are relatively flat, and this result is contrasted with the predictions from a previous equilibrium model. The present model also predicts that the concentrations of excited state species, including the metastable states, are localized on the centerline as suggested by experimental observations, and these concentrations differ significantly from those that would exist if a Boltzmann equilibrium were maintained among the different excited states.

Acknowledgments

During my years here as a graduate student there have been many people who have helped me, fellow graduate students, members of the technical staff, research staff members, and professors, who have helped to make my time at Princeton a rich and rewarding experience. Among these people there are a few who I would like to mention here and thank for their encouragement and support.

First I would like to thank my advisor, Professor Richard B. Miles. Dick you made it possible for me to pursue my research interests and goals especially during the last three years. I will always be indebted to you for your guidance and support at a critical time in my life. You shared with me the trials and triumphs of doing research, and aligning the Ti: Sapphire laser. You are the master of your field, and knowing that I had your support meant a great deal to me. I'm glad I had a chance to work closely with you, and be part of your group, the Applied Physics Group.

I would like to thank Professor Edgar Choueiri who was also my advisor for many years. Eddie, I appreciate your efforts to help me over the many years that we worked together. With your help I was able to accomplish many things. It was a rewarding trip, and there were many positive experiences which I will take with me. It was a thrill to be a part of your lab, working on something as exciting as electric propulsion.

I would like to thank Sohail Zaidi, a research scientist in the Applied Physics Group, who spent much time with me helping me collect the LIF data for this thesis. Sohail, I was fortunate that you were there with me during the long hours and many frustrations that my experimental work entailed. I learned from your patience and persistence, and I found your encouragement and helpful advice to be essential.

I would like to thank Glen Northey, the senior technical staff person who runs the MAE machine shop. Glen helped me with many of the machining and construction tasks for my project, during the numerous weeks that I was working in the shop. It was a pleasure to learn from you, Glen, because you have an enthusiasm for your work and you are a great teacher.

Finally I would like to thank, most of all, my mom, Marie T. Chiravalle. None of what I have done would have been possible without you. Mom, you are a model parent, and the personification of self-sacrifice and courage. I hope that one day I will be only half as good a parent as you are.

This dissertation carries the designation 3113-T in the records of the Department of Mechanical and Aerospace Engineering.

Contents

Abstract	i
Acknowledgments	ii
Table of Contents	iii
List of Symbols	v
1 Introduction	1
1.1 Previous Experimental Work with the Single-Stage MET	4
1.2 Microwave Discharge Models	5
1.3 Potential Role and Limitations of the Single-Stage MET	7
1.4 Two-Stage MET	8
1.5 Dissertation Objectives	9
1.6 Dissertation Outline	12
2 Two-Stage Microwave Thruster Design	13
2.1 Modes in a Cylindrical Cavity	14
2.2 Subsonic Stage	17
2.3 Supersonic Stage	20
3 Physical Model	25
3.1 Gas Dynamics Model	26
3.1.1 Numerical Formulation	29
3.1.2 Boundary Conditions	31
3.2 Plasma Model	32
3.2.1 Electron Loss Mechanisms	33
3.2.2 Electron EEDF	37
3.2.3 Plasma Model for Helium	39
3.2.4 Plasma Model for Argon	40
3.2.5 Rate Coefficients	41
3.3 Transport Properties	44
3.4 Microwave Field Model	45
3.4.1 Finite-Element Technique	46
3.4.2 Boundary Conditions	48
3.5 Validation of the Fluid Solver	51

3.5.1	Conical Flow	51
3.5.2	Compressible Boundary Layers	54
3.6	Validation of the Microwave Field Solver	61
4	Model Comparison with MET Thrust Data	65
4.1	Simulation of 1 kW MET	66
4.1.1	1 kW Thruster Grid	66
4.1.2	Boundary Conditions	67
4.1.3	Simulation Results	70
4.1.4	Comparison with Equilibrium Model	81
4.1.5	Comparison with Thrust Data	82
4.2	100 W MET Simulation	84
4.2.1	Simulation Results	85
4.2.2	Comparison with Thrust Data	95
4.3	Mass Conservation	98
4.4	Summary of Model Performance	100
5	LIF Spectroscopy	102
5.1	LIF History	102
5.2	Experimental Setup	103
5.3	LIF Theory	106
5.4	Ti:Sapphire Laser System	108
6	LIF Data and Model Predictions	111
6.1	Two-Stage Thruster with Subsonic Energy Addition	112
6.1.1	LIF Measurements	113
6.1.2	Comparison with Fluid Simulation	116
6.2	Detailed Simulation of Two-Stage Thruster with Subsonic Energy Addition	120
6.2.1	Simulation Results	121
6.3	Two-Stage Thruster with Supersonic Energy Addition	127
6.3.1	LIF Measurements	127
6.3.2	Comparison with Fluid Simulation	130
6.4	Conclusions from LIF Measurements and Model Predictions	133
7	Conclusions	137
A	Overview of Electric Propulsion	141
A.1	Arcjet	142
A.2	Ion Engine	143
A.3	Hall Thruster	145
A.4	Solar Power Technology	147

A.5 Space-Based Nuclear Reactors	149
B Orbit-Raising Mission Example	152
Bibliography	158

List of Symbols

A_{mn}	Spontaneous emission rate from level m to n
A^+	Complex amplitude coefficient at the microwave inlet port
$B_{m,n}^{i,j}$	Contribution to the finite-element matrix from element (i, j)
CFL	CFL number
c_v	The specific heat at constant volume
$D^{i,j+1/2}$	The numerical approximation to the physical dissipative flux on the right-hand side of cell i, j
e	The charge of an electron
E_e	Internal energy density of electrons
E_h	Total internal energy density of heavy particles
\mathbf{E}_r	Radial component of the complex electric field
\mathbf{E}_z	Axial component of the complex electric field
f	Blasius solution for velocity profile in boundary layer above a flat plate
\mathbf{F}_c	Vector of convective fluxes in the axial direction
\mathbf{F}_d	Vector of physical dissipation fluxes in axial direction
$F^{i+1/2,j}$	The numerical approximation to the convective flux on the right-hand side of cell i, j
\mathbf{G}_c	Vector of convective fluxes in the radial direction
\mathbf{G}_d	Vector of physical dissipation fluxes in axial direction
G_e	The product of the universal gravitational constant and the mass of the earth
g_n	Degeneracy of level n
g_0	Gravitational constant at the surface of the earth, 9.81 m/s^2
$H^{i,j}$	Area of cell i, j
I_{sp}	Specific impulse of a rocket engine
J	Microwave joule heating rate
J_m	Bessel function of order m
k_b	The Boltzmann constant
k_h	Thermal conductivity of the heavy particles
L	Resonant length of a cylindral microwave cavity
M	Total instantaneous mass of a spacecraft
m_e	The mass of an electron
M_e	Mass of a space electric power system

M_f	Total propellant mass
M_p	Payload mass
M_s	Structural mass of the propellant tanks
M_0	Total initial mass of a spacecraft
\hat{n}	Unit vector normal to a boundary
N_A	Number density of atoms
N_e	Electron number density
P	Total gas pressure ($P_h + P_e$)
P_e	Electron pressure
P_h	Heavy particle pressure
Q_{elas}	Elastic energy transfer rate between heavy particles and electrons
q_{hr}	Component of the heavy particle heat flux vector
q_{hx}	Component of the heavy particle heat flux vector
Q_{in}	Inelastic energy transfer rate between heavy particles and electrons
R_i	Gas constant for species i
$R^{i,j}$	Total residual for cell i, j
S_n	Ionization rate coefficient from level n
β_n	Three-body recombination rate coefficient back to level n
S_{nm}^I	Excitation rate coefficient from level n to level m
S_{mn}^{II}	Relaxation rate coefficient from level m to level n
T	Temperature of heavy particles
T_e	Electron temperature
T_w	Temperature on the surface of the flat plate
T_0	Stagnation temperature
T_1	Free stream temperature
T_{θ}	Constant thrust level in the $\hat{\theta}$ direction
\mathbf{U}	Vector of flow conservation variables
u	Axial component of flow velocity
v	Radial component of flow velocity
\bar{v}_r	Average radial velocity of the flow

\bar{v}_z	Average axial velocity of the flow
v_ϕ	Component of the average flow velocity in the direction of the laser beam
w_i	Molecular weight of species i
X	Reflection coefficient at the microwave inlet port
x_i	The mole fraction of species i
Z_L	The resistive part of the loop antenna impedance
Z_0	Characteristic impedance of a coaxial waveguide
α	Specific power of a space electric power supply
α_1	Numerical dissipation coefficient
α_2	Numerical dissipation coefficient
β	The complex propagation constant
β_s	Oblique shock angle
γ	Ratio of specific heats
Δd	Change in the spacing between the etalon mirrors
Δf	Change in etalon transmission frequency
ΔH_i	Enthalpy of formation for species i
$\Delta r^{i+1/2,j}$	The change in r along the right hand side of cell i, j
$\Delta t^{i,j}$	Time step size for cell i, j
ΔV	Velocity increment for an orbit raising maneuver
$\Delta x^{i+1/2,j}$	The change in x along the right hand side of cell i, j
$\Delta \epsilon_{mn}$	Difference in energy between levels m and n
$\Delta \nu$	Laser linewidth
ϵ	The permittivity of a medium
ϵ_0	Permittivity of free space
η	Non-dimensional distance above the flat plate for a compressible boundary layer
η^*	Non-dimensional distance above the flat plate for an incompressible boundary layer
θ_c	Cone half angle
λ	Laser wavelength
Λ	The Coulomb logarithm
λ_g	The guide wavelength as defined in Eqn. 2.4

λ_r	Spectral radius in the radial direction
λ_x	Spectral radius in the axial direction
μ	The permeability of a medium
μ_h	Viscosity of the heavy particles
ν_{eH}	Total energy-averaged momentum transfer collision frequency between electrons and heavy particles
ν_L	Laser frequency
ν_0	Frequency of a transition line
ρ_i	Mass density of species i
σ	Complex electrical conductivity
τ_{rr}	Component of the shear stress tensor
τ_{xr}	Component of the shear stress tensor
τ_{xx}	Component of the shear stress tensor
ψ_k	Influence function associated with point x_k, x_r
ω	The angular frequency of the microwave field
Ω_i	Rate of mass production of species i due to ionization and excitation reactions
$\Omega^{(2,2)}$	A collision integral used in transport calculations

Chapter 1

Introduction

Over the past thirty years, the number of satellites orbiting the earth has increased dramatically, from a handful in 1970 to almost a thousand at the turn of the century. In particular, large spacecraft have been placed in geo-stationary orbits by government and private institutions around the world. These satellites are used for communication, observation and navigation to such a degree that national security, and many functions of the world economy would suffer greatly with the sudden loss of these space assets. In the decades to come even more significant assets will be placed in space, which could possibly include laser weapons and radar systems, linked together by large communication satellites in geo-stationary orbit, for the purpose of ballistic missile defense, and interplanetary spacecraft, for return trips to the moon and missions to Mars. The cost of such endeavors will depend to a great degree on the propulsion systems used to place these payloads into the proper orbit. There are two parts to this equation, the rocket booster, which puts the payload into low-earth orbit, and the upper stage, which moves the payload from low-earth orbit (LEO) into the final orbit, a geo-stationary orbit (GEO) or another (sun synchronous etc).

Consider, for a moment, the cost associated with two contemporary launch vehicles, the Space Shuttle [1], which is used exclusively for civilian space projects such as construction of the International Space Station, and the Titan IVB rocket [2], which launches military satellites into geo-stationary orbit. The Shuttle costs roughly \$350 million dollars to launch and can place a maximum of 54,000 lbs of payload into low earth orbit. If the maximum payload capability is utilized, than the launch cost per pound using the Shuttle would be roughly \$6,500, in year 2002 dollars. The Titan IVB can launch 48,000 lbs into low earth orbit at a cost of roughly \$300 million dollars. The cost per pound for a launch using the Titan IVB is slightly less than the Shuttle, \$6,250. These estimates assume that both of these vehicles are launched from the Kennedy Space Center in Florida, due east into a 28.5 degree inclination orbit. One way to reduce the overall cost of the futuristic missions, described above, would be to develop new rocket boosters that reduce the cost

launching payloads into low-earth orbit. New rocket boosters could be totally reusable, such a next generation Space Shuttle [1], or they could be expendable, but much cheaper to manufacture than existing expendable rockets [3]. Another approach would be to reduce the mass of the upper stage propulsion system, by using an advanced propulsion system for the upper stage, something other than a chemical rocket.

All spacecraft require a means of imparting motion, an engine that accelerates the spacecraft to high velocity. Rocket engines provide acceleration by expelling propellant mass opposite the direction in which the rocket is traveling. The amount of mass, which needs to be expended for a given mission, is a strong function of the exhaust velocity of the rocket engine. Rocket engines are characterized in terms of specific impulse, which is the thrust of the rocket divided by the mass flow rate of propellant and the gravitational constant at the surface of the earth, $g_0 = 9.8 \text{ m/sec}^2$. Chemical combustion rockets, such as the Space Shuttle and the Titan IVB, have a specific impulse which is no greater than 450 sec. This represents an intrinsic limit on the specific impulse attainable by chemical rockets, which is directly related to the amount of energy released in the combustion of hydrogen and oxygen, the most energy intensive reaction used for rocket propulsion. For a rocket to achieve a higher specific impulse, processes other than combustion must be used. Electric propulsion, nuclear thermal rockets, solar thermal rockets, and nuclear pulsed propulsion are all examples of advanced propulsion concepts which can achieve a higher specific impulse than chemical combustion rockets [4–7]. Among these concepts electric propulsion has matured to the point of flight status. Electric propulsion systems are routinely used on satellites to perform various functions on orbit, including attitude control, station-keeping, and orbit-raising [4]. To understand why a high value of specific impulse is beneficial for a rocket it is necessary to review the equation that describes rocket-propelled spacecraft motion. Assuming a constant thrust level, and a short total thrusting time so that gravity can be neglected during the maneuver, the rocket equation relates the total velocity change, ΔV , needed to attain the desired orbit, to the initial mass of the rocket, M_0 , the total propellant mass expended by the rocket, M_f , and to the rocket's specific impulse, I_{sp} , as shown below [8]

$$\frac{M_f}{M_0} = 1 - \exp\left(-\frac{\Delta V}{g_0 I_{sp}}\right), \quad (1.1)$$

The total, initial mass of the rocket is the sum of several terms, the propellant mass, M_f , the structural mass of the rocket, M_s , which includes the mass of the engines, the propellant tanks and payload support structure, and the mass of the payload, M_p . The payload mass fraction, M_p/M_0 , can be increased by reducing the other mass fractions. In general for many spacecraft, the largest mass fraction is the propellant mass fraction, M_f/M_0 , which is controlled by the choice of propulsion

system. As seen from Eqn. 1.1, for a given mission, characterized by certain value of ΔV , M_f/M_0 decreases exponentially as the specific impulse of the propulsion system increases. Using an advanced propulsion system with a higher specific impulse than chemical rockets, such as electric propulsion, reduces the propellant mass fraction significantly, but incurs the penalty of the added mass associated with the power supply for the propulsion system.

Electric propulsion engines, or thrusters, utilize electromagnetic forces to heat or accelerate a gas directly. These systems present one avenue for overcoming the specific impulse limitation inherent with the combustion of conventional rocket fuels. A review of some electric propulsion systems that are routinely used for spacecraft operations is given in Appendix A, and as part of this review the development status of several promising space electric power systems is also explored. To illustrate one potential mission for an electric propulsion system an orbit-raising mission is considered in Appendix B, where the equations of motion for a satellite orbiting the earth are solved to describe an orbit transfer from LEO to GEO using electric propulsion. It is shown that a specific impulse of about 1500 sec is required to accomplish this mission for a 25000 kg satellite, in about 215 days with a useful payload mass fraction of 55 %.

A microwave electrothermal thruster (MET) is one example of an electric propulsion device, in which a microwave-sustained plasma heats a propellant gas that subsequently expands through a nozzle to produce thrust. The key features of single-stage MET are shown in Fig. 1.1, which was taken from Diamant *et al.* [9]. The MET is designed to function as a cylindrical waveguide cavity. The cavity is separated into two parts by a boron nitride plate, which isolates the top part of the cavity, into which propellant gas is injected, from the rest of the thruster. A microwave-sustained plasma is supported within the top part of the cavity, as shown in Fig. 1.1. Microwave energy is coupled into the cavity using a microwave magnetron, the antenna of which enters the bottom part of the cavity. Propellant is injected into the MET, tangentially, through ports on the sides of the cavity as indicated in the Fig. 1.1. In theory virtually any kind of propellant gas can be used with the MET, and in fact many different propellants have been used, as described shortly when the history of this device is reviewed. The microwave-sustained plasma heats the surrounding gas in the cavity and the hot gas is ejected through a nozzle, as shown in Fig. 1.1, to produce thrust.

The fact that a microwave-sustained plasma can be created without electrodes, which are present in all other electric propulsion devices, may allow microwave thrusters to attain a longer lifetime and perform a unique mission, running with water vapor as the propellant. Oxygen atoms produced in the high temperature conditions of a water vapor discharge would destroy the electrodes in an electric propulsion device, by the process of oxidation. The development of microwave thrusters is now reviewed.

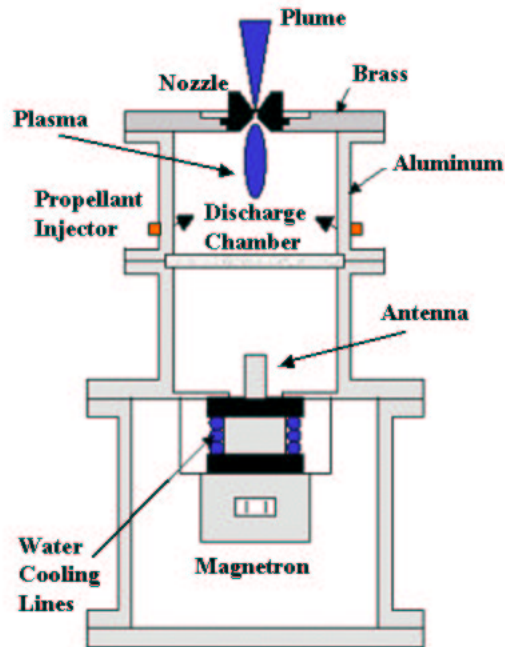


Figure 1.1: Diagram of a microwave electrothermal thruster (MET) as taken from Diamant *et al.* [9].

1.1 Previous Experimental Work with the Single-Stage MET

Microwave electrothermal thrusters have been the focus of research for more than twenty years [10], but unlike many other electric propulsion devices this technology has not been tested in space. Different configurations have been explored for coupling microwave power to a gas, and the cylindrical resonant cavity design, with a standing-wave electric field pattern inside the cavity, was found to be the most promising for thruster applications [10].

The first resonant cavity microwave thruster was built in the early 1980's and it consisted of a cylindrical microwave resonant cavity at 2.45 GHz and a quartz tube, arranged concentrically [11]. Helium or nitrogen gas flowed through the quartz tube, where the walls stabilized the microwave plasma on the centerline. The gas exited the thruster through a nozzle connected to the tube. A radial coupling probe introduced microwave power into the cavity. The probe was connected to a microwave waveguide, with a bi-directional coupler, enabling forward and reflected

microwave power to be measured. It was shown that the ratio of power absorbed by the plasma to the incident power delivered to the cavity, the microwave coupling efficiency, could be made to exceed 95% with proper tuning of the cavity, for discharges sustained at pressures from 40 to 1000 Torr [11]. Cavity tuning was accomplished by two independent means, changing the insertion length of the radial probe into the cavity and adjusting the resonant length of the cavity using a sliding short. Excessive heating and erosion of the quartz nozzle limited the input power to less than 2 kW for mass flow rates in the range of 100 mg/sec [11].

In a separate work, spectroscopic measurements were made of free-floating helium plasmas inside a similar cavity [12]. A hemispherical quartz containment vessel was used to confine the plasma. Unlike the previous experiments, which involved long, slender, quartz tubes, the hemispherical quartz vessel used here was large enough, so that the plasma could float freely inside it. A ceramic bluff body was placed inside quartz vessel, which created a wake, to confine and stabilize the plasma. Results from experiments with this configuration indicate that the electron temperature of helium discharges is roughly constant at 12,000 K over a range of absorbed power levels from 0.5 to 1.0 kW and a range of pressures from 1.0 to 3.0 atm [12]. One explanation for the fact that the electron temperature remains relatively constant over such a range of pressure in the MET is that most of the microwave energy absorbed by the electrons is transferred to the heavy particles due to elastic collisions. This explanation is confirmed by numerical calculations performed in this thesis, as discussed later. A prototype thruster was built by Micci [13] using a similar configuration, a cylindrical resonant cavity at 2.45 GHz, in which the hemispherical quartz vessel and bluff body were removed. This thruster, with the plasma floating freely inside, has operated successfully at power levels of up to 2.2 kW and pressures as high as 3 atm with helium, nitrogen, ammonia and hydrogen as propellants [13]. In this design, which is illustrated in Fig. 1.1, propellant is injected tangentially into the cavity, and exits the cavity through a graphite nozzle.

To date there have been several efforts to create a water-fueled MET and measure its performance [9, 14]. Initial measurements by Diamant *et al.* [9] with a system that is similar to Micci's design [13] have shown a specific impulse of 400 sec, at 5 kW input power for water [9]. As part of that same work, Diamant *et al.* collected thrust data for the MET running on a variety of other propellants including helium, nitrogen and nitrous oxide. For helium they report a specific impulse of roughly 420 sec at a specific energy of 12 MJ/kg and a total power level of 1500 W.

1.2 Microwave Discharge Models

In addition to these experimental efforts, numerical work has been done to model the physical processes occurring in microwave-sustained discharges, such as those

occurring inside the MET. The energy addition region inside a microwave-sustained discharge is three-dimensional in nature, but its axisymmetry allows it to be modeled as a two-dimensional axisymmetric problem. To capture the essential features of the discharge it is necessary to solve the complete set of Navier-Stokes equations, while simultaneously solving the Maxwell's equations for the microwave field. The coupling between the two sets of equations is controlled by the plasma conductivity, which itself is a function of the electron number density. The physical models that have been developed to simulate microwave discharges are differentiated by how the electron number density is determined, whether by using an equilibrium or non-equilibrium treatment of the ionization process.

A single-temperature, equilibrium model was used, by Venkateswaran and Merkle [15], to predict the size, shape, location and peak electron temperature of free-floating helium discharges, stabilized by a bluff body, discussed above. The numerical implementation of this model consisted, in part, of an implicit numerical algorithm for solving the time-dependent Navier-Stokes equations, employing a preconditioning method for convergence acceleration. In addition the Maxwell equations were numerically integrated in time using an explicit algorithm, and at any given point the values of the electric field were time-averaged over one frequency cycle to determine the electron joule-heating rate. Thermodynamic equilibrium was assumed, in the sense that both electrons and heavy species have the same temperature and that the electron number density is determined from the Saha relation. The calculated electron temperature profile (equal to the gas temperature profile), for helium discharges, is consistent with the electron temperature measurements discussed above. Subsequently, this microwave discharge model was extended to include the converging flow geometry of the prototype thruster, with the free-floating plasma inside. A parametric study of the effect of nozzle throat area, discharge pressure, and absorbed power, on the location of the plasma was performed, with the thruster operating on helium [16]. For simulations, at a microwave frequency of 0.915 GHz, a helium mass flow rate of 1.9 g/sec (1 atm plenum pressure) and an incident power of 40 kW, a toroidal plasma was observed off the cavity centerline. As the cavity length was changed, detuning the cavity from resonance and reducing the power absorbed by the plasma, it was shown that the plasma would move back on the centerline.

As part of the early work associated with this thesis, a similar single-temperature, equilibrium model was used to show that a stable plasma could be created in a supersonic argon flow, using microwaves at 2.45 GHz [17]. That model was implemented using an explicit time-marching algorithm to solve the Navier-Stokes equations. Instead of solving the complete set of Maxwell's equations, the Helmholtz wave equation for both the complex axial and radial electric fields was solved. The finite-element method was used to solve these time-independent equations, and the joule-heating rate was determined directly from the values of the complex

field components. In that early work the argon plasma is toroidal, with most of the energy addition occurring in the boundary layer of the expanding supersonic flow. That numerical model was subsequently expanded to include the effects of distinct electron and heavy species temperatures, and finite-rate ionization, similar to the models used to simulate arcjets [18, 19], as mentioned in Appendix A.

Unlike the arcjet which is a similar electric propulsion system where an electric arc performs the same role as the microwave-sustained plasma and for which several relatively complete theoretical models exist, for the MET there is a need for such a model that provides an adequate understanding of the microwave energy absorption and the gas heating processes occurring inside the thruster.

1.3 Potential Role and Limitations of the Single-Stage MET

As illustrated by the example worked out in Appendix B, a specific impulse of between 1500 and 3000 sec is preferable for the 10 N thrust level, orbit-raising mission. This specific impulse range is within the performance envelope of ion engines and Hall thrusters, as well as hydrogen arcjets as discussed in Appendix A. These systems are tried and proven, for space missions, in addition there are other research concepts, such as the applied field MPD thruster, running on lithium, which could also fulfill this role, given further development and testing. So the question becomes what role, if any, could the microwave thruster play in electric propulsion missions of the future. The realization of a water-fueled microwave thruster would represent a propellant handling capability not possible with the other devices, and may radically change the way propellant is stored on future spacecraft, reducing mass and enhancing safety. In addition, new kinds of missions such as the in space refueling of satellites may become possible with such a system.

There are fundamental limits on the specific impulse due to the maximum temperature that can be sustained by the thruster walls, around 2000 K, for a MET constructed of materials similar to those used on arcjets. For a hydrogen arcjet the maximum specific impulse that has been demonstrated at this wall temperature is about 2200 sec [20]. This value of specific impulse corresponds to an average plenum temperature of about 10000 K, with the wall temperature close to 2000 K. The specific impulse of a generic thermal rocket as a function of average plenum temperature, for several propellants, is shown in Fig. 1.2. The curves in this figure were generated using a chemical equilibrium program [21], assuming certain conditions in the plenum, a specified value of average temperature, a pressure of one atmosphere, and a nozzle with an area expansion ratio of 20. In these calculations it was assumed that the flow expands isentropically, starting from the conditions in the plenum, and that the concentrations of dissociation and ionization prod-

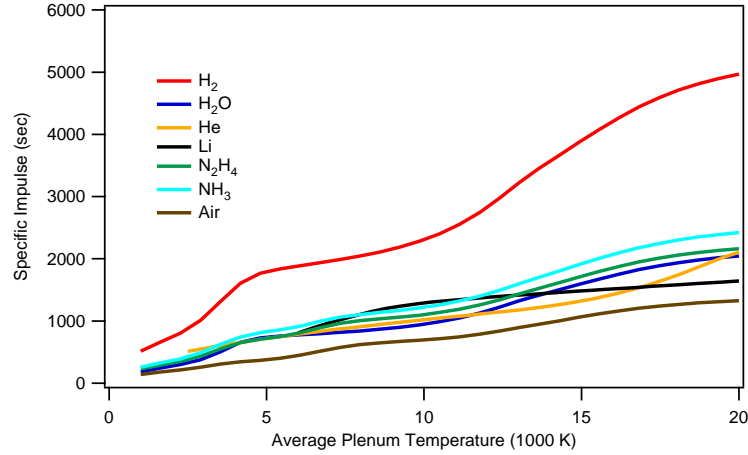


Figure 1.2: Specific impulse as a function of average plenum temperature for different propellants, assuming an isentropic expansion.

ucts are in chemical equilibrium at every point. When the average temperature in the plenum is 10000 K the specific impulse which can be achieved using water is about 1000 sec, as shown in Fig. 1.2. This value is indicative of the maximum specific impulse which could be achieved with a single-stage MET running on water, and is about 600 sec greater than what has been demonstrated experimentally. Not only are temperature limitations an issue, but in addition at high input powers and plenum pressures plasma instabilities may also constrain the specific impulse attainable with a MET. Plasma instabilities have been observed for METs running on conventional propellants such as helium and nitrogen [22].

1.4 Two-Stage MET

One possible way to circumvent the limitations of the single-stage MET and to realize higher specific impulse in the useful specific impulse range near 1500 sec is to add additional energy to the propellant in the supersonic, expanding section of MET, thus creating a two-stage thruster.

Supersonic energy addition has been the focus of research for many years as part of the radiatively driven hypersonic windtunnel project [23], and experiments have been completed successfully, involving the addition of more than one hundred kilowatts of power to a supersonic flow in a windtunnel using electron beams [24]. This project motivated the further exploration of this concept as a means to improve the specific impulse of microwave thrusters.

One thermodynamic path, among several, for the supersonic energy addition process is an isothermal expansion, where the plenum temperature is maintained

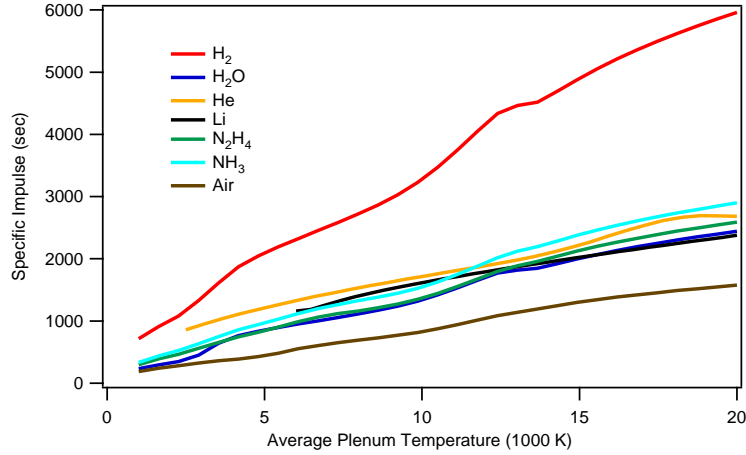


Figure 1.3: Specific impulse as a function of average plenum temperature for different propellants, assuming an isothermal expansion to the same exit pressure as in the isentropic case.

by external energy addition as the flow expands. During an isothermal expansion the external energy transferred to the flow, $T\Delta S$, is converted directly into flow velocity by the expansion process. Fig. 1.3 shows the specific impulse achieved using different propellants starting, as before, from the given conditions in the plenum, and expanding isothermally to the same exit pressure as in the isentropic case, shown in Fig. 1.2. For water at an average plenum temperature of 10000 K, a specific impulse of 1320 sec is achieved with the isothermal expansion, 32 % higher than for the isentropic case, with no external energy addition, as shown in Fig. 1.2. Similarly the specific impulse for each of the other propellants also increases with supersonic energy addition, as shown in Fig. 1.3.

The supersonic "afterburner", described above, can be created on a microwave thruster by using a second microwave cavity, which surrounds a dielectric, expanding nozzle, as shown in Fig. 1.4. The second stage is connected directly to the MET, and another microwave-sustained plasma is created inside this stage, in the supersonic region of flow. The two-stage MET concept illustrated in Fig. 1.4 is explored in this thesis.

1.5 Dissertation Objectives

Supersonic energy addition, incorporating the two-stage configuration discussed above, is a promising avenue towards the eventual realization of a water-fueled microwave thruster with a specific impulse useful for the LEO to GEO orbit-raising mission, among other possible missions. The purpose of this thesis is to answer

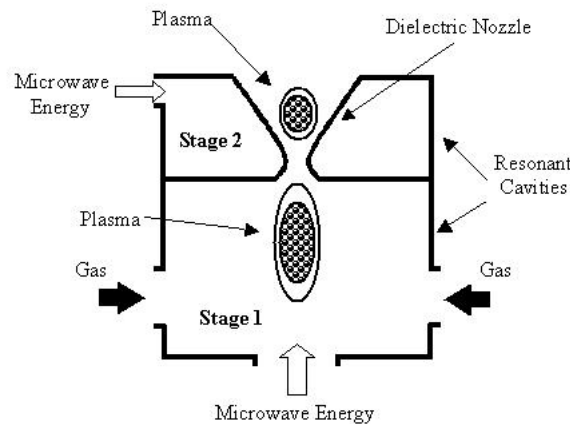


Figure 1.4: Diagram of a Two-Stage MET.

a set of fundamental questions relating to the two-stage thruster and the energy addition process in microwave thrusters in general. These questions are outlined now.

Before any question concerning the flow properties inside the two-stage can be explored, the first issue to address is whether the two-stage MET configuration is feasible, that is whether supersonic energy can in fact be deposited in the flow in the second stage of the thruster. Once it has been established that supersonic energy addition is occurring inside the second stage of the two-stage thruster the immediate question that follows is whether this energy is deposited in the core of the supersonic flow or in the boundary layer. Ultimately the purpose of a supersonic stage is to increase the specific impulse of the MET, and one of the most important issues to resolve experimentally is whether the flow velocity at the exit of the thruster increases, or changes at all, with supersonic energy addition.

Having addressed the basic concerns above related to the functionality of the two-stage MET, one can begin to contemplate what the properties of the plasma, the electron number density and electron temperature, are in the supersonic stage. For that matter there are still some uncertainties as to what the corresponding properties are in the standard MET configuration, and hence what these properties would be in the subsonic stage of the two-stage thruster. For instance, the gas pressure in the standard MET configuration can be as high as several atmospheres and under these conditions one would expect that the electron temperature and the gas temperature are relatively close in magnitude. Whether this is true or not is a question to be addressed in this thesis. As to the spatial extent of the plasma in the standard MET, this too remains to be fully quantified. Part of this particular question is directly related to which processes are important in the production and

destruction of electrons in the standard MET. Finally the question arises as to the concentrations of the metastable species in the standard MET. The concentrations of these species determine the spatial profile of plasma luminosity inside the MET. Whether the light emission observed experimentally with the MET under certain situations can be explained theoretically in terms of these concentrations remains to be determined.

In order to address the important physical questions just outlined a series of research projects have been accomplished and these projects form the basis of this dissertation. To address whether in fact supersonic energy addition can be accomplished with the two-stage thruster, and to quantify what the effect of such energy addition would be on the flow, the following activities were undertaken:

- The construction of a two-stage microwave thruster, with a novel supersonic energy addition stage, meant to operate using argon as the propellant gas.
- The installation of a new vacuum facility, and the construction of all necessary hardware for testing the two-stage thruster.
- The design and implementation of an LIF spectroscopy experiment to measure simultaneously the temperature and velocity in the exhaust plume of the two-stage thruster.
- The refurbishment and realignment of a solid-state ring cavity laser system which was used as the light source for the LIF spectroscopy measurements.
- The installation of a computer interface for controlling the laser and collecting the LIF data, and the creation of a computer code for analyzing the LIF data to find the flow velocity and temperature.
- *Measurement of the flow velocity and temperature in the plume of the two-stage thruster, both with and without supersonic energy addition, and comparison with the predictions of the model for the supersonic stage.*

The final bullet in this list represents the ultimate goal of this thesis, quantifying the effect of supersonic energy addition on the flow properties in the MET.

In addition to answering the basic questions regarding the two-stage MET and the effect of supersonic energy addition on the flow properties in the thruster, many other additional questions regarding the plasma properties inside the two-stage thruster and the standard MET in general, as outlined previously, were addressed in this thesis. In order to do so a comprehensive numerical model of the MET was developed, that incorporates all the important and diverse physical elements of the problem. This model was used to study the single stage MET and was applied separately to the supersonic stage of the two-stage MET. A list of the important activities done as part of this thesis to develop this model follows below:

- The formulation of a plasma model for noble gases, involving several electronically excited species, and ionized species, and the finite rate kinetics which govern the creation and destruction of these species. This model includes species and rates processes relevant for helium and argon.
- The formulation of a transport model for the different species in the model, including both heavy particles and electrons.
- The creation of a two-temperature, gas dynamics model, which incorporates the numerical solution of the Navier-Stokes equations, to find the fluid properties inside the thruster.
- The creation of a microwave field model, which utilizes the finite-element method to find both axial and radial electric field components inside a microwave cavity.

Having discussed all the questions that are addressed in this dissertation and the activities that contributed to the resolution of these questions, an outline of this dissertation is now given.

1.6 Dissertation Outline

The rest of this dissertation consists of six chapters that present and explain the results from experimental testing of two-stage MET, and from numerical simulations of the both stages of the two-stage MET, each done separately, and also of the standard MET. In Chapter 2, a detailed description of the two-stage microwave thruster is given, explaining how both stages of the thruster work and how the supersonic stage was designed. In Chapter 3, the elements of the physical model, which can be used to study both the two-stage thruster and the standard microwave thruster, are presented and the numerical techniques used to implement these elements are discussed. In Chapter 4, the model is applied to study two standard microwave thrusters and a comparison is made with existing thrust data in each case. In Chapter 5, the LIF experiment to measure temperature and velocity in the plume of the two-stage thruster is described. In Chapter 6, the results of LIF experiments and the predictions of the physical model for the supersonic stage of the two-stage thruster are compared, to form a complete picture of how supersonic energy addition effects the microwave thruster. Finally, Chapter 7 summarizes the important conclusions of this dissertation.

Chapter 2

Two-Stage Microwave Thruster Design

There are two essential elements common to all microwave thrusters, a cylindrical cavity, where the plasma is sustained, and a nozzle which converts the high temperature gas into thrust. The two-stage thruster studied in this thesis has both of these basic elements, but unlike a standard microwave thruster, the two-stage thruster has an additional cavity that surrounds the expanding section of the nozzle. This allows for another plasma to be sustained in the supersonic part of the thruster. The nozzle in the two-stage thruster is dielectric, so that microwave energy can propagate through the physical boundaries of the nozzle to heat the gas. The two-stage thruster therefore can be divided into two parts, a subsonic stage consisting of the standard microwave thruster, and a supersonic stage consisting of the second cavity, surrounding the dielectric nozzle.

In this chapter the characteristics of this two-stage thruster and the details of how it was designed are discussed. First the classical solution for the microwave field in a cylindrical waveguide is presented. The equations that describe the different kind of modes that can exist in a waveguide cavity as a function of its radius and length are given, and the fundamental mode structure in both stages of the two-stage thruster is discussed, neglecting the presence of the plasma. Next a detailed description of the subsonic stage of the two-stage thruster is presented, showing how the propellant gas is injected into the thruster and how microwave energy is coupled into the subsonic stage. This is followed by a similar description of the supersonic stage. The method of coupling microwave energy into the supersonic stage is different than that used for the subsonic stage. The means through which this coupling is accomplished, and the elements required to do so are outlined.

2.1 Modes in a Cylindrical Cavity

Ignoring for a moment the presence of the plasma, and neglecting the effects of the coupling probe, dielectric plate and nozzle, both stages of the two-stage microwave thruster are nothing more than cylindrical, resonant, microwave cavities. The field patterns, or modes, which exists in an empty cylindrical waveguide are well known. The components of the electromagnetic field are described by Maxwell's equations. There exist two types of modes, TM-type modes and TE-type modes, which are differentiated by whether there is either an axial component of the electric field or the magnetic field, respectively. In waveguide propagation problems it is convenient to represent the electric and magnetic field components in terms of their corresponding complex quantities. For example, the radial component of electric field, E_r , is related to its complex value, \mathbf{E}_r , according to $E_r = \frac{1}{2}(\mathbf{E}_r e^{-i\omega t} + \mathbf{E}_r^* e^{i\omega t})$. For TM-type modes, the kind of interest in this thesis, the field components in complex form are described in terms of the complex magnetic vector potential, ϕ , by the following set of equations [22]

$$\begin{aligned}
 \mathbf{E}_r &= -i \frac{1}{\omega \mu \epsilon} \frac{\partial^2 \phi}{\partial r \partial z}, \\
 \mathbf{E}_\theta &= -i \frac{1}{\omega \mu \epsilon r} \frac{\partial^2 \phi}{\partial \theta \partial z}, \\
 \mathbf{E}_z &= -i \frac{1}{\omega \mu \epsilon} \left[\frac{\partial^2}{\partial z^2} + \epsilon \mu \omega^2 \right] \phi, \\
 \mathbf{H}_r &= \frac{1}{\mu r} \frac{\partial \phi}{\partial \theta}, \\
 \mathbf{H}_\theta &= \frac{-1}{\mu} \frac{\partial \phi}{\partial r}, \\
 \mathbf{H}_z &= 0.
 \end{aligned} \tag{2.1}$$

A similar set of equations exists for TE-type modes as well, where the field components are related to the complex electric vector potential. The equation which describes the spatial variation of ϕ is the Helmholtz wave equation [22],

$$\frac{1}{r} \frac{\partial}{\partial r} r \frac{\partial \phi}{\partial r} + \frac{1}{r^2} \frac{\partial^2 \phi}{\partial \theta^2} + \frac{\partial^2 \phi}{\partial z^2} + \epsilon \mu \omega^2 \phi = 0. \tag{2.2}$$

In all the equations above ϵ and μ are the permittivity and permeability of the medium inside the waveguide, respectively and ω is the angular frequency of the microwave field. The solution to the Helmholtz wave equation for ϕ is

$$\phi = J_m \left(\frac{x_{mn} r}{a} \right) \cos(m\theta) \left[A e^{\frac{-i2\pi z}{\lambda_g}} + B e^{\frac{i2\pi z}{\lambda_g}} \right]. \tag{2.3}$$

J_m is the Bessel function of order m , x_{mn} is the n th root of J_m , a is the radius of the waveguide, and A and B are complex constants which determine the amplitudes of the forward and backward propagating wave solutions respectively. The guide wavelength is defined as,

$$\lambda_g = \frac{2\pi}{\sqrt{\epsilon\mu\omega^2 - \left(\frac{x_{mn}}{a}\right)^2}}. \quad (2.4)$$

For a TE-type mode the same expression can be used to find the guide wavelength, in which case x_{mn} represents the n th root of the first derivative of J_m . In either case the length of a cylindrical resonant cavity, L , which supports this mode, is equal to the number of integer guide half-wavelengths, p , which fit inside the cavity,

$$L = p \frac{\lambda_g}{2}. \quad (2.5)$$

Thus the mode type, either TM or TE, and the three indices, m , n and p , completely describe the microwave field pattern inside the cavity.

For the two-stage microwave thruster, both the subsonic and supersonic stages were designed to support TM_{011} type modes, at a microwave frequency of 2.45 GHz. In this kind of configuration there are two components of electric field, in the axial and radial directions, and there is a single component of magnetic field in the azimuthal direction. The field components inside an empty cavity for a TM_{011} type mode can be determined by setting A and B equal to $1/2$ in Eqn. 2.3, representing the physical situation where a standing wave pattern exists involving both forward and backward propagating waves. Eqn. 2.3 is then substituted into Eqn. 2.1. It is convenient to normalize all three equations by the coefficient $-ix_{01}^2/\epsilon\mu\omega a^2$, which appears in the equation for \mathbf{E}_z . The equations for the normalized field components then become,

$$\begin{aligned} \mathbf{E}_z &= J_0\left(\frac{x_{01}r}{a}\right) \cos\left(\frac{2\pi z}{\lambda_g}\right), \\ \mathbf{E}_r &= \frac{2\pi a}{\lambda_g x_{01}} J_1\left(\frac{x_{01}r}{a}\right) \sin\left(\frac{2\pi z}{\lambda_g}\right), \\ \mathbf{H}_\theta &= \frac{-ia\epsilon\omega}{x_{01}} J_1\left(\frac{x_{01}r}{a}\right) \cos\left(\frac{2\pi z}{\lambda_g}\right). \end{aligned} \quad (2.6)$$

At 2.45 GHz the resonant cavity length is $L = \lambda_g/2 = 15.9$ cm, for an air-filled cavity. The time-averaged value of the normalized axial electric field, $\mathbf{E}_z \mathbf{E}_z^*/2$, for such a cavity is shown in Fig. 2.1. A cavity radius of 5.08 cm was chosen for this example, closely following the actual proportions of the standard microwave thruster [13]. The maximum value of unity for the normalized axial field occurs on the centerline in two locations, at $x=0$ and $x=15.87$ cm, corresponding to the end

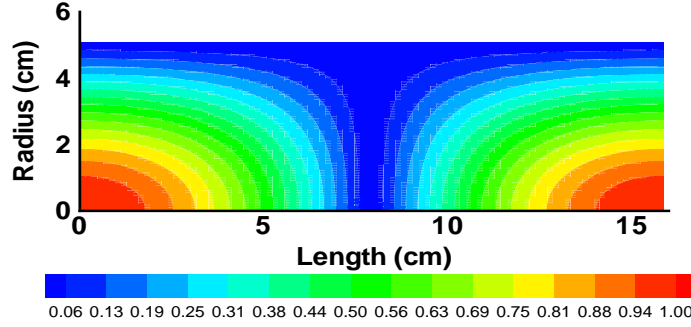


Figure 2.1: Time-averaged, normalized, axial electric field in non-dimensional units.

walls of the cavity. It is evident that at the mid plane of the cavity the axial field drops off to zero, and the time-averaged field pattern is symmetric about the mid plane. The corresponding contour plot of the time-averaged, normalized radial electric field is shown in Fig. 2.2. The radial field is zero along the centerline of the cavity. Its maximum value of 0.24 occurs in the mid plane about 3.91 cm above the centerline. The radial field maximum is smaller than the axial field maximum, and unlike the axial field the radial field drops off to zero at the ends of the cavity. The standard microwave thruster was designed to incorporate this feature, because it was assumed that this electric field pattern would confine the plasma close to the centerline, near one of the ends of the cavity where the nozzle was located. At the other end, where the second axial field maximum is located, a coupling probe is placed. It was hoped that this field pattern would give rise to strong microwave coupling into the cavity as well. The time-averaged, normalized, azimuthal magnetic field component is weaker than both the axial and radial electric fields, as shown in Fig. 2.3. Like the axial electric field, the azimuthal magnetic field has its maximum value at the ends of the cavity and drops off to zero in the middle. The maximum of 0.0017 occurs above the centerline at $y=3.91$ cm, the same distance as for the radial electric field.

The subsonic stage of the two-stage thruster is similar to the standard microwave thruster, and shares a similar microwave field configuration. Under cer-

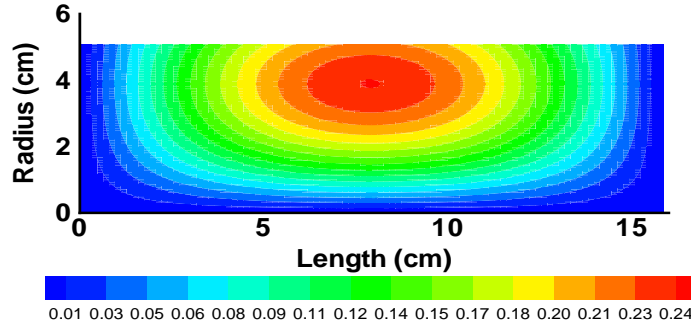


Figure 2.2: Time-averaged, normalized, radial electric field in non-dimensional units.

tain circumstances the field components in the thruster are distorted, relative to the idealized field solution just presented, due to the presence of the plasma. The results of a finite-element simulation of the microwave field including plasma effects are presented in Chapter 4, as part of a complete simulation of two different single-stage METs running on helium. The subsonic stage supports only the TM_{011} mode and the supersonic stage supports the TM_{011} , as well as several other modes. The details of the subsonic stage are now discussed.

2.2 Subsonic Stage

The design of the subsonic stage of the two-stage thruster is essentially a replica of a standard microwave thruster, which operates at 2.45 GHz, first developed by Micci [12]. The standard microwave thruster is a TM_{011} cavity, which is divided into two cylindrical sections of similar length, separated by a boron nitride plate, as shown in Fig. 2.4. The top section forms a plenum where the propellant gas is injected and the plasma forms. The bottom section is pressurized, and the coupling probe is located in this section. In a standard microwave thruster the flow is injected tangentially to create a flow swirl, which is thought to help with plasma confinement and stability. There are three injection ports on the standard thruster, located about 1 cm above the boron nitride pressure plate and separated by 120 de-

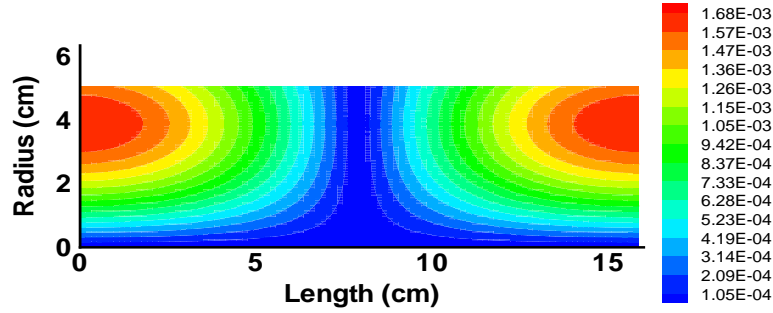


Figure 2.3: Time-averaged, normalized, azimuthal magnetic field in non-dimensional units.

grees. One of these injection ports is illustrated in Fig. 2.4, just above the boron nitride plate. The ports are roughly 1 mm in diameter and are directed upwards toward the nozzle at an angle of 15 degrees relative to the pressure plate. Unlike previous microwave thruster prototypes, where the plasma was confined in a quartz tube placed inside the cavity, Micci's design, with its tangential propellant injection, was motivated by the desire to have the plasma confined to the centerline without the need for a dielectric containment vessel. The plasma is free-floating in the cavity.

The inside diameter of the cavity of the standard microwave thruster is 10.16 cm, the length of the top section is 7.6 cm and the overall cavity length is 16.6 cm, as indicated in Fig. 2.4. The ideal length for a TM_{011} cavity is 15.87 cm, and it was found empirically that lengthening the cavity by 0.87 cm improved the coupling between the microwave probe and the plasma [22]. This length was retained for the subsonic stage of the two-stage thruster, built for this thesis, which is shown in Fig. 2.4. The microwave field pattern inside the standard thruster and the subsonic stage used here are similar. Without a plasma, the field components in the subsonic stage are those given by Eqn. 2.6. The field pattern is distorted by varying degrees depending on whether the thruster is running on helium or argon.

In the standard microwave thruster the hot gas is ejected from the cavity through a converging-diverging conical nozzle, made from stainless steel, with a throat di-

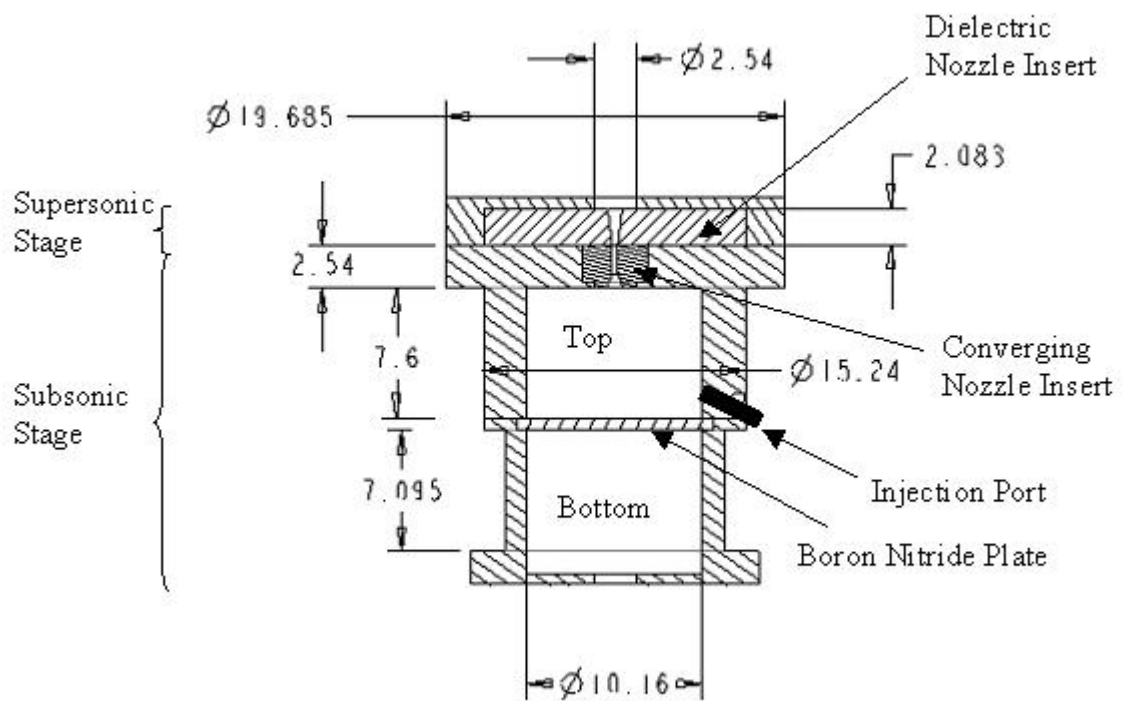


Figure 2.4: Cross-sectional view of the two-stage MET developed for this thesis. All dimensions are in centimeters.

ameter of 0.75 mm, a converging half-angle of 30 degrees, and a diverging half-angle of 20 degrees. The standard thruster is meant to work with the exhaust gas exiting the nozzle into vacuum, although if the plenum is pressurized to a few atmospheres then the flow can be exhausted into the laboratory at atmospheric conditions. Like the standard microwave thruster, the subsonic stage of the two-stage thruster built for this thesis, was made entirely from aluminum, with the exception of the nozzle, made from stainless steel, and the boron nitride pressure plate.

There are some important differences between the standard microwave thruster design discussed above, and the subsonic stage of the two-stage thruster. In contrast to the standard microwave thruster, the subsonic stage of the two-stage thruster does not utilize a conventional coupling probe, but instead the antenna of the microwave magnetron itself is placed in the cavity to cause the coupling directly. Although this feature removes the need to build a microwave circuit for impedance matching between the magnetron and the thruster, involving bulky waveguide components and a coaxial transmission line, with this approach there is no way to measure the power absorbed by the plasma. Another difference is in the nozzle design; the subsonic stage utilizes a stainless steel nozzle with a 30 degree conical converging section which mates directly to a straight throat section about 1.25 cm long. It was decided that the supersonic energy addition experiments would use higher mass flow rates than those explored in the initial experiments with the standard microwave thruster, and thus the throat diameter of the two-stage thruster is 3.18 mm, larger than the one in the standard thruster. The exhaust gas moves from the stainless steel converging nozzle directly into the diverging, dielectric nozzle in the supersonic stage, as shown in Fig. 2.4, and discussed in the next section.

2.3 Supersonic Stage

The supersonic stage consists of three parts, an aluminum cavity, a ceramic nozzle insert, which fits inside the cavity and completely fills it, and a coaxial transmission line, through which microwave energy is transmitted into the stage from a rectangular waveguide. The cavity supports a TM_{011} type mode, as mentioned before. The radius of the supersonic cavity is 7.62 cm; having a larger radius facilitated the physical attachment of the supersonic stage to the rest of the thruster, as well as making the resonant length of the stage smaller. Unlike the subsonic stage, which was sized to be longer than the resonant length, the supersonic stage was made to be precisely the resonant length for a TM_{011} mode. This length is 2.08 cm, which is considerably shorter than the resonant length of the subsonic stage, 15.87 cm. Part of this is due to the radius of the supersonic stage being larger and the other part is due to the dielectric constant of the ceramic insert. The ceramic nozzle insert is made from alumina ceramic, with a dielectric constant of 9.0 [25]. The field

pattern inside the supersonic stage, when there is no plasma present, is qualitatively similar to the one inside the subsonic stage. The actual value of the electric field inside the supersonic stage will depend on the amount of microwave power injected into the stage during the operation of the thruster. The normalized field pattern, in non-dimensional units, can be computed using the equations given earlier in this chapter. The normalized radial electric field reaches a maximum of 2.78, which is larger than the axial field maximum, at the mid plane of the cavity, 5.79 cm away from the centerline. At the same distance above the centerline, the normalized azimuthal magnetic field has a maximum of 0.023, which occurs at the two ends of the cavity. Although the supersonic cavity was designed to support the TM_{011} mode, additional cavity modes can exist in this configuration. The resonant lengths for the different modes were computed using Eqn. 2.4 and Eqn. 2.5, taking the appropriate value for x_{mn} in each case from Ref. [26]. Fig. 2.5 is a plot of the resonant length, for the different TM-type and TE-type modes which can exist in a cavity completely filled with alumina, as a function of cavity radius. The radius of

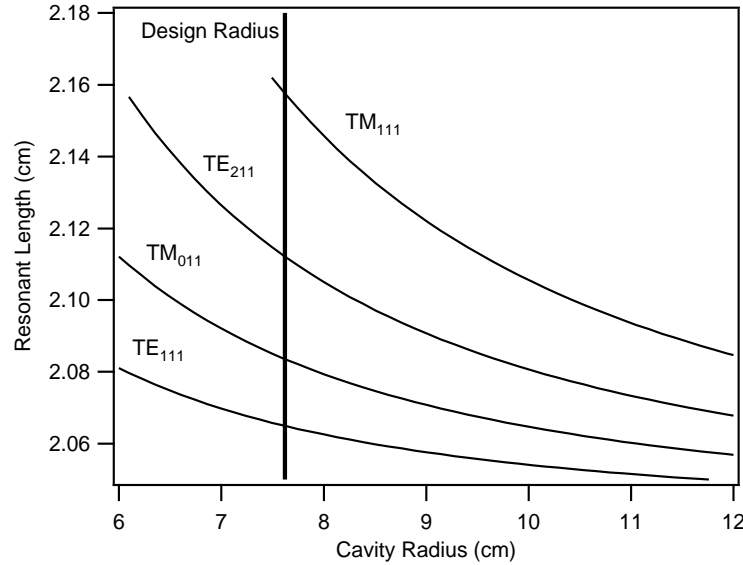


Figure 2.5: Resonant cavity length for different cylindrical waveguide modes as a function of cavity radius.

the supersonic stage is 7.62 cm, as indicated in the figure, and for this value the resonant length of the TM_{011} , TE_{111} , TM_{111} , and TE_{211} modes are all within 1 mm of each other. Since 1 mm represents a small de-tuning of the cavity, and since other elements such as the antenna and the plasma could conceivably cause this kind of de-tuning, it is possible that several or all of these additional modes are present in the supersonic cavity during normal operation of the supersonic stage.

The dielectric nozzle insert, shown in Fig. 2.4, is basically a cylindrical piece, which has a hole in the center in the form of a conical nozzle, with a half angle of 7.5 degrees. It was constructed by casting commercial alumina ceramic into a custom made mold. The throat diameter of the insert is 3.18 mm, matching the corresponding throat diameter of the subsonic section. The outer radius of the insert is 7.62 cm so that it fits inside the cavity completely. A square hole, 2.54 cm in length, was fashioned into the alumina piece, so that there would be space inside the supersonic cavity for the microwave loop antenna. Two o-rings, concentric with the nozzle centerline axis, hold the ceramic piece in place against the two end walls of the cavity.

Microwave energy is transmitted into the supersonic stage using the microwave circuit shown in Fig. 2.6. This circuit is composed of several elements, a magnetron,

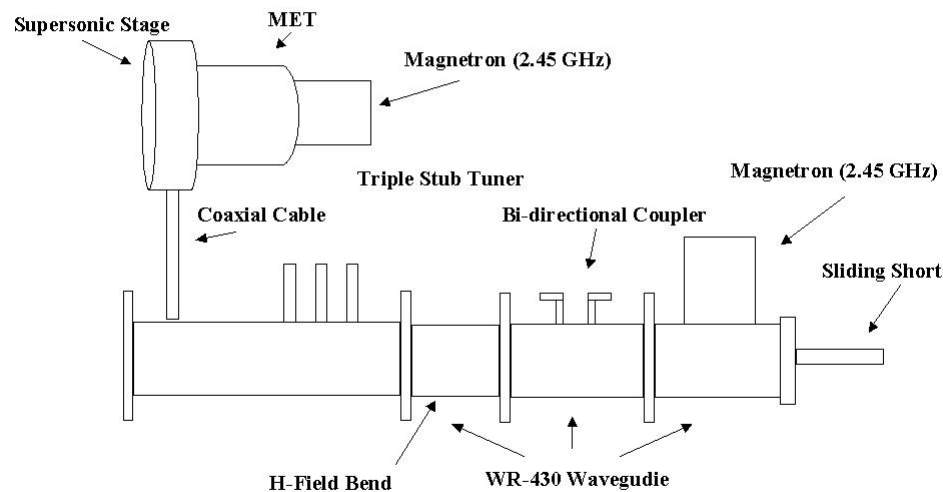


Figure 2.6: Elements of the prototype two-stage microwave thruster.

a bi-directional coupler, a triple-stub tuner and a waveguide-to-coaxial transition. The coaxial transmission line is connected to a loop antenna, which is placed inside the supersonic stage. The elements in this circuit all act so that a prescribed amount of microwave power is delivered to the supersonic stage. These elements are now described, starting first with the magnetron. In addition to the magnetron used for the subsonic stage, the two-stage thruster uses a second magnetron, which

is connected directly to a piece of WR-430 waveguide as shown in the Fig. 2.6. The magnetron for the supersonic stage is a Panasonic model 2M236, rated for 900 W. The magnetron used on the subsonic stage is a Panasonic model, 2M261 tube, rated for 1.2 kW. Both magnetrons are commercial items, intended for use in microwave ovens, and were modified by replacing the aluminum radiators surrounding the magnetron tube with a custom built, copper, cooling block. Chilled water was sent through the cooling block during normal operation of the magnetron. Each magnetron is connected to a separate high voltage power supply. Microwave energy for the supersonic stage propagates along the WR-430 waveguide into a bi-directional coupler, which samples a fraction of the power propagating in the forward and backward directions, such that the sample is attenuated by 60.1 dB for the forward propagating direction and 49.9 dB for the backward propagating one. Two crystal diode detectors, Agilent model 423B, are connected to the bi-directional coupler with 50 Ohm termination, enabling forward and backward power to be measured simultaneously. In a separate experiment, not related to this thesis, the crystal diode was calibrated to find voltage versus microwave power, using a microwave bolometer [27]. The triple stub tuner was also custom made, by inserting three, threaded, brass rods into the waveguide, each separated by a quarter guide wavelength. The purpose of the tuner is to correct for an impedance mismatch between the rectangular waveguide and the rest of the circuit, consisting of the coaxial transmission line, a loop antenna, not shown in the diagram, and the supersonic cavity.

The coaxial transmission line was constructed from a copper center conductor, 0.64 cm in diameter, and an aluminum outer conductor with a diameter of 1.27 cm. The gap between the two conductors is completely filled with teflon. The aluminum outer conductor has the shape of a block, with a 1.27 cm hole drilled through it. Additional holes were drilled into the block, so that chilled water could pass through the block during operation of the supersonic stage. The top part of the block is attached directly to the supersonic stage of the thruster and the bottom part is attached to the rectangular waveguide. The copper center conductor is inserted into the rectangular waveguide at the point of attachment, which is a quarter guide wavelength away from the solid wall termination of the waveguide. On the thruster side, the copper center conductor extends into the supersonic cavity and is connected to a loop antenna, made from 1.6 mm copper wire. The antenna is grounded through a copper pin, force-fit into the wall of the cavity. The characteristic impedance of a coaxial transmission line, Z_0 , with outer conductor radius, b , and inner conductor radius, a , can be calculated using the formula [26],

$$Z_0 = \sqrt{\frac{\mu}{\epsilon}} \frac{\log(b/a)}{2\pi}. \quad (2.7)$$

For the coaxial line used on the two-stage thruster Z_0 is 28.7 Ohms.

The copper loop antenna has a radius of about 4.0 mm. A loop antenna will radiate energy into space; the ratio of the radiated power to the current in the loop is the characteristic load resistance, or impedance, of the antenna. When an antenna is placed inside a waveguide there are additional reactive terms due to the cavity that also contribute to the antenna impedance. These reactive components were not considered in the design of the antenna, and may in fact be small. The formula for the pure resistive component of the antenna impedance, Z_L , is [26],

$$Z_L = 20\pi^2 (\sqrt{\mu\epsilon}\omega a)^4, \quad (2.8)$$

where a is the radius of the antenna and ω is the angular frequency of the radiation. Z_L for the loop antenna in the supersonic stage is 28.5 Ohms. This value assumes that the antenna radiates into a space filled with alumina ceramic, whose dielectric constant is 9.0. The antenna radius was chosen so that its impedance is close to the impedance of the coaxial transmission line, thereby minimizing the reflection of microwave power at the antenna-line interface.

Chapter 3

Physical Model

In order to understand the plasma properties and the heating process which sustains the plasma in a microwave thruster, a physical model was developed and subsequently implemented using standard numerical techniques. This model consists essentially of four parts: a gas dynamics model, a plasma model, a transport model and a microwave field model. All of these components interact with each other to capture the highly non-linear nature of the microwave heating process.

The microwave field model includes both axial and radial components of the complex electric field in the cylindrical geometry of the experimental two-stage microwave thruster, with each component described by the Helmholtz equation. These two equations are solved using a finite-element code.

Transport properties for heavy particles, including thermal conductivity and viscosity, are calculated using the results of kinetic theory for monatomic gases, assuming a Lennard-Jones type interaction for atomic species and a Coulomb type interaction for ionic species. The overall viscosity and thermal conductivity of the mixture, including neutral atoms and ions, is calculated from the respective pure species values using an empirical mixture rule. The electrical conductivity is calculated by solving an integral of the electron energy distribution function using the appropriate experimental cross-section for electron-neutral collisions, and assuming that the electrons have a Maxwellian distribution.

The validity of using a Maxwellian distribution function for the electrons is explored in the plasma model section of this chapter. The plasma model keeps track of the net rate of production of the relevant species in the plasma, electrons, atoms, atomic ions and molecular ions. Different levels of electronic excitation are considered in the plasma model as well, including metastable states and additional radiative states. Reaction rates for ionization and electronic excitation are calculated from the experimental cross-sections for the appropriate process. Two different sets of rate coefficients were used in the plasma model, one for helium plasmas and one for argon plasmas.

The gas dynamics model incorporates the Navier-Stokes equations, with some

additional equations, one for the electron density, one for the density of each of the excited state species, and one for the electron thermal energy. This set of fluid conservation equations is solved using an explicit, time-marching, finite-volume, numerical method.

In this chapter the equations that constitute the gas dynamics model are given first, followed by a discussion of the numerical techniques used to solve them. Following this the models used for helium and argon plasmas are discussed, and the complete set of rate coefficients, which was derived for this work, is given. Next the method used to calculate the transport coefficients is discussed. Then the microwave model is described, and the details of the finite-element code used to implement this model are enumerated. Following this, the fluid solver is validated by comparing numerical results with theoretical solutions to classical fluid problems involving supersonic flow over a cone and compressible boundary layers over a flat plate. Finally, in the last section, the microwave solver is validated by computing the electric field pattern inside a resonant cavity. The most important test of the validity of the complete model is made in subsequent chapters where comparisons are made with experimental data.

3.1 Gas Dynamics Model

The gas dynamics model incorporates the unsteady, axisymmetric, Navier-Stokes equations for a two-temperature gas with reacting species. These equations can be written in cylindrical coordinates in the following differential vector form [28]

$$\frac{\partial r \mathbf{U}}{\partial t} + \frac{\partial r \mathbf{F}_c(\mathbf{U})}{\partial x} - \frac{\partial r \mathbf{F}_d(\mathbf{U})}{\partial x} + \frac{\partial r \mathbf{G}_c(\mathbf{U})}{\partial r} - \frac{\partial r \mathbf{G}_d(\mathbf{U})}{\partial r} = \mathbf{S}, \quad (3.1)$$

where x and r are the axial and radial directions, respectively. $\mathbf{U} = (\rho_i, \rho u, \rho v, E_h, E_e)$ is the vector of conservation variables, where ρ_i represents the mass density of species i , ρ is the total mass density (neglecting the contribution due to the electron mass density, ρ_e), u is the axial velocity, and v the radial velocity. The total heavy particle energy density (thermal plus directed kinetic) is expressed as

$$E_h = \sum_h \rho_i \left(\frac{3}{2} R_i T + 1/2 [u^2 + v^2] + \Delta H_i \right),$$

where ΔH_i and R_i are the enthalpy of formation and the gas constant for species i , and T is the heavy particle temperature. The summation includes all the species except the electrons. The electron energy density is taken to be $E_e = (3/2) \rho_e R_e T_e$, where R_e is the electron gas constant and T_e the electron temperature. The flux vectors, $\mathbf{F}_c(\mathbf{U})$, $\mathbf{F}_d(\mathbf{U})$, $\mathbf{G}_c(\mathbf{U})$ and $\mathbf{G}_d(\mathbf{U})$, are functions of the conservation variables and the superscripts c and d denote the terms due to convection and physical

dissipation respectively. The convective flux vectors are

$$\mathbf{F}_c(\mathbf{U}) = \begin{bmatrix} \rho_i u \\ \rho u^2 + P \\ \rho uv \\ u(E_h + P_h) \\ u(E_e + P_e) \end{bmatrix},$$

$$\mathbf{G}_c(\mathbf{U}) = \begin{bmatrix} \rho_i v \\ \rho uv \\ \rho v^2 + P \\ v(E_h + P_h) \\ v(E_e + P_e) \end{bmatrix},$$

while the diffusive flux vectors are

$$\mathbf{F}_d(\mathbf{U}) = \begin{bmatrix} 0 \\ \tau_{xx} \\ \tau_{xr} \\ -q_{hx} + u\tau_{xx} + v\tau_{xr} \\ 0 \end{bmatrix},$$

$$\mathbf{G}_d(\mathbf{U}) = \begin{bmatrix} 0 \\ \tau_{xr} \\ \tau_{rr} \\ -q_{hr} + u\tau_{xr} + v\tau_{rr} \\ 0 \end{bmatrix},$$

where P is the total gas pressure, τ_{xx} , τ_{xr} , and τ_{rr} are the components of the viscous stress tensor, q_{hx} and q_{hr} are the components of heavy particle heat flux. The heavy particle pressure is expressed as $P_h = \sum_h \rho_i R_i T$ and the electron pressure is $P_e = \rho_e R_e T_e$.

The components of the heat flux and the stress tensor are related to temperature and velocity derivatives by the transport coefficients, μ_h and k_h . The expressions for the components of viscous stress are given below [28]

$$\begin{aligned} \tau_{xx} &= \frac{4}{3}\mu_h \frac{\partial u}{\partial x} - \frac{2}{3}\mu \left(\frac{\partial v}{\partial r} + \frac{v}{r} \right), \\ \tau_{rr} &= \frac{4}{3}\mu_h \frac{\partial v}{\partial r} - \frac{2}{3}\mu \left(\frac{\partial u}{\partial x} + \frac{v}{r} \right), \\ \tau_{xr} &= \mu_h \left(\frac{\partial u}{\partial r} + \frac{\partial v}{\partial x} \right), \end{aligned} \tag{3.2}$$

where μ_h is the heavy particle viscosity. The components of the heat flux are

$$\begin{aligned} q_{hx} &= -k_h \frac{\partial T}{\partial x}, \\ q_{hr} &= -k_h \frac{\partial T}{\partial r}, \end{aligned} \quad (3.3)$$

with k_h equal to the thermal conductivity of the heavy particles. Species mass diffusion and electron thermal conduction are neglected in this thesis for the reasons outlined in the plasma model section.

The right hand side of Eqn. 3.1, S , contains source terms that are due to the cylindrical symmetry of the problem, the finite rate of electronic excitation and ionization reactions, the energy transfer between electrons and heavy particles, and microwave joule heating rate, J . The source term is given below

$$S = \begin{bmatrix} r\Omega_i \\ 0 \\ p + \frac{2}{3} \left(\tau_{xr} - \frac{2\mu_h v}{r} \right) \\ r(Q_{elas} + Q_{in}) \\ r(-Q_{elas} - Q_{in} + J) \end{bmatrix}. \quad (3.4)$$

In the above expression Ω_i is the rate of mass production for species i due to ionization and electronic excitation processes. The microwave joule heating rate is a function of the complex electric field amplitudes, \mathbf{E}_r and \mathbf{E}_z , and the complex conductivity, σ , according to the following formula [26]

$$J = \frac{1}{4} (\sigma + \sigma^*) (\mathbf{E}_r \mathbf{E}_r^* + \mathbf{E}_z \mathbf{E}_z^*). \quad (3.5)$$

The energy transfer from electrons to heavy particles due to elastic collisions is Q_{elas} and the inelastic energy transfer term is Q_{in} . Q_{elas} is determined from the following expression [29],

$$Q_{elas} = 3\rho_e \nu_{eH} k_b (T_e - T) / M_A, \quad (3.6)$$

where M_A is the mass of an atom, ν_{eH} is the total energy-averaged momentum transfer collision frequency of electrons with heavy particles and k_b is the Boltzmann constant. ν_{eH} is comprised of two components, a contribution from electron-atom collisions, ν_{ea} , and a contribution from electron-ion collisions, ν_{ei} . In this thesis the energy-averaged momentum transfer collision frequency of electrons with helium atoms is taken to be

$$\nu_{ea} = 1.453 \times 10^{-15} N_A T_e^{0.381}, \quad (3.7)$$

where N_A is the atom number density. The corresponding collision frequency for argon atoms is

$$\nu_{ea} = 4.783 \times 10^{-20} N_A T_e^{1.427}. \quad (3.8)$$

These expressions were obtained by numerically integrating experimental data for the momentum transfer cross-section [30, 31], following the approach in Ref. [29], and fitting a function of the form, AT_e^N , to the result. A Maxwellian electron energy distribution function was assumed for the integration. The energy-averaged momentum transfer collision frequency for electron-ion collisions, ν_{ei} , is taken from Ref. [29],

$$\nu_{ei} = 3.6410^{-6} N_e \frac{\log 1.24 \times 10^7 \sqrt{T_e^3 / N_e}}{T_e^{3/2}}, \quad (3.9)$$

where it is assumed that the electron density, N_e , is equal to the ion density. It is further assumed that only singly ionized species are present in all the calculations in this thesis. The inelastic energy transfer term is the sum of all net ionization and excitation reaction rates weighted by the individual reaction energies, $\Delta\epsilon_{ij}$, where index ij denotes the two atomic states (or energy levels) involved in the reaction. There are twelve reactions in the helium model and fifteen in the argon model. The chemical source term, Ω_i , for each of the species in the model, is discussed in the plasma model section.

3.1.1 Numerical Formulation

A conservative, finite-volume, cell-centered formulation, incorporating flux-limited scalar dissipation, is used to numerically integrate the governing equations (3.1) in time until a steady state is reached, an approach that has been thoroughly validated by several authors [28, 32, 33]. A structured, two-dimensional grid was used for all the calculations in this thesis, in which the domain was divided into a series of quadrilateral cells. For the finite volume formulation used here, the convective flux at each of the four faces of a cell was computed using information at centers of the two cells adjacent to the face. For example, to find the convective flux on the right hand side of a cell with indices, i and j , which is denoted as $F^{i+1/2,j}$, the following formula is used [34, 35],

$$\begin{aligned} F^{i+1/2,j} &= 1/2 (\mathbf{F}_c^{i+1,j} + \mathbf{F}_c^{i,j}) \Delta r^{i+1/2,j} - 1/2 (\mathbf{G}_c^{i+1,j} + \mathbf{G}_c^{i,j}) \Delta x^{i+1/2,j} \\ &\quad - \alpha_1/2 (\lambda_x^{i+1,j} + \lambda_x^{i,j}) \\ &\quad [\mathbf{U}^{i+1,j} - \mathbf{U}^{i,j} - \alpha_2 \text{MINMOD}(\mathbf{U}^{i+2,j} - \mathbf{U}^{i+1,j}, \mathbf{U}^{i,j} - \mathbf{U}^{i-1,j})] \end{aligned} \quad (3.10)$$

$\lambda_x^{i,j}$ is the spectral radius in the x direction, evaluated at the cell center [32]. The change in x along the right-hand side face is denoted as $\Delta x^{i+1/2,j}$ and the corresponding change in r as $\Delta r^{i+1/2,j}$; changes in direction are calculated in the counterclockwise direction around the cell. The convective fluxes on the other faces of

the cell, $F^{i,j+1/2}$, $F^{i-1/2,j}$, and $F^{i,j-1/2}$, are computed in a similar manner. For the convective fluxes on the top and bottom of the cell, the spectral radius in the r direction, λ_r , is used in place of λ_x . The MINMOD function is a flux limiter, defined in terms of the absolute values of its arguments, x and y , and the MIN function, which returns the minimum value of its two arguments, as follows [36]:

$$\text{MINMOD}(x, y) = \left(\frac{|x|}{x} + \frac{|y|}{y} \right) \text{MIN}(|x|, |y|).$$

α_1 is the coefficient of second-order numerical dissipation in Eqn. 3.10, and α_2 is the coefficient of fourth-order anti-dissipation. It is common practice that these coefficients are selected empirically for a given geometry and grid spacing so that the level of numerical dissipation is sufficient for the computation to converge properly [35, 37]. α_1 can be any value between 0 and 0.5 and α_2 can be between 0 and 1, so that the resulting scheme is second order accurate [34, 35, 37]. It is desirable for α_1 to be as small as possible and α_2 to be as large as possible, especially when calculations are performed involving viscous boundary layers where it is important that the numerical dissipation does not obscure the physical dissipation. The values chosen for α_1 and α_2 in this thesis vary and are discussed later; these values typically range from 0.25 to 0.5 for α_1 and from 0.1 to 0.5 for α_2 . In addition to the convective fluxes, arising from the F_c and G_c terms in Eqn. 3.1, there is also physical dissipation at each cell face to consider as well, due to F_d and G_d . For the right hand face of cell i, j , the flux due to physical dissipation is denoted as $D^{i,j+1/2}$. In evaluating $D^{i,j+1/2}$, F_d and G_d are calculated directly at the cell face, unlike the convective flux, by first calculating the spatial derivatives of u , v , and T at cell face using the auxiliary cell technique discussed in Ref. [32]. The total residual for cell i, j is then

$$\begin{aligned} R^{i,j} = & (F - D)^{i+1/2,j} r^{i+1/2,j} - (F - D)^{i-1/2,j} r^{i-1/2,j} \\ & + (F - D)^{i,j+1/2} r^{i,j+1/2} - (F - D)^{i,j-1/2} r^{i,j-1/2} - S^{i,j} H^{i,j}. \end{aligned} \quad (3.11)$$

In this equation $r^{i+1/2,j}$ denotes the average value of r along the right-hand side face, etc.

An explicit, Eulerian time integration scheme is used to march the solution forward, such that $U_{t+1}^{i,j} = U_t^{i,j} - \text{CFL} \Delta t R_t^{i,j} / H^{i,j}$. The time step size, Δt , is determined for each cell according to the method in Ref. [32]. The cell volume is denoted as $H^{i,j}$. The Courant condition requires that for a stable explicit scheme $\text{CFL} < 1$. For the calculations in this thesis the CFL number was taken to be 0.25 for all equations except the electron energy equation where it was typically 0.005. Having different CFL numbers is essential, because the addition of an electron energy equation adds stiffness to the problem. It was found empirically that for higher values of the CFL number, greater than 0.25 for the heavy particles or greater than 0.005 for the electron energy equation, the solution would not converge properly. For numerical

techniques such as the one used in this thesis, the addition of species mass source terms, involving reaction rates, itself makes the problem stiff and could lead to instabilities under certain circumstances. There are numerical methods which deal with this problem by preconditioning the numerical scheme above, so that in effect each species equation is advanced with its own characteristic time step, thereby preserving the overall stability of the scheme [38]. In practice, for the calculations in this thesis, it was found that the use of preconditioning was not necessary to insure stability. This may be true because of the relatively low mass fractions of the excited species encountered here, which rarely were greater than 10^{-5} . This may be true also because all of the species source terms depend on the electron temperature, and the electron energy equation is advanced at a slower rate than the other equations, which acts in some sense to compensate for the stiffness.

The time step is determined individually for each cell on the grid, since only the final steady state solution is of interest here. The criterion for convergence of the numerical solution to steady state conditions is when the total mass and energy fluxes inside the diverging part of the nozzle do not vary by more than 5 % from one axial cell location to the next. In practice, as shown in Chapter 4, it is found that even after this criterion is met, there are still differences of typically no more than 10 % between the total mass and energy fluxes inside the nozzle and those values corresponding to the specified conditions at the inlet. Furthermore, the residual for each of the equations must decrease by at least four orders of magnitude in order for the computation to be judged properly converged.

3.1.2 Boundary Conditions

Because of the cell-centered scheme used by the Navier-Stokes solver it is necessary to specify the values of the flux vectors, F and D , at the physical boundaries of the domain. Along all the boundaries the numerical dissipation is set equal to zero, so that $\alpha_1 = 0$ and $\alpha_2 = 0$. Along the wall and centerline boundaries the convective fluxes are specified so that there are no mass, momentum or energy fluxes through these respective boundaries. The only contribution to F from a face on either of these two boundaries is from the gas pressure. Consider a cell immediately below the wall boundary, in this case the convective flux is

$$F^{i,j+1/2} = \begin{bmatrix} 0 \\ P^{i,j} \Delta r^{i,j+1/2} \\ -P^{i,j} \Delta x^{i,j+1/2} \\ 0 \\ 0 \end{bmatrix}. \quad (3.12)$$

In addition to the above specifications for the convective fluxes, the no slip conditions, $u = 0$ and $v = 0$, are applied at the wall boundary. Heat transfer to the

wall by the heavy particles is handled by either setting the heat flux terms at the wall equal to zero (adiabatic wall assumption) or by specifying the temperature at the wall. This facilitates the computation of the physical dissipation, $D^{i,j+1/2}$, at these locations. Cylindrical symmetry is enforced along the centerline by setting v and all partial derivatives with respect to r equal to zero. The dissipative fluxes are zero at the gas inlet and exit planes. At the gas inlet the fluid properties are prescribed, so that the required mass flux enters the thruster, in most cases at a temperature of 300 K.

The convective fluxes for the cell immediately adjacent to the exit plane are calculated in one of two ways, depending on whether the flow is entering or leaving the domain. If the flow is exiting the domain then the properties are calculated by extrapolation from the interior of the domain. If the flow is entering the domain, which occurs when a re-circulation zone is established around the expanding thruster plume, then the exit pressure and temperature are specified and the flow velocity is extrapolated from the interior of the domain. It should be pointed out, for a typical calculation in this thesis, that at the exit plane most of the flow leaving the domain is supersonic and all of the flow entering the domain is subsonic, so these boundary conditions are in some sense representative of the correct domain of physical dependence for the flow. There are more rigorous treatments of subsonic and supersonic boundary conditions [37], and, of course, all methods introduce some error at the boundaries. The treatment used in this thesis has proven to be robust and simple to implement for a range of calculations, although it reduces the spatial accuracy to that of a first order scheme at the boundaries.

3.2 Plasma Model

The energy addition process in microwave thrusters is influenced strongly by the properties of the microwave sustained-plasma in the thruster. The conditions of interest in this thesis span the full range of pressure near atmospheric conditions in the plenum of a standard microwave thruster down to a few Torr in the supersonic stage of the prototype thruster, and as such a comprehensive model is needed to describe the concentrations of different ionized and electronically excited species. The plasma model developed in this thesis is applied to study either a purely helium plasma or a purely argon plasma. In either case the relevant species are electrons, neutral atoms, atomic ions and molecular ions. For such plasmas the relevant volumetric electron loss processes are discussed, and it is shown that under typical conditions in the plenum of the MET thruster molecular ions are the dominant ionic species, and dissociative recombination is the dominant electron loss mechanism. The validity of using a Maxwellian electron energy distribution function (EEDF) for determining the rate coefficients of ionization and excitation is then explored. Finally the two sets of parameters which were derived as part of

this thesis for calculating the rate coefficients for excitation and ionization in both helium and argon plasmas are given, and the manner in which these parameters are used to find the rate coefficients is discussed.

3.2.1 Electron Loss Mechanisms

There are several volumetric electron loss mechanisms in plasmas formed from a monatomic gas. Among these loss rates are three-body recombination with an electron as the third body, three-body recombination with an atom as the third body, photo-recombination, ambipolar diffusion and dissociative recombination involving molecular ions. The last of these processes is important only when the concentration of molecular ions is significant.

The concentration of molecular ions in the plenum of the MET can be calculated using thermodynamics. This is true because inside the plenum where the pressure is typically 1 atm or greater and the flow residence time is substantial (on the order of one second or more), there are sufficient collisions for thermodynamic equilibrium to be established between atomic and molecular ions. If the molecular ion number density is denoted as $N_{A_2}^+$ and the atomic ion number density is denoted as N_A^+ then their ratio is found using the formula

$$\frac{N_{A_2}^+}{N_A^+} = N_A \left(\frac{h^2}{\pi M_A k_b T} \right)^{3/2} e^{\Delta H_{A_2}^+ / k_b T}, \quad (3.13)$$

where N_A is the neutral atom number density, M_A is the atomic mass and $\Delta H_{A_2}^+$ is the energy of formation of the molecular ion. For argon molecular ions the energy of formation is 1.25 eV and for helium molecular ions it is 3.0 eV. Using the appropriate value of $\Delta H_{A_2}^+$ and assuming that $N_A = 10^{19} \text{ cm}^{-3}$, which is indicative of atmospheric conditions inside the plenum, the number density ratio of molecular to atomic ions for argon can be calculated using Eqn. 3.13 and the result is shown in Fig. 3.1. Below approximately 700 K it is evident that argon molecular ions are the dominant ionic species. When the MET is running on argon under the conditions studied in this thesis the temperature in the plenum is 700 K or less, as will be discussed in Chapter 6 when the results from the LIF temperature measurements are presented. The corresponding plot for helium is shown in Fig. 3.2. In this case helium molecular ions are the dominant ionic species below about 2000 K. It can be inferred from thrust measurements for both the 1 kW and 100 W helium METs, collected by Diamant [9] and Sullivan [14], that the average plenum temperature does not exceed 1500 K in either case. Therefore for both the argon and helium METs explored in this thesis molecular ions are present and are in fact the dominant ionic species in the plenum of the thruster.

The rates of various electron loss processes are now computed to determine which of these processes are relevant for argon and helium plasmas in the plenum

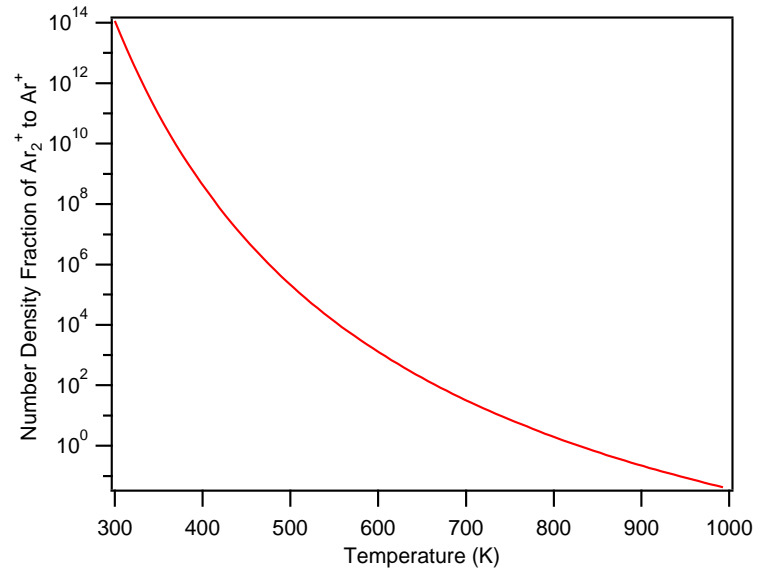


Figure 3.1: Number density ratio of molecular to atomic ions for argon as a function of temperature.

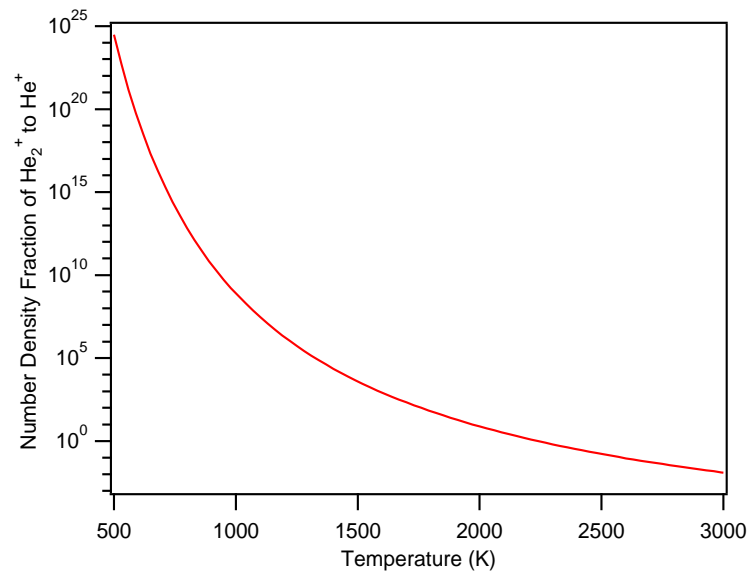


Figure 3.2: Number density ratio of molecular to atomic ions for helium as a function of temperature.

of the MET thruster. The case of an argon plasma is considered first where the gas temperature is roughly 700 K, the electron number density is 10^{12}cm^{-3} and as

before $N_A = 10^{19} \text{ cm}^{-3}$. These conditions were considered representative of those found inside the argon MET in this thesis. A comparison is made of the different electron loss processes in Fig. 3.3. The formula derived by Darwin [39] was used to

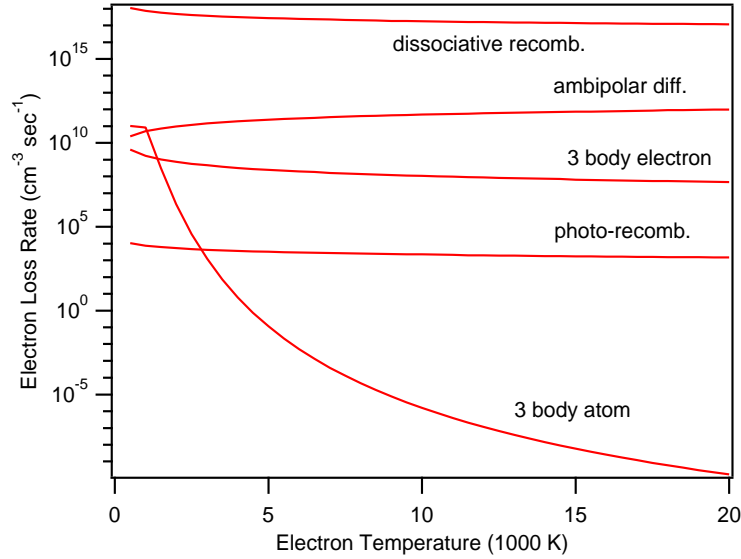


Figure 3.3: A comparison of various electron loss rates as a function of electron temperature for representative conditions in the plenum of an argon MET.

estimate the three-body recombination rate with a neutral atom as the third body. For three-body recombination with an electron as the third body the rate was determined using the parameters in Table 3.3, as discussed later in this section. The photo-recombination rate was determined following the approach in Ref. [40], using the photo-ionization cross section cited in that work. For photo-recombination and three-body recombination the rates were calculated for the situation where the final atomic state is the $4s[3/2]_2$ metastable level. The corresponding rates when the final state is the ground state are less than those shown. It is also worth noting that a Maxwellian electron energy distribution function was assumed here in making these simple estimates of the photo-recombination and three-body recombination rates. The rate of ambipolar diffusion was estimated as

$$N_e \mu^+ \frac{k_b T_e}{e} \left(\frac{2.405}{a} \right)^2,$$

where a is the radius of the plenum chamber (5.08 cm) and μ^+ is the molecular ion mobility as determined experimentally by Biondi [41]. The rate of dissociative recombination involving an electron and a molecular ion was taken to be $9.1 \times 10^{-7} N_e^2 (T/T_e)^{0.61} \text{ cm}^{-3} \text{ sec}^{-1}$, as presented in Ref. [42]. In Fig. 3.3 it is clear that

the dissociative recombination rate is several orders of magnitude greater than the other rates, over the range of electron temperatures expected in the plenum. For this reason and the fact that gas temperatures no greater than 700 K are present in the plenum dissociative recombination alone is considered in the argon plasma model for calculations involving the plenum, and the other electron loss processes are neglected. Dissociative recombination is not considered, however, when modeling the supersonic energy addition stage in Chapter 6, because of the high velocities (hundreds of meters per second) and short resonant times ($100 \mu\text{sec}$ or less) associated with this part of the flow; convection is the dominant electron loss mechanism in this case.

The corresponding electron loss rates for helium in the plenum of the MET are shown in Fig. 3.4, and once again the dissociative recombination rate is at least an order of magnitude greater than the other rates. To represent a helium plasma in

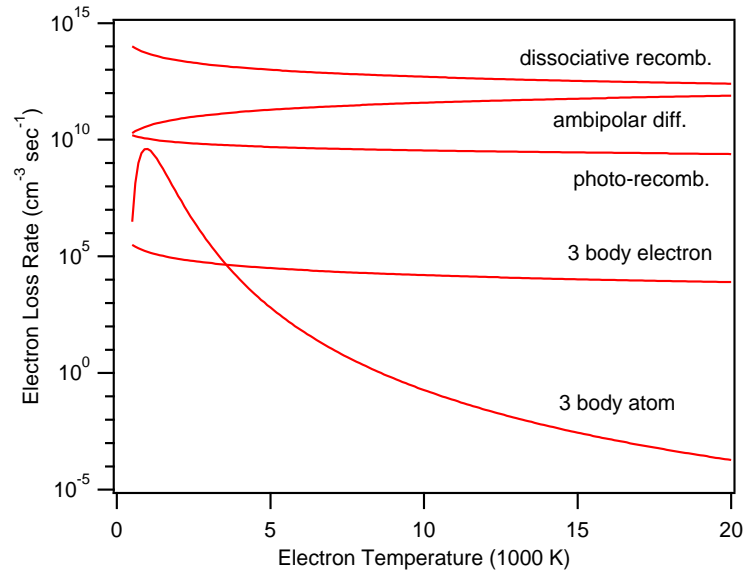


Figure 3.4: A comparison of various electron loss rates as a function of electron temperature for representative conditions in the plenum of a helium MET.

the plenum of the MET the gas temperature was taken to be 1000 K and the electron number density was 10^{11}cm^{-3} . The neutral density was taken to be the same as before. The loss rates were computed using the same procedures as outlined above. The photo-ionization cross section from Ref. [43] was used when determining the photo-recombination rate. For three-body recombination with an atom as the third body the formula of Darwin [39] was used and when an electron was the third body the recombination rate was determined from the parameters in Table 3.3. For the photo-recombination and three-body recombination rates only the

case where the final atomic state is the 2^1S metastable level is shown; in the case where the electron returns to the ground state the corresponding rates are smaller. When computing the ambipolar diffusion rate the appropriate value of μ^+ for helium molecular ions was taken from Biondi [41]. The dissociative recombination rate for helium molecular ions was calculated as $5 \times 10^{-9} N_e^2 T / T_e \text{ cm}^{-3} \text{ sec}^{-1}$, following the approach in Ref. [44]. For the case of both argon and helium the plasma model developed in this thesis incorporates the most significant electron loss process, dissociative recombination between molecular ions and electrons.

3.2.2 Electron EEDF

The electron energy distribution function (EEDF) influences the plasma properties through its role in determining the various rates of excitation and ionization. A critical assumption in this thesis is that the EEDF is Maxwellian, and the validity of this assumption is now explored.

For weakly-ionized molecular gas discharges in general the EEDF is not Maxwellian, but for monatomic gases under certain conditions the EEDF can be Maxwellian [45]. A good indication of whether the EEDF is in fact Maxwellian is whether electron-electron collisions are more dominant than electron-neutral atom collisions. Mitchner and Kruger [29] suggest that one criterion for judging when the electron EEDF is Maxwellian is when the following inequality holds true

$$\frac{m_e \nu_{eA}}{M_A \nu_{ee}} \ll 1, \quad (3.14)$$

where ν_{eA} is the energy-averaged electron-neutral collision frequency as defined previously (Eqn. 3.7 or Eqn. 3.8) and ν_{ee} is the energy-averaged electron-electron collision frequency, which is equal to ν_{ei} defined by Eqn. 3.9 for the case of singly charged ions. The ratio of $m_e \nu_{eA} / M_A \nu_{ee}$ is evaluated in Table 3.1 for several plasma

Table 3.1: $m_e \nu_{eA} / M_A \nu_{ee}$ for Several Relevant Plasma Conditions

Gas	N_A (cm^{-3})	N_e (cm^{-3})	T_e (K)	$m_e \nu_{eA} / M_A \nu_{ee}$
-	-	-	-	-
He	10^{19}	10^{11}	10000	17
He	5×10^{18}	5×10^{11}	17000	4.6
Ar	10^{19}	10^{12}	10000	0.098
Ar	10^{18}	10^{15}	15000	4.6×10^{-5}

conditions of interest in this thesis. For the argon cases in Table 3.1 which represent the conditions calculated for the subsonic and supersonic stages of the two-stage thruster respectively, as presented in Chapter 6, this ratio is less than unity and as

such the assumption of a Maxwellian EEDF is valid for these cases. For both of the helium cases explored, which are indicative of the calculated conditions for the 1 kW and the 100 W helium METs in Chapter 4 this ratio is larger than unity and this suggests that the true electron EEDF is not Maxwellian in these situations.

In order to see how the true EEDF compares with a Maxwellian distribution for helium a commercial software program written by Kinema Research & Software LLC was used, which numerically solves the electron Boltzmann equation for the EEDF. The Boltzmann equation and the numerical method used by this software package to solve it are described in Ref. [46]. The numerical solution generated by this code is shown in Fig. 3.5 for four different values of E/P , which is the ratio of root-mean-squared electric field to gas pressure. For the simulations of helium

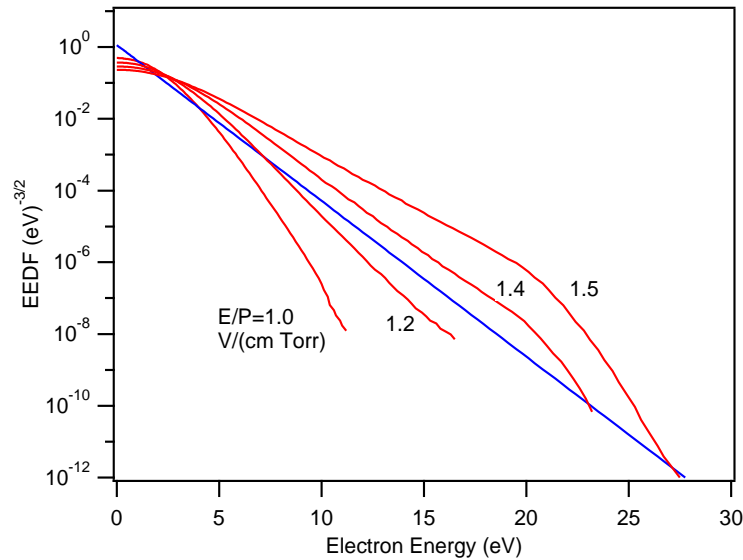


Figure 3.5: The EEDF for helium at several levels of E/P (red curves) together with the Maxwellian EEDF with $T_e = 1$ eV (blue curve).

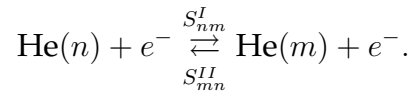
METs in this thesis a typical value of E/P is roughly 1 V/(cm Torr). Together with the numerical solutions in Fig. 3.5 the Maxwellian EEDF for an electron temperature of 1 eV (11600 K) is also shown as the blue curve. This value of electron temperature was chosen for the Maxwellian EEDF because it is typical of those values which were calculated for the helium METs in Chapter 4. The corresponding value of electron temperature for the EEDF at 1 V/(cm Torr) in Fig. 3.5 is 1.1 eV and for the EEDF at 1.5 V/(cm Torr) it is 1.8 eV. The Maxwellian EEDF is straight throughout the entire range of electron energy, and it is evident from Fig. 3.5 that as E/P is increased by 50% the magnitude of the tail of the EEDF (that part of the curve beyond 5 eV) changes by a considerable amount. Under the conditions

which were calculated for the helium METs in this thesis the tail of true EEDF is less than that of the Maxwellian EEDF as is evident in Fig. 3.5, and this suggests that the ionization and excitation rates calculated by the numerical model in this chapter are therefore higher than the actual rates for helium. Therefore in order to maintain the same ionization and excitation rates as those calculated assuming a Maxwellian EEDF the true electric field and hence the true electron temperature would have to be greater than the corresponding calculated values assuming a Maxwellian EEDF. Fig. 3.5 suggests that true electric field would have to be no more than 50 % greater in order to maintain a similar level of ionization as that calculated assuming a Maxwellian EEDF. Since solving the electron Boltzmann for the EEDF at every point in the computational domain is time prohibitive and since assuming a Maxwellian EEDF would most likely lead to errors in the macroscopic properties which are no greater than a factor of two, this assumption was made for helium in this thesis, even though the true EEDF is not Maxwellian.

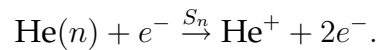
3.2.3 Plasma Model for Helium

The plasma model for helium includes source terms for the net rate of production of several different species including helium atoms in the ground state, the two helium metastable states, two additional electronically excited levels, and electrons. As mentioned before, in this thesis it is always assumed that the number density of electrons is equal to the number density of ions, where in the case of the plenum section of the MET this means helium molecular ions. According to the LS coupling rules, the helium atom can be divided into two sets of excited states, singlet and triplet states. The ground state of helium is a singlet state and it is denoted as 1^1S . The two helium metastable states are denoted 2^1S and 2^3S , for the singlet and triplet states respectively. The two additional excited states which are considered are the 2^1P and the 2^3P states. Helium ions are labeled as He^+ . Three distinct types of collisional and radiative processes, in addition to dissociative recombination, are considered when calculating the individual species mass density source terms, Ω_i for helium plasmas. These processes are listed below.

(a) Excitation and de-excitation by electron collisions



(b) Ionization by electron impact



(c) Radiative decay of electronically excited states by spontaneous emission



There are a total of seven excitation reactions for helium that are considered in the plasma model. The first seven lines of Table 3.2 consist of these excitation reactions, and in each case the energy states involved in the reaction are indicated. The remaining five lines of Table 3.2 consist of the five ionization reactions for helium considered in the plasma model. Ionization from the ground state and from each of the excited states is included in the model. Absent from the above model are Penning ionization processes. In addition many more radiative states could also be included in the model. In the interests of computational efficiency it was decided that the model would be restricted to the processes outlined above, together with dissociative recombination, in the hope that these alone would give an accurate representation of the plasmas considered in this thesis. This may be true for a number of reasons including the fact that the ionization level is low, typically much less than 10^{-3} , and the mass fractions of excited states are low as well, making radiative energy transfer from spontaneous emission not important in the overall energy balance. It is important in determining the species concentrations, however. Three radiative decay processes are considered in the plasma model, involving the optical transitions from the 2^1P level to both the 2^1S level and the 1^1S level, and the optical transition from the 2^3P level to the 2^3S level. The corresponding model for argon plasmas is considered next, followed by a discussion of how the rate coefficients for both helium and argon were calculated.

3.2.4 Plasma Model for Argon

The plasma model for argon includes the same total number of species, in a similar fashion as helium. These species include argon atoms in the ground state, the two argon metastable states, two additional electronically excited levels, and electrons. Unlike helium, argon is characterized by the $j_c - K$ coupling scheme [47], in which the orbital angular momentum of the excited electron couples with the core angular momentum, j_c to give the angular momentum K . The K angular momentum then couples with the spin of the excited electron to generate the total angular momentum of the argon atom. The ground state of argon is denoted as 1S_0 . The two metastable states are labeled $4s'[1/2]_0$ and $4s[3/2]_2$, respectively. The two additional radiative states correspond to the $4s'[1/2]_1$ and $4s[3/2]_1$ levels.

The collisional, radiative model for argon plasmas includes the same processes as the model for helium plasmas. There are ten electronic excitation reactions for argon in the model, and the species involved in these reactions are shown in the first ten lines of Table 3.3. In addition to the excitation reactions, there are five ionization reactions, including ionization from the ground state and each of the excited states. As far as radiative transitions are concerned, spontaneous emission from both the $4s'[1/2]_1$ and $4s[3/2]_1$ levels to the ground state is considered.

3.2.5 Rate Coefficients

The parameters used for determining the rate coefficients for ionization and excitation are now presented. For electronic excitation the rate coefficient for the reaction involving species n and m is S_{nm}^I and the corresponding de-excitation rate coefficient is S_{mn}^{II} . The forward rate coefficient, S_{nm}^I , is obtained by integrating the appropriate cross-section over a Maxwellian electron energy distribution function for different values of electron temperature. The corresponding Arrhenius coefficients, A and N , are then determined by fitting the results to the following formula

$$S_{nm}^I = AT_e^N \exp \frac{-\Delta\epsilon_{mn}}{k_b T_e}, \quad (3.15)$$

where T_e is in Kelvin. The cross-sections for the above processes of electronic excitation by electron impact were taken from a compilation of experimental data for helium given in Ref. [44], and for argon in Ref. [40]. The numerical integration was performed using gaussian quadratures [48]. The backward rate coefficient, S_{mn}^{II} , is determined using the forward rate coefficient and the Klein-Rosenland formula [49]. When this is done the backward rate coefficient can be written as

$$S_{mn}^{II} = S_{nm}^I \frac{g_n}{g_m} \exp \frac{\Delta\epsilon_{mn}}{k_b T_e}. \quad (3.16)$$

In the equations above g_n is the degeneracy of the initial state n and g_m is the degeneracy of the upper state m .

The rate coefficient for the electron impact ionization of species n is S_n and the corresponding three-body recombination rate coefficient (involving an electron as the third body) is β_n . As in the case of excitation the forward rate coefficient for ionization, S_n , is obtained by integrating the appropriate cross-section over a Maxwellian electron energy distribution function for different temperatures and fitting the result to the formula

$$S_n = AT_e^N \exp \frac{-\Delta\epsilon_{cn}}{k_b T_e}, \quad (3.17)$$

where $\Delta\epsilon_{cn}$ is the ionization energy from level n . For those calculations concerning the subsonic plenum section of the MET, dissociative recombination with molecular ions is the dominant process and three-body recombination is not considered. In the supersonic section convection is the dominant electron loss mechanism, however in the calculations of supersonic energy addition with argon in Chapter 6 three-body recombination involving an electron as the third body was also included. The rate coefficient for three-body recombination, β_n , can be written in terms of the forward ionization rate coefficient, S_n , as

$$\beta_n = S_n \frac{g_n}{2} \left(\frac{h^2}{2\pi m_e k_b T_e} \right)^{3/2} \exp \frac{\Delta\epsilon_{cn}}{k_b T_e}. \quad (3.18)$$

The overall rate of mass production of species i , Ω_i , is computed by adding the contributions from all the net ionization and excitation reactions involving species i . For those species which spontaneously decay to a lower level, this rate process is included in Ω_i as well. The spontaneous emission rate coefficients, A_{nm} , for the relevant transitions in helium and argon, mentioned above, were obtained from Ref. [50] and Ref. [51], respectively.

The set of parameters used to determine the rate coefficients for the excitation and ionization of helium in the current model is given in Table 3.2. The corresponding set for argon is given in Table 3.3.

Table 3.2: Parameters Used to Find the Rate Coefficients for Helium

-	Lower State (n)	Upper State (m)	A (m^3/sec)	N -	g_n -	g_m -	$\Delta\epsilon_{mn}$ (eV)
1	1^1S	2^1S	1.74×10^{-17}	0.365	1	1	20.6
2	1^1S	2^3S	1.35×10^{-15}	0.0655	1	3	19.8
3	2^1S	2^1P	2.04×10^{-13}	0.241	1	3	0.600
4	2^1S	2^3P	6.58×10^{-12}	-0.470	1	9	0.340
5	2^3S	2^1S	5.48×10^{-12}	-0.486	3	1	0.800
6	2^3S	2^1P	6.45×10^{-13}	-0.364	3	3	1.40
7	2^3S	2^3P	3.19×10^{-14}	0.354	3	9	1.14
8	1^1S	He^+	4.72×10^{-18}	0.635	1	-	24.6
9	2^1S	He^+	7.62×10^{-16}	0.502	1	-	3.96
10	2^1P	He^+	1.34×10^{-15}	0.477	3	-	3.36
11	2^3P	He^+	4.11×10^{-16}	0.528	3	-	4.76
12	2^3P	He^+	1.04×10^{-15}	0.489	9	-	3.62

Table 3.3: Parameters Used to Find the Rate Coefficients for Argon

-	Lower State (n)	Upper State (m)	A (m^3/sec)	N -	g_n -	g_m -	$\Delta\epsilon_{mn}$ (eV)
1	1^1S_0	$4\text{s}[3/2]_2$	2.34×10^{-15}	-0.0408	1	5	11.5
2	1^1S_0	$4\text{s}[3/2]_1$	2.22×10^{-17}	0.396	1	3	11.6
3	1^1S_0	$4\text{s}'[1/2]_0$	3.21×10^{-16}	-0.0367	1	1	11.7
4	1^1S_0	$4\text{s}'[1/2]_1$	5.09×10^{-17}	0.397	1	3	11.8
5	$4\text{s}[3/2]_2$	$4\text{s}[3/2]_1$	4.17×10^{-17}	-0.0272	5	3	0.0760
6	$4\text{s}[3/2]_2$	$4\text{s}'[1/2]_0$	1.30×10^{-18}	-0.0218	5	1	0.175
7	$4\text{s}[3/2]_2$	$4\text{s}'[1/2]_1$	3.76×10^{-18}	-0.0188	5	3	0.280
8	$4\text{s}[3/2]_1$	$4\text{s}'[1/2]_0$	2.04×10^{-17}	-0.0255	3	1	0.0990
9	$4\text{s}[3/2]_1$	$4\text{s}'[1/2]_1$	6.43×10^{-18}	-0.0208	3	3	0.204
10	$4\text{s}'[1/2]_0$	$4\text{s}'[1/2]_1$	2.88×10^{-16}	-0.501	1	3	0.105
11	1^1S_0	Ar^+	3.66×10^{-17}	0.654	1	-	15.8
12	$4\text{s}[3/2]_2$	Ar^+	6.48×10^{-15}	0.300	5	-	4.25
13	$4\text{s}[3/2]_1$	Ar^+	6.82×10^{-15}	0.298	3	-	4.17
14	$4\text{s}'[1/2]_0$	Ar^+	7.31×10^{-15}	0.295	1	-	4.07
15	$4\text{s}'[1/2]_1$	Ar^+	7.88×10^{-15}	0.292	3	-	3.97

3.3 Transport Properties

In computing the viscous stress tensor and the heat flux in the gas dynamics model both heavy particle and electron transport processes are considered. For the heavy particles viscosity and thermal conductivity are calculated, and for the electrons, the complex electrical conductivity is calculated.

The viscosity and thermal conductivity for pure helium or argon atoms are taken from the results of kinetic theory for a monatomic gas [52],

$$\begin{aligned}\mu_i &= \frac{5\sqrt{\pi m_i k_b T}}{16\pi\Omega^{(2,2)}} \\ k_i &= \frac{25\sqrt{\pi m_i k_b T} c_v}{32\pi\Omega^{(2,2)}},\end{aligned}\quad (3.19)$$

where m_i is the atomic mass, $\Omega^{(2,2)}$ is a collision integral, evaluated assuming a Lennard-Jones potential, and c_v is the specific heat of species i . For pure argon or helium ions, either atomic or molecular, the corresponding expressions are [29]

$$\begin{aligned}\mu_i &= 0.72 \frac{\sqrt{m_i} (4\pi\epsilon_0)^2 (kT)^{5/2}}{\sqrt{\pi} e^4 \Lambda} \\ k_i &= 2.925 \frac{k (4\pi\epsilon_0)^2 (kT)^{5/2}}{\sqrt{\pi} m_i e^4 \Lambda},\end{aligned}\quad (3.20)$$

where in this case, m_i is the ion mass. Λ is the Coulomb logarithm, for which the following formula is used [29], $\Lambda = \log 1.24 \times 10^7 \sqrt{T_e^3/N_e}$. The viscosity of the mixture, μ_h , is determined from the pure atom and ion values, μ_i , using an empirical mixture rule [53]

$$\begin{aligned}\mu_h &= \sum_i x_i \mu_i [\sum_j x_j \Phi_{ij}], \\ \Phi_{ij} &= \frac{\left[1 + \left(\frac{\mu_i}{\mu_j}\right)^{1/2} \left(\frac{w_j}{w_i}\right)^{1/4}\right]^2}{8 \left(1 + \frac{w_i}{w_j}\right)},\end{aligned}\quad (3.21)$$

where x_i and w_i are the mole fraction and molecular weight of species i . The thermal conductivity of the mixture, k_h , is determined using the same formula, with μ_i replaced with k_i . Now electron transport is discussed.

For both helium and argon plasmas, considered in this thesis, the only electron transport property considered is the complex electrical conductivity, σ , previously defined in terms of the microwave joule heating rate. This quantity is calculated using the Frost mixture rule formula [29], involving the following integration of the electron energy distribution

$$\sigma = \frac{4N_e e^2}{3\sqrt{\pi} m_e} \int_0^\infty \frac{X^{3/2} \exp -X}{\nu_c + i\omega} dX,$$

where ν_c is another electron collision frequency term, different from ν_{eH} , and ω is the angular frequency of the microwave field. The electron energy has been non-dimensionalized by $k_b T_e$ in the integral above. This integral is solved in numerical simulations by using a ten point Gauss-Laguerre formula [48].

3.4 Microwave Field Model

The spatial distribution of the microwave field inside the thruster influences the plasma properties and the joule heating profile, and therefore any model that accurately represents a microwave thruster must include a detailed description of the microwave field. As mentioned previously, for a TM_{01} mode in a cylindrical waveguide there are three components of the electromagnetic field, E_r , E_z , and H_θ . The relationships among these components are expressed by Maxwell's equations. When considering the heating of a plasma by microwaves, only the electric field components are important, evident in the expression for the joule heating rate, Eqn. 3.5. The microwave model in this thesis includes both radial and axial electric fields, expressed in terms of the corresponding complex field amplitudes.

When considering a time periodic electromagnetic field of angular frequency ω it is convenient to describe any one of the components of the field, represented by Φ , in terms of a complex amplitude, in the following way

$$\Phi = \frac{1}{2} (\Phi e^{-i\omega t} + \Phi^* e^{i\omega t}), \quad (3.22)$$

as mentioned in Chapter 2. By writing each component in the form of Eqn. 3.22, substituting into Maxwell's equations and simplifying, it can be shown that the complex amplitude of each of the components of the electromagnetic field obeys the Helmholtz wave equation [26]. In cylindrical coordinates the Helmholtz equation for the complex amplitude of the axial electric field component, E_z is

$$\frac{1}{r} \frac{\partial}{\partial r} r \frac{\partial E_z}{\partial r} + \frac{\partial^2 E_z}{\partial x^2} + \beta^2 E_z = 0. \quad (3.23)$$

The corresponding equation for the complex amplitude of the radial component, E_r is

$$\frac{1}{r} \frac{\partial}{\partial r} r \frac{\partial E_r}{\partial r} + \frac{\partial^2 E_r}{\partial x^2} + \left(\beta^2 - \frac{1}{r^2} \right) E_r = 0. \quad (3.24)$$

In these equations the complex propagation constant β is such that

$$\beta^2 = \mu \epsilon \omega^2 \left(1 - i \frac{\sigma}{\epsilon_0 \omega} \right),$$

where ϵ_0 is the dielectric permittivity of free space and σ is the complex conductivity of the plasma. In solving these equations for the complex field components, the non-linear interaction between the field and the plasma, due to the effects of the complex conductivity, is captured. It will be shown later that under certain circumstances the field inside the microwave thruster is influenced strongly by the presence of the plasma and is highly distorted, compared with the idealized field pattern presented in Chapter 2. The equations for the complex field components, Eqn. 3.23 and Eqn. 3.24, are solved in the model, using a finite-element technique that is now discussed.

3.4.1 Finite-Element Technique

The finite-element method is used to solve both Eqn. 3.24 and Eqn. 3.23 separately. The finite-element method has been applied successfully to many problems involving partial differential equations in such diverse areas as fluid mechanics, structural mechanics, heat transfer and electromagnetic wave propagation [54]. This method breaks a two dimensional computational domain into a series of finite elements, triangles, quadrilaterals, etc, that fill the entire domain and whose corners are the points where the discrete solution to the partial differential equation is determined. A critical assumption is that at every point inside one of these finite elements, the solution can be expressed as a weighted sum of the respective values at the corners of that particular finite element. There is an influence function, ψ_k , associated with each point, x_k, r_k , on the grid. These influence functions are used to compute the appropriate weight when performing the sum. The finite-element method solves a weighted-integral form of the equation, and in so doing a matrix is generated, implicitly relating each point on the grid to a group of other points on the grid. There is one equation for each grid point. For certain two dimensional problems of interest, such as the one considered in this thesis, the finite-element matrix is band-diagonal, and can be inverted using a standard numerical algorithm [48].

In order to apply the finite-element method to solve Eqn. 3.24 and Eqn. 3.23, these equations must be written in weighted integral form, which is sometimes referred to as the weak solution form [54]. Consider Eqn. 3.23, for instance, the weighted-integral form is

$$\int \int_A w \left[\frac{\partial}{\partial r} r \frac{\partial \Phi}{\partial r} + \frac{\partial^2 r \Phi}{\partial x^2} + \beta^2 r \Phi \right] dx dr = 0, \quad (3.25)$$

where E_z has been replaced with Φ for notational convenience. The domain of integration in the x, r plane is denoted as A , and w is the weighting function, which can be any one of the influence functions, ψ_k . In evaluating this integral, $\Phi(x, r)$ is first expressed as the sum of influence functions, $\sum \Phi_j \psi_j(x, r)$, where Φ_j is the

value of Φ at one of the discrete points on the grid and $\psi_j(x, r)$ is the influence function associated with that point. Following the approach outlined in Ref. [54], the integral above can be transformed into the form,

$$\begin{aligned} \int \int_A \Sigma_j \Phi_j \left[-r \left(\frac{\partial \psi_k}{\partial r} \frac{\partial \psi_j}{\partial r} + \frac{\partial \psi_k}{\partial x} \frac{\partial \psi_j}{\partial x} \right) + \beta^2 r \psi_k \psi_j \right] dx dr \\ + \oint \psi_k r \left[\frac{\partial \Phi}{\partial x} dr - \frac{\partial \Phi}{\partial r} dx \right] = 0. \end{aligned} \quad (3.26)$$

For each ψ_k , an equation of the form 3.26 is generated, forming an implicit set of algebraic equations which can be solved for all the unknown Φ_k values on the grid. The second term of Eqn. 3.26 is a line integral along the boundary of the domain, and in this integral Φ is not written as a series of ψ_k functions, but rather the treatment of Φ on the boundaries is done separately as discussed later. The line integral term is only present in those cases when (x_k, r_k) is on a physical boundary.

It is common practice in finite-element problems to choose ψ_k so that, in each of the finite elements containing the grid point, (x_k, r_k) , the ψ_k function is equal to be the bilinear interpolation function associated with that point and that finite element. Consider for instance a quadrilateral finite element, which has four corners. There are four bilinear interpolation functions associated with this finite element, one for each of the corners. In this thesis quadrilateral finite elements are used. The bilinear interpolation functions for a quadrilateral finite element can be expressed most conveniently by transforming to a local coordinate system, (u^*, v^*) , where each of the corners becomes either $(-1, -1)$, $(1, -1)$, $(1, 1)$, or $(-1, 1)$. In the (u^*, v^*) coordinate system the bilinear interpolation functions are [54]

$$\begin{aligned} \psi_1 &= \frac{(u^* - 1)(v^* - 1)}{4}, \\ \psi_2 &= \frac{-(u^* + 1)(v^* - 1)}{4}, \\ \psi_3 &= \frac{(u^* + 1)(v^* + 1)}{4}, \\ \psi_4 &= \frac{-(u^* - 1)(v^* + 1)}{4}, \end{aligned} \quad (3.27)$$

starting first with the function for the lower left corner and moving counterclockwise around the element. Choosing ψ_k to be one of these interpolation functions creates a stencil including (x_k, r_k) and its eight nearest neighbors, when evaluating Eqn. 3.26 in a region away from a boundary.

The finite-element equation for Φ at a point (i, j) on the grid, denoted $\Phi^{i,j}$, contains nine terms, each of which is a sum of individual contributions from the four finite elements that contain $\Phi^{i,j}$. For the point (i, j) , the four finite elements that

surround it are the $(i-1, j-1)$, $(i, j-1)$, (i, j) and $(i-1, j)$ elements on the grid. The value of β^2 from Eqn. 3.23 is computed at the center of each of these finite elements by the fluid solver, as discussed previously in this chapter. Using the notation above, the finite-element equation for $\Phi^{i,j}$, at a point away from a boundary, is

$$\begin{aligned} & B_{13}^{i-1,j-1} \Phi^{i-1,j-1} + [B_{34}^{i-1,j-1} + B_{12}^{i-1,j}] \Phi^{i-1,j} + B_{24}^{i-1,j+1} \Phi^{i-1,j+1} + \\ & [B_{23}^{i-1,j-1} + B_{14}^{i,j-1}] \Phi^{i,j-1} + [B_{33}^{i-1,j-1} + B_{22}^{i-1,j} + B_{11}^{i,j} + B_{44}^{i,j-1}] \Phi^{i,j} + \\ & [B_{23}^{i-1,j} + B_{14}^{i,j}] \Phi^{i,j+1} + B_{24}^{i,j-1} \Phi^{i+1,j-1} + \\ & [B_{34}^{i,j-1} + B_{12}^{i,j}] \Phi^{i+1,j} + B_{13}^{i,j} \Phi^{i+1,j+1} = 0, \end{aligned} \quad (3.28)$$

where $B_{m,n}^{i,j}$ is the contribution to the finite-element matrix from element (i, j) due to the interaction of influence functions ψ_m and ψ_n . For finite element (i, j) , $B_{m,n}^{i,j}$ is computed as

$$B_{m,n}^{i,j} = \int \int_{A^*} \left[-r \left(\frac{\partial \psi_m}{\partial r} \frac{\partial \psi_n}{\partial r} + \frac{\partial \psi_m}{\partial x} \frac{\partial \psi_n}{\partial x} \right) + \beta^2 r \psi_m \psi_n \right] dx dr, \quad (3.29)$$

where the domain of integration, A^* , spans the area of the finite element (i, j) , and it is assumed that β^2 is constant across the element. For certain points on a boundary there are additional terms present on the right hand side of Eqn. 3.28. Eqn. 3.28 is valid when $\Phi = \mathbf{E}_r$ also, but in this case $B_{m,n}^{i,j}$ is

$$B_{m,n}^{i,j} = \int \int_{A^*} \left[-r^2 \left(\frac{\partial \psi_m}{\partial r} \frac{\partial \psi_n}{\partial r} + \frac{\partial \psi_m}{\partial x} \frac{\partial \psi_n}{\partial x} \right) - r \psi_n \frac{\partial \psi_m}{\partial r} + (\beta^2 r^2 - 1) \psi_m \psi_n \right] dx dr. \quad (3.30)$$

In the numerical simulations to follow, the double integrals above are calculated for any given finite element by first transforming to the local coordinate system, (u^*, v^*) , and computing the appropriate Jacobian, then using a ten-point Gauss-Legendre formula to evaluate each dimension of the integral [48]. After computing the $B_{m,n}^{i,j}$ terms, the finite element matrix is formulated. Because of the nine point stencil this matrix is band-diagonal, and it is inverted using an optimized L-U decomposition algorithm for band-diagonal matrices [48]. The treatment of the boundary conditions is discussed next.

3.4.2 Boundary Conditions

When formulating the boundary conditions for a finite-element problem it is necessary to specify either the function Φ or its normal derivative at the boundary,

$$\frac{\partial \Phi}{\partial \hat{n}} ds = \frac{\partial \Phi}{\partial x} dr - \frac{\partial \Phi}{\partial r} dx. \quad (3.31)$$

How these boundary conditions are specified is now reviewed.

The electric field vector at the surface of a perfect conductor is normal to the surface, $\mathbf{E} \times \hat{n} = 0$. All waveguide surfaces, shorting plates and the stainless steel nozzle in the subsonic stage, are assumed to be perfect conductors since at microwave frequencies the skin depth is such that the microwave field only penetrates a few microns into the metal. Along the waveguide boundary, $r = a$ with a being the waveguide radius, it is true that $\mathbf{E}_z = 0$, since tangential electric fields cannot exist. It is not necessary to include the equation for this boundary point in formulating the finite-element matrix. In the other equations which contain the boundary point, \mathbf{E}_z is set equal to zero. The corresponding boundary condition for the radial electric field, when $r = a$, is $\partial r \mathbf{E}_r / \partial r = 0$, which comes directly from Maxwell's equations and the fact that $\mathbf{E}_z = 0$. This implies that along the $r = a$ boundary

$$\frac{\partial \mathbf{E}_r}{\partial \hat{n}} ds = \mathbf{E}_r \frac{dz}{r}. \quad (3.32)$$

For a finite element just below the waveguide boundary the above expression relates the normal derivative of \mathbf{E}_r to its functional value on the top edge of finite element. When this is substituted into the line integral in Eqn. 3.26, \mathbf{E}_r can be written in terms of a series involving the two ψ_k functions corresponding to the top two points of the element. The line integral in Eqn. 3.26 is then evaluated numerically in a similar manner as the double integral, and for the case of \mathbf{E}_r , the r which appears in the integrand must be replaced with r^2 when evaluating this line integral. Therefore for each point on the boundary, \mathbf{E}_r is unknown and an equation of the type 3.28 is written for this unknown with some of the coefficients, $B_{m,n}^{i,j}$, modified due to the inclusion of the line integral on the boundary.

Along the wall of the conical nozzle in the subsonic stage, $\mathbf{E} \times \hat{n} = 0$ requires that $\mathbf{E}_z / \mathbf{E}_r = \tan \theta$, where θ is the half angle of the conical nozzle. When evaluating the line integral from Eqn. 3.26 along this boundary, the tangent of the nozzle half angle is equal to $-dr/dz$, and with this expression it is possible to show that for the axial field

$$\frac{\partial \mathbf{E}_z}{\partial \hat{n}} ds = \mathbf{E}_z \frac{dz}{r}, \quad (3.33)$$

and for radial field

$$\frac{\partial \mathbf{E}_r}{\partial \hat{n}} ds = \mathbf{E}_r \frac{dz}{r}. \quad (3.34)$$

These expressions are used to evaluate the line integrals for \mathbf{E}_z and \mathbf{E}_r along the nozzle wall boundary in the manner just described.

At the subsonic nozzle exit plane, where the flow exits the subsonic part of the thruster and enters the supersonic part, the electric field is evanescent, since the

nozzle throat diameter is much smaller than the waveguide radius. An evanescent field decays to zero in the following fashion,

$$\frac{\partial \Phi}{\partial x} = -\sqrt{(x_{01}/a)^2 - \mu\epsilon_0\omega^2}\Phi, \quad (3.35)$$

where in this case a is the radius of the throat. Along the nozzle throat boundary, $dz = 0$, the above equation is used to specify the normal derivatives of both \mathbf{E}_z and \mathbf{E}_r , in terms of the functions themselves. The evanescent field is calculated for the subsonic part of the thruster only.

The supersonic cavity is formed in the two-stage thruster by shorting a section of waveguide at the throat where the flow exits from the subsonic part of the thruster. It is assumed the waveguide is completely closed by the shorting plate. The evanescent part of the field caused by the hole in the shorting plate due to the nozzle throat is neglected because it decays to zero in a relatively short distance. The supersonic waveguide section is filled completely with the dielectric nozzle for the supersonic expansion. Along the shorting plate boundary the following conditions hold true, $\mathbf{E}_r = 0$ and $\partial \mathbf{E}_z / \partial z = 0$. At the waveguide centerline, for both the subsonic and supersonic sections, the cylindrical symmetry of the problem implies that $\mathbf{E}_r = 0$ and $\partial \mathbf{E}_z / \partial r = 0$.

At the microwave inlet port for both the subsonic and supersonic sections, the following procedure is used to specify the values of \mathbf{E}_r and \mathbf{E}_z . The classical solution for waves propagating in both directions in a cylindrical waveguide follows from the presentation in Chapter 2, Eqn. 2.1 and Eqn. 2.3,

$$\mathbf{E}_z = A^+ J_0 \left(\frac{x_{01}r}{a} \right) \left[e^{-\frac{i2\pi z}{\lambda_g}} + X e^{\frac{i2\pi z}{\lambda_g}} \right], \quad (3.36)$$

$$\mathbf{E}_r = iA^+ \frac{2\pi a}{\lambda_g x_{01}} J_1 \left(\frac{x_{01}r}{a} \right) \left[e^{-\frac{i2\pi z}{\lambda_g}} - X e^{\frac{i2\pi z}{\lambda_g}} \right], \quad (3.37)$$

where A^+ is the complex amplitude coefficient and X is the reflection coefficient. The axial component of the field, \mathbf{E}_z , at the inlet boundary is specified assuming a normalized electric field such that $\mathbf{E}_z = J_0(x_{01}r/a)$. After the finite element solution is generated, the reflection coefficient is determined by substituting the finite element solution at two closely spaced points near the inlet into Eqn. 3.37 separately, and then taking the ratio of the two equations. The value of X , so obtained, is then used with Eqn. 3.37 to scale the \mathbf{E}_z solution, and with Eqn. 3.37 to specify \mathbf{E}_r at the inlet, assuming that $A^+ = 1$ in both cases. The finite-element solution for \mathbf{E}_r is generated and subsequently the source term, J from Eqn. 3.5, is computed for each cell on the grid. The source terms are added together and finally the value of A^+ is found, so that the desired amount of microwave power is absorbed by the flow. Once A^+ is determined the complete solution for the complex electric field is rescaled by multiplying by this factor. The computed values of J are rescaled by A^{+2} .

3.5 Validation of the Fluid Solver

Now that all the elements of the physical model have been covered, the numerical procedure used to solve Eqn. 3.1 is validated by looking at some classical test cases involving supersonic flow over a cone and compressible boundary layers over a flat plate. It is important to stress that the underlying numerical techniques used to solve the fluid equations in this thesis are well established, and the numerical approach adopted here has been shown by many others to be both robust and accurate [34–36]. The purpose of validation in the context of this thesis is to verify that no errors have been made implementing these well-known numerical techniques, since the code generated for the model was built from scratch.

3.5.1 Conical Flow

The first test case involves supersonic flow over a cone with a half angle, θ_c , neglecting the effects of heat transfer and viscosity. This problem is axisymmetric in nature, and it is convenient to use a polar coordinate system with the origin at the apex of the cone. The cone extends out to infinity in this idealized problem. Under such conditions, a shock wave is present at an angle of β_s , relative to the centerline of the cone. The properties of the flow between the shock wave and the cone depend on the properties in the free stream, the cone half angle, and the angle of the flow relative to the centerline, θ . This dependence is described by the Taylor-Maccoll equation for conical flows [55]

$$\frac{\gamma - 1}{2} \left[1 - V_r^2 - \left(\frac{dV_r}{d\theta} \right)^2 \right] \left[2V_r + \frac{dV_r}{d\theta} \cot \theta + \frac{d^2V_r}{d\theta^2} \right] - \left(\frac{dV_r}{d\theta} \right)^2 \left[V_r + \frac{d^2V_r}{d\theta^2} \right] = 0, \quad (3.38)$$

where V_r is the radial velocity component, and $V_\theta = dV_r/d\theta$ is the velocity component in the θ direction. This equation can be written as a system of first order ordinary differential equations, and can be integrated using a Runge-Kutta numerical technique [48]. For a given shock wave angle, the corresponding cone half angle must be found by numerically integrating Eqn. 3.38, starting from immediately behind the shock, until the right value of θ is reached so that $V_\theta = 0$, which is true on the surface of the cone. When doing this, the shock angle, β_s and the normal shock relations [55], are used to find the flow velocity just behind the shock. A shock wave polar for conical flow can be generated in this fashion, by varying the shock angle. Some representative results are shown in Fig. 3.6, for the case when $\gamma = 1.4$. In finding the shock polar, the ratios of density and pressure at the surface of the cone relative to the free stream conditions were tabulated to be used for comparison with the results from the fluid code.

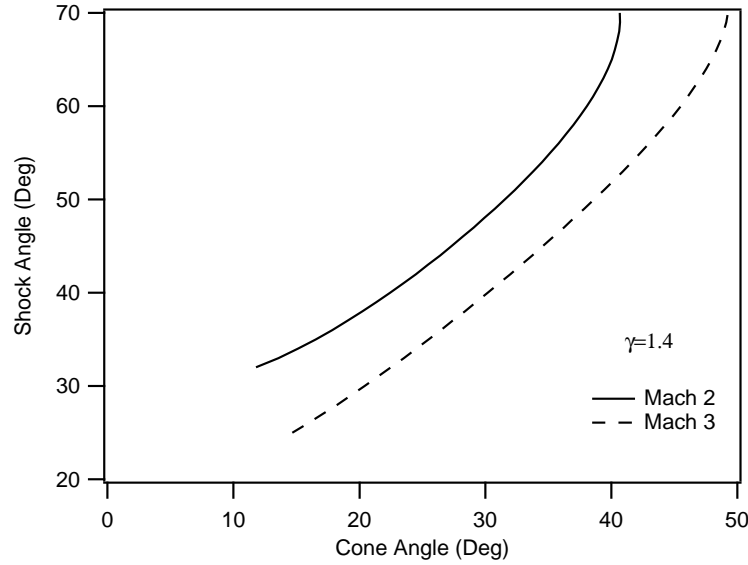


Figure 3.6: Shock angle as a function of cone half angle for two different Mach numbers, found by solving Eqn. 3.38.

Numerical simulations were performed for air at two different Mach numbers, 2 and 3, for two different cone half angles, 20 and 30 degrees, using the fluid code described previously in this chapter. For the case of air γ is equal to 1.4, as opposed to 1.67 for monatomic gases, and for the simulations performed in this section the internal energy was calculated accordingly ($5 R_i T/2$). The surface pressure and density ratios for a supersonic air flow over a 20 degree cone are compared with those predicted by solving Eqn. 3.38, in Table 3.4.

Table 3.4: Pressure and Density Ratios for a 20 Degree Cone

Mach Number	Pressure Ratio Eqn. 3.38	Pressure Ratio Code	Density Ratio Eqn. 3.38	Density Ratio Code
-				
2	1.86	1.91	1.55	1.56
3	2.75	2.76	2.02	1.95

The free stream conditions in the numerical simulation were $\rho = 10^{-2} \text{kg/m}^3$ and $T=500 \text{ K}$. The values calculated using the fluid code are labeled as code and the values calculated by numerically solving Eqn. 3.38 are referred to as Eqn. 3.38 in Table 3.4. The values of pressure and density obtained from the fluid code, displayed in Table 3.4, were averaged over the surface area of the cone. The values

from the fluid code and Eqn. 3.38 agree to within 5% in all cases. The discrepancy between the two is due to two factors, the lack of grid refinement at the apex of the cone and too high a level of numerical dissipation created by the choice of dissipation coefficients. A grid of 70 by 120 cells was used for this numerical simulation, as shown in Fig. 3.7. Twenty longitudinal cells were placed in front of the cone.

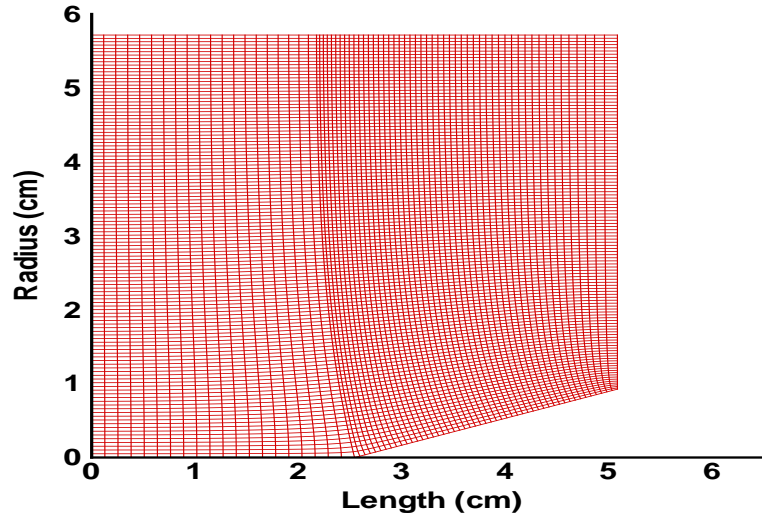


Figure 3.7: Grid used to simulate flow over a 20 degree cone.

The grid consists of the streamlines and lines of constant velocity potential for a two-dimensional, incompressible flow moving through this geometry. These grid lines were found by using the finite-element method to solve the Laplace equation numerically. A similar grid is used for the 30 degree case, which is considered next. In both cases the dissipation coefficients in Eqn. 3.10 were set such that $\alpha_1 = 0.5$ and $\alpha_2 = 0.1$.

Another comparison is made for the same free stream conditions and a cone angle of 30 degrees. The results are shown in Table 3.5. Satisfactory agreement

Table 3.5: Pressure and Density Ratios for a 30 Degree Cone

Mach Number	Pressure Ratio Eqn. 3.38	Pressure ratio Code	Density Ratio Eqn. 3.38	Density Ratio Code
-				
2	2.88	2.79	2.08	1.98
3	4.52	4.53	2.72	2.58

is obtained once again, suggesting that the numerical implementation of the ba-

sic conservation scheme is correct. The second order dissipation coefficient was kept at high value for these calculations, and the fourth order anti-dissipation coefficient was kept low. This is not an optimum situation for capturing a shock wave [36], yet agreement between code and theory is acceptable. By reducing α_1 further and also increasing the anti-dissipation coefficient, α_2 , the numerical dissipation in the problem would be reduced and it would be possible to improve the agreement even further. It becomes necessary to treat the dissipation in this manner when considering boundary layers and transport because too much numerical dissipation can overwhelm the physical dissipation in certain situations, distorting the solution [35].

3.5.2 Compressible Boundary Layers

Now that the numerical implementation of the basic scheme has been tested, the routines for calculating the transport properties of the flow are tested by considering compressible flows over a flat plate. For an incompressible, laminar flow over a flat plate the Navier-Stokes equations can be reduced to a set of boundary layer equations involving the axial velocity u , the distance along the plate, x and the distance above the plate, y . The solution to the boundary layer equations for the velocity profile is the well-known Blasius profile [56], f , such that

$$\frac{u}{u_1} = f(\eta^*), \quad (3.39)$$

where $\eta^* = y\sqrt{u_1/\nu_1 x}$. The free stream quantities are denoted with the subscript 1 above, and ν_1 is the kinematic viscosity μ_{h1}/ρ_1 . Under certain conditions, when the Prandtl number of the flow, $\mu_h c_p/k_h$ is equal to unity, and when the viscosity varies with temperature according to a power-law relationship, such that $\mu_h = \mu_0 (T/T_0)^n$, where n is an integer and T_0 is the flow stagnation temperature, the non-dimensional compressible boundary layer equations can be transformed into a form that is functionally identical to the incompressible case [56]. The Blasius profile is, therefore, the solution for the compressible velocity profile as well, where in this case η^* is replaced with η such that,

$$\eta = \frac{u_1}{\nu_1 x} \int_0^y \frac{T_1}{T} dy. \quad (3.40)$$

The distance above the plate, y , at which the velocity is $u = u_1 f(\eta)$, in the compressible boundary layer can be found by inverting Eqn. 3.40,

$$y = \frac{\nu_1 x}{u_1} \int_0^\eta \frac{T}{T_1} d\eta. \quad (3.41)$$

The temperature ratio relative to free stream conditions in a compressible boundary layer, under the special conditions mentioned above, can be expressed in terms of the Blasius profile [56]. When this is done for the case of an adiabatic plate the result is,

$$\frac{T}{T_1} = 1 + \frac{\gamma - 1}{2} M_1^2 [1 - f^2(\eta)] . \quad (3.42)$$

For the case of a plate with constant surface temperature T_w , the corresponding result is,

$$\frac{T}{T_1} = 1 + \frac{\gamma - 1}{2} M_1^2 [1 - f^2(\eta)] + \frac{T_w - T_0}{T_1} [1 - f(\eta)] . \quad (3.43)$$

In these equations, as before, the subscript 1 denotes the free stream conditions and the subscript 0 denotes the stagnation conditions. Eqn. 3.42 or Eqn. 3.43 can be used with Eqn. 3.41 to find the velocity distribution in a compressible boundary layer and the theoretical profile thus obtained is now compared with numerical results from the fluid code.

A compressible flow over an adiabatic plate was considered first, for two different free stream Mach numbers, 2 and 3. Air was the fluid, with $\gamma = 1.4$ everywhere and with the viscosity varying linearly with temperature, $n = 1$. The free stream value for the viscosity, μ_{h1} was 1.85×10^{-5} kg/m sec, the free stream density was 10^{-2} kg/m³ and the free stream temperature was 500 K in all cases considered. The computational domain consisted of a region surrounding the plate, 5.08 cm in length and 1.27 cm high, with 70 cells distributed linearly along the length and a total of 120 cells in the direction perpendicular to the plate. Seventy of these cells were placed in an exponential distribution in a region 0.254 cm above the plate, so that the sharp gradients near the surface of the plate could be resolved properly. Ten longitudinal cells were placed in front of the plate. The velocity profile in the boundary layer for a Mach 2 flow, as a function of η^* , 2.90 cm from the front edge of the plate, is shown in Fig. 3.8, where the velocity has been non-dimensionalized by the free stream velocity. In the figure, the blue points correspond to the calculated results from the fluid code, and the solid red line refers to the solution obtained by integrating Eqn. 3.42. The temperature profile in the boundary layer is shown in Fig. 3.9. For both velocity and temperature there is relatively good agreement. The code predicts correctly that the adiabatic temperature is roughly 1.8 times the free stream temperature, and the velocity in the boundary layer approaches the free stream value when η^* is about eight. The coefficients of numerical dissipation were set so that $\alpha_1 = 0.25$ and $\alpha_2 = 0.5$ for this calculation, and the remaining calculations in this section. When α_1 was made less than 0.25 or α_2 greater than 0.5 the calculation would not converge properly.

A Mach 3 flow over an adiabatic plate was also simulated, under the same conditions as the previous case. The result for the velocity distribution, 2.90 cm from

the front edge of the plate, is shown in Fig. 3.10 and the corresponding temperature distribution is shown in Fig. 3.11. Agreement between the code predictions and the results using Eqn. 3.42 is good once again. For this Mach number the velocity approaches the free stream value when η^* equals about ten. Shortly before this point there is about a 5% difference between the velocity predicted by the code and the analytic solution as shown in Fig. 3.10. The code predicts that at the surface of the plate the temperature is 2.71 times the free stream temperature, whereas the analytic result is 2.8, representing a 3.5% difference. This suggests that the code is modeling the transport processes correctly, and one more test was done, considering a plate with heat transfer at the surface.

The final test case involves Mach 2 flow over the plate, with the temperature held fixed at the free stream value of 500 K. For this case Eqn. 3.43 is used in place of Eqn. 3.42 to generate the analytic solution. The velocity profile in the boundary layer, as computed by the code under these conditions is shown in Fig. 3.12. There is very good agreement between the analytic solution and the code for the velocity distribution as shown in Fig. 3.12. For this case the velocity in the boundary layer approaches free stream value when η^* is equal to about six, and the code predicts this correctly. Fig. 3.13 shows the temperature distribution predicted by the code. At the surface of the plate the code predicts a temperature ratio of 1.0, as expected, with a maximum temperature ratio of 1.14 occurring at $\eta^* = 1.91$. The analytic solution for the temperature, has a maximum at $\eta^* = 1.75$ and its value is 1.2. The difference in the temperature peaks is close to 5%. As mentioned previously even higher accuracy could be achieved by adjusting the numerical dissipation coefficients further. No attempts were made to do this however, since the accuracy achieved here was considered sufficient.

The rate of convergence of the residual for each fluid variable, for the case of heat transfer through the flat plate, is shown in Fig. 3.14. The mass, axial momentum, radial momentum, and energy residuals are shown, which are the root-mean-square values over the entire grid. In each case it is evident that after thirty thousand steps there is a reduction of at least four orders of magnitude in the value of the residual, indicating a proper convergence to steady state conditions.

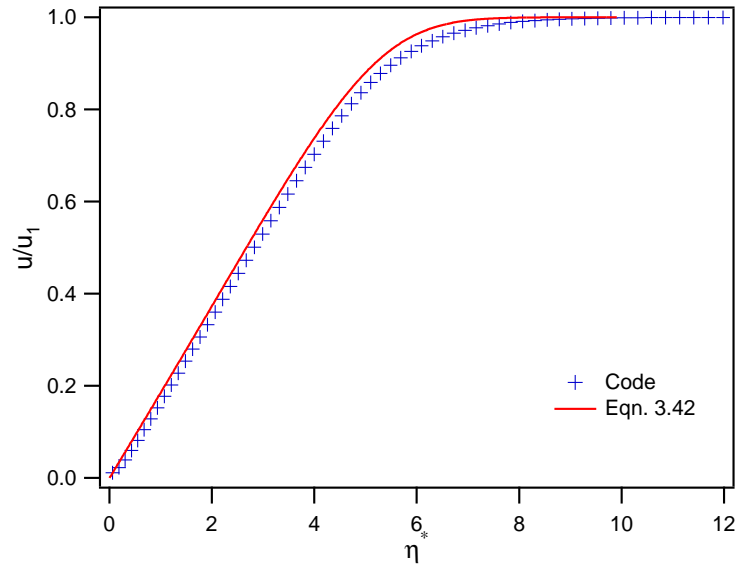


Figure 3.8: Velocity profile for a Mach 2 compressible boundary layer.

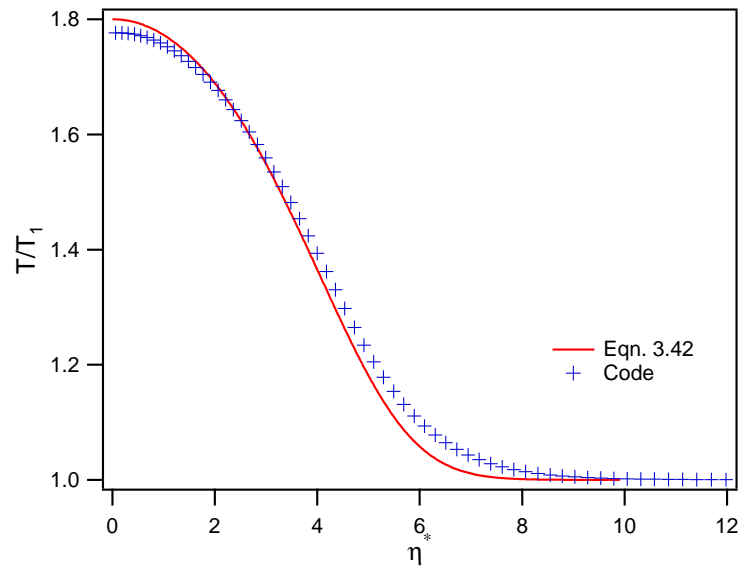


Figure 3.9: Temperature profile for a Mach 2 compressible boundary layer.

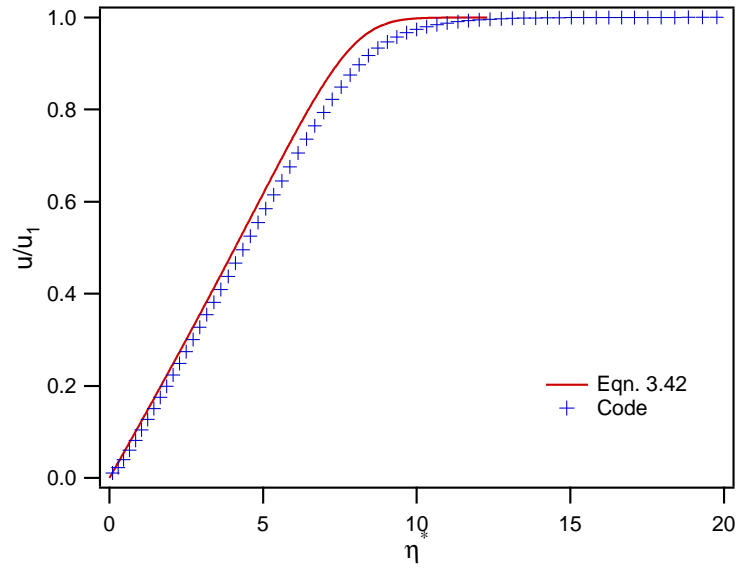


Figure 3.10: Velocity profile for a Mach 3 compressible boundary layer.

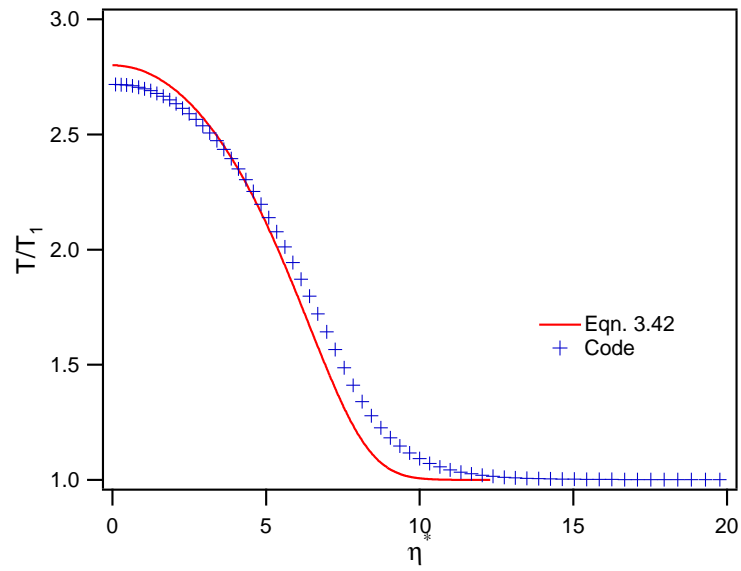


Figure 3.11: Temperature profile for a Mach 3 compressible boundary layer.

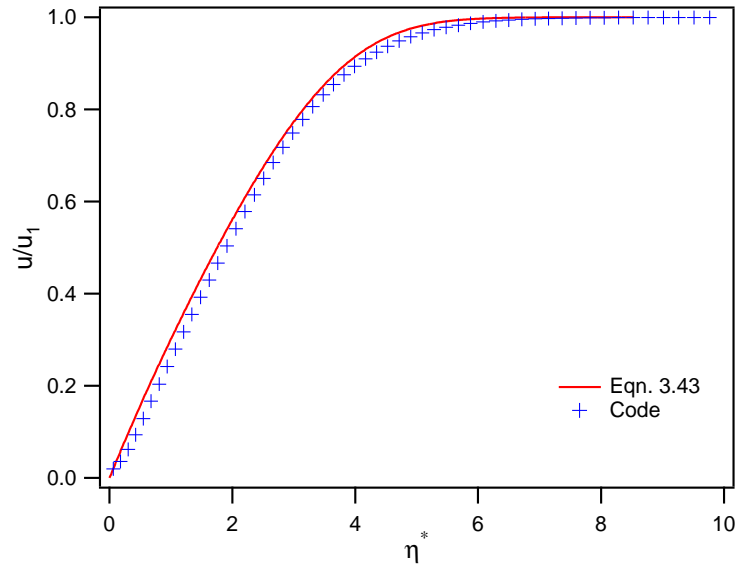


Figure 3.12: Velocity profile for a Mach 2 compressible boundary layer with heat transfer.

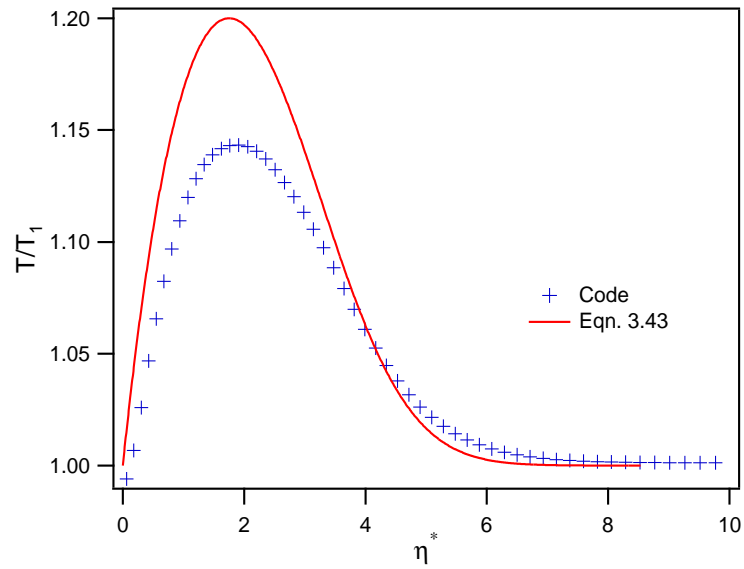


Figure 3.13: Temperature profile for a Mach 2 compressible boundary layer with heat transfer.

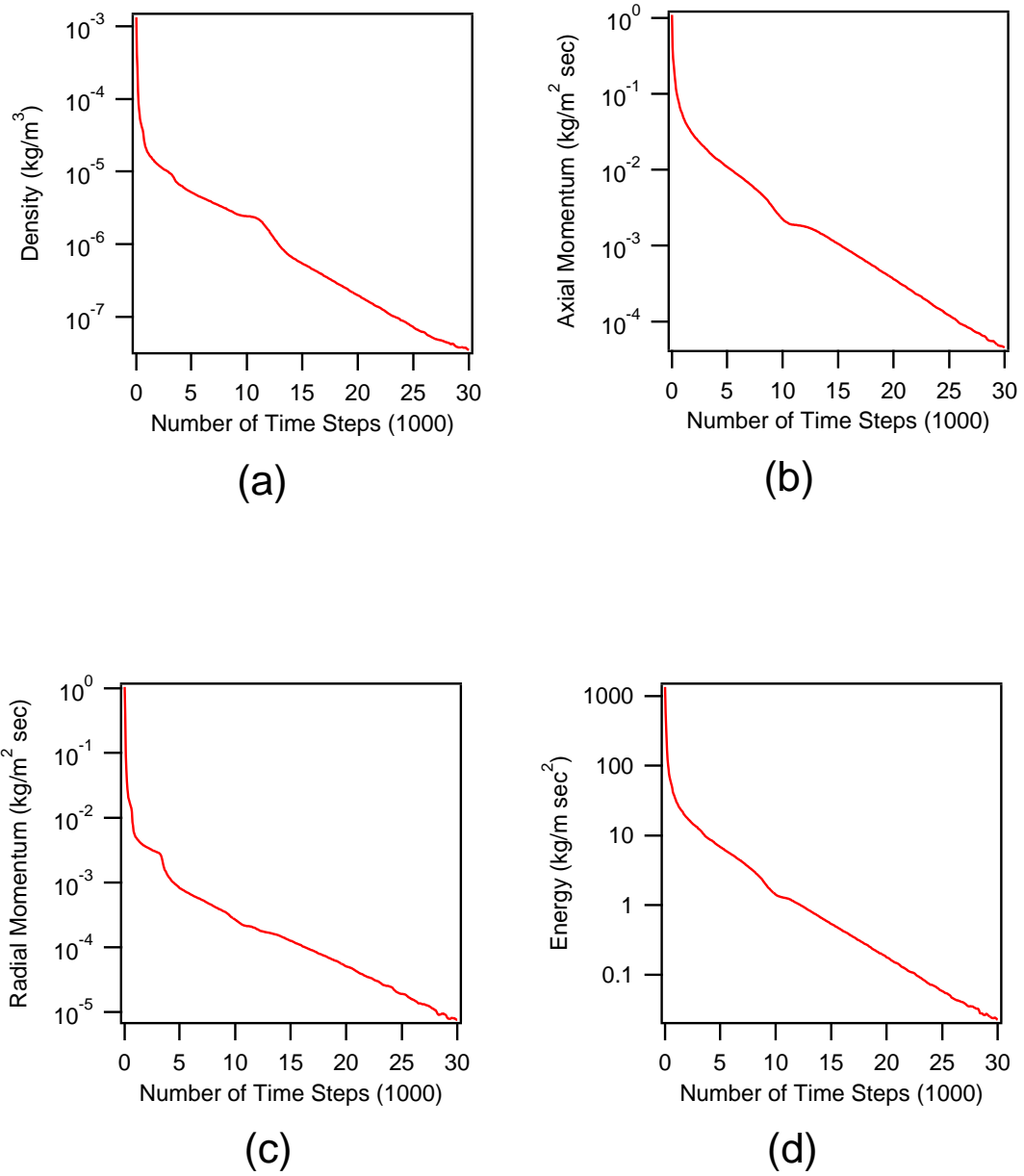


Figure 3.14: Convergence rates of the root-mean-square residuals for the case of a Mach 2 boundary layer with heat transfer: mass (a), axial momentum (b), radial momentum (c) and energy (d).

3.6 Validation of the Microwave Field Solver

Now that a certain degree of confidence has been established with regards to the fluid solver, another central part of the model, the microwave field solver is validated. A single test was performed to compare the predictions from the finite-element microwave code to those from the analytic formulation presented in Chapter 2, involving a cylindrical microwave waveguide filled with alumina ceramic. The cavity radius was chosen to be 7.62 cm, and the length was chosen as 5.26 cm. For this test case the microwave frequency was chosen as 2.45 GHz. The left end of the waveguide was shorted with a perfectly conducting plate. This configuration is similar to the supersonic stage of the thruster, but longer.

The normalized electric field components in the axial and radial directions follow directly from Eqn. 2.6, where as before the dielectric constant of alumina is taken to be 9.0. Fig. 3.15 is a contour plot of the time-averaged, axial field component, indicating that its maximum value is about 1.0. Points of maximum intensity are spaced roughly 2.08 cm apart. This distance is equal to $\lambda_g/2$. The time-averaged radial field component is shown in Fig. 3.16. The radial field is stronger than the axial field. The maximum value of the radial field is 2.78, which occurs 5.79 cm above the centerline.

A comparison is now made with the calculated results for these conditions, using the finite-element code which solves Eqn. 3.23 and Eqn. 3.24. A grid consisting of 140 axial finite elements and 120 radial finite elements was used to simulate the waveguide geometry. In this calculation, the procedure outlined previously, in the section on the boundary conditions for the finite-element code, was implemented. This procedure involves solving for the axial field component first, assuming a normalized value at the right end of the waveguide, subsequently determining the reflection coefficient, X in Eqn. 3.37 and Eqn. 3.37, from this solution, and using this value of reflection coefficient to specify the boundary conditions for the radial field. Unlike situations where a plasma exists inside the waveguide, the field amplitude, A^+ , was equal to unity in this test case. Only the phase of the microwave field at the inlet port needs to be determined here. The plots of the time-averaged axial and radial field components, found using the finite-element microwave solver, are shown in Fig. 3.17 and Fig. 3.18. There is hardly any difference at all between these contours and those of Fig. 3.15 and Fig. 3.16, respectively. The maximum axial field is 1.0 and the maximum radial field is 2.78, virtually identical with the results obtained from Eqn. 2.6. The separation between the points of maximum intensity for both the axial and radial fields in Fig. 3.17 and Fig. 3.18 is 2.08 cm, as expected. The only perceptible difference is that the radial field predicted by the finite-element code has its maximum at a distance of 5.88 cm above the centerline, whereas the analytic solution has a maximum at 5.79 cm above the centerline. This is only a 1.5% difference. The agreement shown here for this test case ver-

ifies that no egregious errors have been made in the numerical implementation of the finite-element method for microwave part of the physical model. Further results involving the complete simulation of various microwave thrusters will be presented in the following chapters, validating even further many aspects of the complex and comprehensive physical model developed in this thesis.

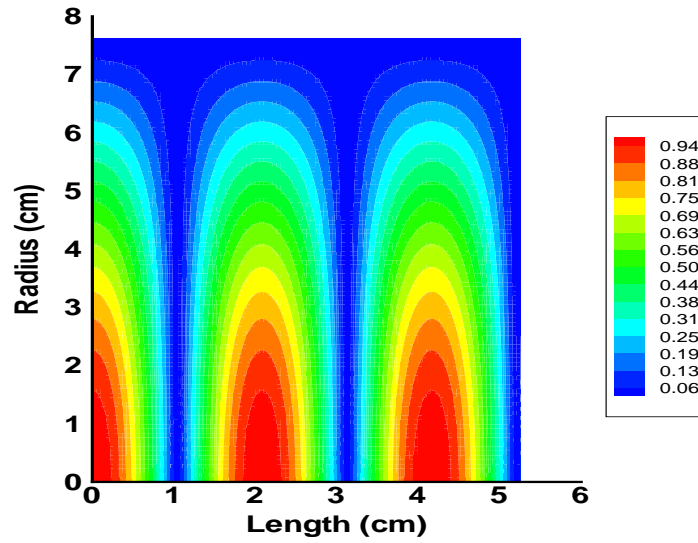


Figure 3.15: Analytic solution for the time-averaged, normalized, axial electric field in the waveguide.

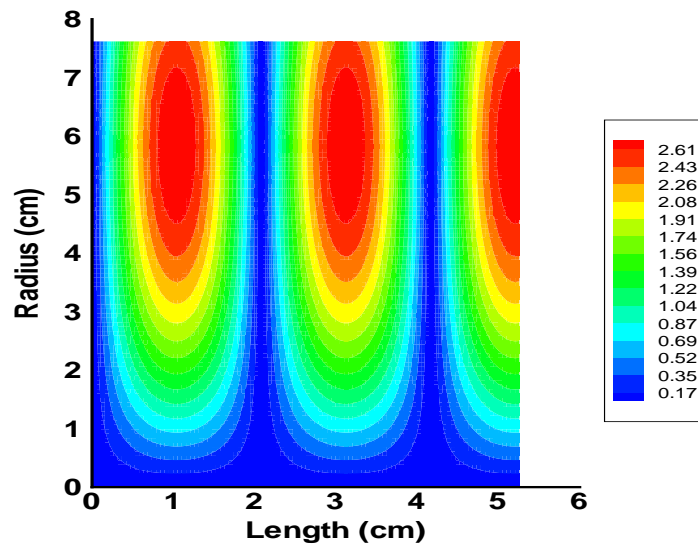


Figure 3.16: Analytic solution for the time-averaged, normalized, radial electric field in the waveguide.

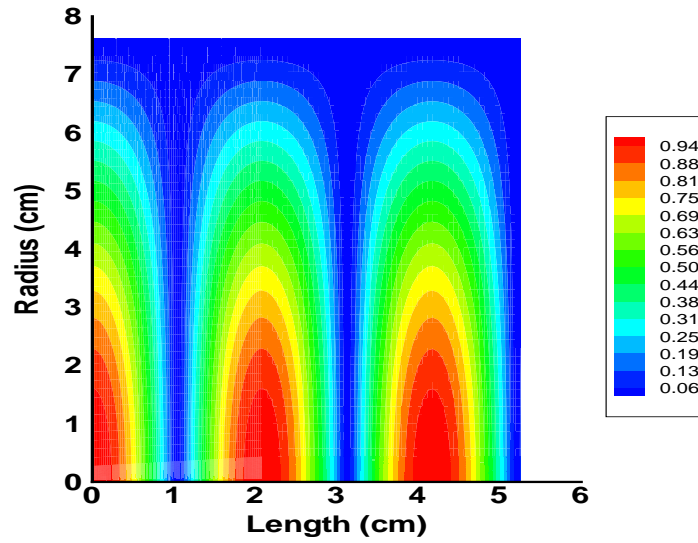


Figure 3.17: Finite-element solution for the time-averaged, normalized, axial electric field in the waveguide.

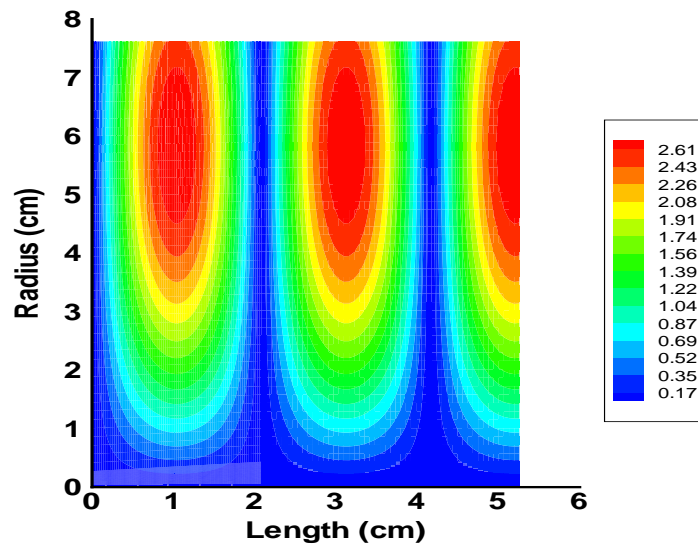


Figure 3.18: Finite-element solution for the time-averaged, normalized, radial electric field in the waveguide.

Chapter 4

Model Comparison with MET Thrust Data

The physical model, developed and validated, in the last chapter is now used to study the single-stage MET. Two calculations were performed, for two different MET thrusters, running on helium propellant. The predicted thrust is compared with existing thrust data in each case. The first case involves the standard 1 kW MET thruster, operating at 2.45 GHz, and the second case, a miniaturized, 100 W MET thruster, operating at 7.5 GHz. These two test cases were chosen in part because reliable thrust data exist in both instances, and also because, taken together, these two thrusters cover a broad range of operating conditions, in terms of power level, physical size and microwave frequency.

In this chapter the calculation involving the 1 kW MET is discussed first. A description of the structured grid used for the numerical simulation is given, along with a discussion of how the grid was generated and how many grid points were used for the calculation. The manner in which the boundary conditions are specified, which was discussed briefly in Chapter 3, is discussed in greater detail here; specifically, how the plenum wall temperature is determined, and how the subsonic inlet plane is treated. The calculation involving the 1 kW MET simulates a realistic thruster condition where the specific energy is 10 MJ/kg, with 100 mg/sec of mass flow rate and 1 kW of subsonic energy addition. Before any results are presented from this simulation, it is verified that the numerical solution is properly converged to steady state conditions. The results of the simulation include the gas temperature and electron temperature profiles inside the thruster. In addition the electron number density, another essential quantity in determining the conductivity and the defining property of the plasma, is presented. The electron joule-heating rate is then discussed, followed by the result for the electric field components. The number densities of the metastable excited atomic states are also presented. While there is a lack of flow field data for the MET, there exists a measurement of the spatial distribution of electron temperature inside the thruster,

and this will be used to compare with the calculation for the 1 kW MET. Finally a comparison is made with measured thrust data as well.

The second part of this chapter involves the 100 W MET. The numerical grid used for this geometry is presented, covering the essential features. Before presenting any results from the simulation, verification of convergence is done, as in the previous case. The 100 W MET thruster simulation was done for the same value of specific energy, 10 MJ/kg, as the 1 kW thruster. The results of this simulation include the gas temperature, electron temperature and all the other properties discussed above. The features which are similar to those of the 1 kW MET are highlighted. There are differences between this case and the 1 kW MET, however, involving where the regions of maximum ionization and joule heating are located, and the peak electron density. Thrust data were collected for this 7.5 GHz thruster by Sullivan [14], who measured the momentum in the exhaust plume, rather than determining the thrust directly using a conventional thrust stand. Although absorbed microwave powers in the range of 110 to 150 W were recorded by Sullivan [14] when making his measurements, the thruster which he used is referred to as the 100 W MET in this thesis. The measured thrust data for the 100 W MET are presented, showing how the specific impulse varies as a function of specific energy. A comparison is made between the computation and the measured thrust data for the 100 W thruster as well. Finally a summary of the model performance in simulating both single-stage thrusters is given.

4.1 Simulation of 1 kW MET

The standard microwave thruster, with a 10.16 cm diameter cylindrical cavity, discussed in the previous chapters, is the first test case for the model. Thrust data were collected for a thruster of this type, operating on helium, by Diamant *et al.* [9]. The nozzle throat diameter was 0.132 cm, and thrust measurements were made in the specific energy range between 5 and 20 MJ/kg. A calculation is performed for this thruster, operating at 10 MJ/kg. The calculation includes the effects of distinct electron and heavy particle temperatures and non-equilibrium ionization from several helium excited states, while assuming an Maxwellian electron energy distribution as outlined in Chapter 3. In this regard, the present model is much different than previous equilibrium models of microwave discharges, which were used to study microwave thrusters.

4.1.1 1 kW Thruster Grid

An essential ingredient for obtaining an accurate numerical solution is the proper choice of grids. Several methodologies exist for creating numerical grids, including the structured [37], the unstructured [34], and adaptive unstructured [36] ap-

proaches. A structured grid, with rectangular cells, was used for all the simulations in this work, because it is simpler to implement than an unstructured grid. An adaptive unstructured grid, which evolves as the flow changes, may offer certain advantages in terms of accuracy, however, especially if sharp gradients that fluctuate in time need to be resolved. The structured grid for the 1 kW MET consists of three regions: (a) the plenum section of the thruster, where microwave energy addition occurs, (b) the converging-diverging nozzle section, and (c) the vacuum expansion region, into which the flow exhausts from the nozzle.

In the 1 kW thruster there is a disparity between the length scales in the plenum and nozzle sections. The nozzle diameter is 0.132 cm, while the diameter of plenum section, which is a microwave resonant cavity, is 10.16 cm. To incorporate both of these length scales, without using an excessive number of points, a curvilinear series of grid points were chosen that follow the natural contours of the geometry. The grid points were formed by the intersection of the streamlines and lines of constant velocity potential, which would correspond to an incompressible flow moving through the physical domain of the thruster, from the plenum section, through the nozzle, and into the vacuum section. This is the standard approach for generating a structured grid [32,37]. The streamlines are found by solving Laplace's equation, $\nabla^2\phi = 0$, with the stream function ϕ equal to zero on the left boundary and equal to one on the right boundary. The normal derivative of ϕ is zero on the top and bottom boundaries of the domain. Similarly, the lines of constant velocity potential are found by solving the same equation, with a different set of boundary conditions. For this case ϕ is specified on the top and bottom boundaries and its normal derivative is set to zero on the left and right boundaries. A finite-element routine, similar to those used for finding the microwave field components, was used to solve Laplace's equation, for the two different sets of boundary conditions. The grid points were determined from the computed values of ϕ in each case.

The number of grid points in a numerical simulation influences its accuracy, and also determines the computational time required to complete the simulation. Choosing the number of points is therefore a compromise between accuracy and speed. For the 1 kW MET, a grid consisting of 61 radial cells and 190 axial cells was selected, as shown in Figure 4.1. This grid is such that at the throat there are 16 radial cells within 50 μm of the nozzle wall. A typical calculation, would take about twelve days to complete, using a personal computer, with an average processor speed of greater than 1 GHz, running the Linux operating system.

4.1.2 Boundary Conditions

There are two critical issues involving the modeling of the plenum boundaries which influence the calculation and were not discussed in Chapter 3. These are the treatment of the mass injection into the thruster and the treatment of the plenum

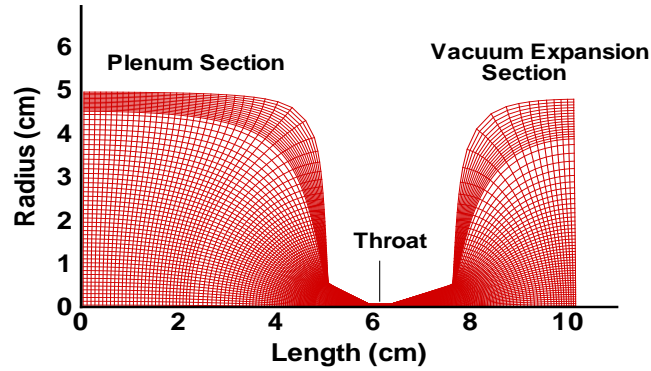


Figure 4.1: The structured grid generated for the 1 kW MET geometry.

wall temperature.

The standard MET has three injection ports in the plenum section, so that propellant can enter the thruster, as described in Chapter 2. These ports are oriented so that both axial and azimuthal components of flow velocity are induced. In the current model it is assumed that the mass injection occurs in an annular ring, 16 cells wide, in the upper left-hand corner of the plenum. The boundary conditions for this annular injection region are such that the temperature is fixed at 300 K, and the pressure is extrapolated from the neighboring cells. In addition the total mass flow rate entering the thruster is fixed, with the velocity and density at the inlet being adjusted based on the instantaneous pressure. The total mass flow rate into the thruster is 100 mg/sec. There is only one component of velocity at the inlet, the axial component. In the real thruster there is an azimuthal component as well, which is neglected in the simulation.

In order to properly account for the heat transfer to the walls of the thruster, a wall temperature was specified in the plenum section. In the current thruster model it is assumed that the temperature of the plenum wall remains constant, which is reasonable since the thermal conductivity of the metallic wall is high. The plenum wall extends from the top left hand corner of the grid to the nozzle throat, and is treated differently than the back plate, which forms most of the left hand boundary of grid (excluding the 16 cells used for mass injection). In the real thruster the back plate, or pressure plate, is made from boron nitride ceramic as

described in Chapter 2. The back plate is adiabatic in the current simulation. It is acceptable to neglect heat transfer through the back plate, as a first approximation, since the total surface area of the back plate is exactly three times less than the surface area of the metallic part of the plenum. It is also assumed that the nozzle wall in the diverging part of the nozzle is adiabatic because the cumulative convective heat flux along this surface should be considerably less than total heat flux in the plenum.

The plenum wall temperature was estimated for this simulation, using the values of mass flow rate and plenum pressure measured during operation of the thruster. In the simplest of terms the thruster can be considered a choked orifice, with a diameter equal to the throat diameter of nozzle. For a choked flow the stagnation temperature, T_0 , is related to the mass flow rate, \dot{m} , the area of the orifice, A , the stagnation pressure, P_0 , and the gas constant, R , according to the formula [55]

$$T_0 = \left(\frac{AP_0}{\dot{m}} \right)^2 \frac{\gamma}{R} \left(\frac{2}{\gamma + 1} \right)^{\frac{\gamma+1}{\gamma-1}}. \quad (4.1)$$

The measured value of plenum pressure was reported to be in the range of 700 to 1400 Torr by Diamant *et al.* [9]. T_0 determined from this formula was used as an estimate for the stagnation temperature in the plenum, which for the case of the 1 kW thruster, operating at a plenum pressure of 1100 Torr and with a mass flow rate of 100 mg/sec, was 1020 K. This temperature is greater than the melting point of aluminum, 933 K, and no doubt, the actual wall temperature is less than the stagnation temperature of the flow. Assuming a realistic wall recovery factor of 0.9 [57], for instance, the wall temperature becomes roughly 900 K. This value, 900 K, is taken as the wall temperature in the numerical simulation which follows. It should be pointed out also that Eqn. 4.1 is a one-dimensional approximation to the true two-dimensional flow field at the throat, and neglects the curvature of sonic line and the influence of the viscous boundary layer. As such it should be expected that the plenum temperature predicted by Eqn. 4.1, for a specified plenum pressure and mass flow rate, would not correspond exactly to the true plenum temperature. It is shown later in this chapter that using Eqn. 4.1 to predict the mass flow rate for the 100 W MET geometry, starting from a fixed temperature and pressure in the plenum, introduces at most at 10 % error in the mass flow rate value for the plenum conditions explored. Under certain conditions Eqn. 4.1 may not be accurate at all. For the present concerns, a 10 % error in any of the specified plenum conditions would not have a significant impact on the microwave field distribution or the plasma processes occurring inside the thruster, and for this reason the simple estimate for the wall temperature above, 900 K, was used.

4.1.3 Simulation Results

Before presenting contours of the various flow properties, resulting from the simulation, it is verified that mass and energy fluxes through the thruster nozzle are in fact close to the expected values and that these fluxes remain constant from one axial location to the next. In this simulation the inlet properties are such that 100 mg/sec of helium enters the thruster, with a total energy flux of approximately 170 W. Added to this energy flux is 1 kW of microwave energy, which is absorbed by the plasma in the plenum section. Assuming that the plenum wall is maintained at 900 K, as mentioned previously, the code predicts that the total heat flux through the plenum wall is approximately 720 W. This means that the total energy flux through the nozzle, under steady state conditions, should be about 450 W.

The energy and mass fluxes were calculated from the computed values of flow properties at the cell centers inside the nozzle. The contributions from all cells, with the same axial index i , were added to form the total flux through each vertical grid line inside the nozzle. There are seventy axial cells inside the nozzle. The energy and mass fluxes, so obtained for each index i , were normalized by their expected values, and are shown in Fig. 4.2. The energy flux differs typically by 7 % from the expected value, and remains relatively constant throughout diverging part of the nozzle (axial cells 30 to 70). The mass flux differs from the expected value of 100 mg/sec, typically by about 1 %. Like the energy flux the mass flux remains relatively constant throughout the nozzle. The fact that these numbers did not change significantly after one million time steps, strongly suggests that for practical purposes steady state conditions have been reached. The sensitivity of the mass flux prediction to the level of numerical dissipation, and the amount of grid refinement is explored further in the last section of this chapter. It is unlikely that the difference between the expected and predicted values of the mass and energy fluxes would have a strong influence on the plasma properties inside the thruster.

An important assumption in formulating the physical model in Chapter 3, was that turbulence does not play a significant role in the transport processes. Now this assumption can be verified using the results of this calculation. The Reynolds number, $Re_x = \rho u x / \mu_h$, was computed for each axial cell on the centerline in the nozzle. The distance from the nozzle entrance was used as the length scale. The maximum value of Re_x is 4×10^4 , which occurs in the vicinity of the throat (axial cell 30) as shown in Fig. 4.3. The turbulent transition for an incompressible boundary layer over a flat plate occurs at about $Re_x = 2 \times 10^6$, when the initial turbulence level in the free stream is vanishingly small [57]. With an initial turbulence of a few percent in the free stream, the transition threshold is reduced to as low as approximately 3×10^5 , roughly [57]. Since the Reynolds number in this case is less than 10^5 , the boundary layer inside the nozzle of the microwave thruster is most likely laminar, and the model developed in this thesis should be able to describe it accurately. Outside the nozzle, in the free jet expansion region, there is a shear

layer where turbulence is significant.

The results for the physical properties of interest inside the 1 kW MET are now presented. Fig. 4.4 shows the gas temperature contours in degrees Kelvin. The gas temperature is relatively constant in the plenum, about 920 K, which is 20 K higher than the specified wall temperature. The electron temperature, shown in Fig. 4.4, on the other hand has a maximum on the centerline, which occurs about 3 cm downstream of the back plate, where the electron temperature is approximately 14800 K. The electron temperature contours, are shown in Fig. 4.5. It is readily apparent that the electron temperature profile is markedly different than the gas temperature profile, by an order of magnitude. The regions of maximum electron temperature correspond to the locations of maximum electric field strength. The electron temperature is relatively constant in the region of maximum field strength, varying by one to two hundred degrees. The disparity between the electron and heavy species temperature occurs, even though the gas pressure is 1400 Torr, as can be seen by comparing Fig. 4.4 and Fig. 4.5. The pressure contours are shown in Fig. 4.6. The calculated value of pressure is towards the upper end of the range of plenum pressure observed in the experiments, 700 to 1400 Torr, as reported by Diamant *et al.* [9], and differs by about 30 % from the value used above with Eqn. 4.1 to make a rough estimate of the wall temperature.

The contours of the axial component of the electric field are shown in Fig. 4.7. The maximum value of the axial electric field is about 0.65 kV/cm, which occurs on the centerline, about 3 cm downstream of the back plate. The back plate is located at the origin in Fig. 4.7, and the plenum section, where the flow properties are calculated is entirely to the right of the back plate. The radial component of the complex electric field is shown in Fig. 4.8. The electric field pattern is similar to the ideal mode structure presented in Chapter 2, as the electron number density is not high enough to seriously perturb the electric field. Most of the joule heating of the electrons occurs in the region of maximum axial field. The joule heating rate is shown in Fig. 4.9. The electrons receive roughly 5.5 W/cm^3 of power from the microwave field on the centerline. The heated region is fairly large, and not as compact as the result from the equilibrium model would indicate [15]. The heating rate decreases by about 30 % as one moves three centimeters away from the centerline in the radial direction.

For microwaves at 2.45 GHz the critical electron number density is $7.5 \times 10^{10} \text{ cm}^{-3}$. The electron number density, computed for the 1 kW MET is larger than this, as shown in Fig. 4.10. The maximum electron number density is $8.4 \times 10^{10} \text{ cm}^{-3}$, which occurs along the centerline of the plenum section. A surprising result from this calculation is that the electron number density is fairly uniform throughout the plenum section. The net ionization rate is shown in Fig. 4.11. Electrons are created in the region of maximum joule heating, at a rate of about $4.1 \times 10^{13} \text{ cm}^{-3} \text{ sec}^{-1}$ and the recombination rate is not strong enough in the other areas of the plenum to

localize the electron concentration. Dissociative recombination involving He_2^+ is considered in the current model, yet this doesn't seem to be sufficient for plasma localization. As discussed in Chapter 3 this process would be the dominant electron loss process for a static discharge under the conditions of interest here. In this calculation one needs to remember that the number density of He_2^+ is set equal to the number density of electrons since by the thermodynamic arguments presented in Chapter 3 molecular ions are the dominant ionic species and there is no net charge in the flow.

The 2^1S and 2^3S helium metastable states are relatively localized in the plenum and on the centerline, as shown in Fig. 4.12 and Fig. 4.13, respectively. The number densities of these species on the centerline are 4.2×10^{10} and $4.6 \times 10^{10} \text{cm}^{-3}$, in that order. Both 2^1S and 2^3S are maintained in significant numbers throughout the plenum, but the value of each of these species decreases by roughly a factor of two as one moves away from the centerline, in contrast to the electron number density which remains relatively constant. The spatial distribution of the metastable species, as calculated here, suggests that the plasma luminosity would be greatest on the centerline, provided that optical transitions involving the ionic species are not significant, and the discharge would appear as a ball in front of the converging nozzle section. This situation corresponds to what is commonly observed for helium METs under similar conditions of flow rate and absorbed microwave power [9]. Taking the electron temperature value just mentioned on the centerline, 14800 K, and the ground state number density, which is $1.5 \times 10^{19} \text{cm}^{-3}$, the number densities that the metastable species would have if a Boltzmann equilibrium was maintained among the different excited states can be computed. These values turn out to be $1.4 \times 10^{12} \text{cm}^{-3}$ for 2^1S and $8.1 \times 10^{12} \text{cm}^{-3}$ for 2^3S . The metastable number density differs from the Boltzmann equilibrium value by more than an order of magnitude in both cases. The effects of photo-recombination and Penning ionization were not included in the present model and these processes may have some influence on the number density of the metastable species. This is a topic for future work. The current result, by itself, neglecting these processes or the non-Maxwellian nature of the electron energy distribution is an example of why it is necessary to include several excited species and finite rate kinetics for ionization and excitation in physical model, in order to accurately model the number densities of the excited states.

The Mach number contours inside thruster are shown in Fig. 4.14. The Mach number on the centerline at the nozzle exit is about 6.6. The flow is under-expanded at the nozzle exit, since the exit pressure is about 1.2 Torr and the background pressure in the vacuum expansion region is roughly 0.7 Torr. An expansion fan can be seen, as the subtle shift in color from green to dark blue, at the nozzle exit in Fig. 4.6. The axial velocity contours for the 1 kW MET are shown in Fig. 4.15. The axial velocity at the exit is about 3 km/sec. There is a prominent re-circulation

region inside the plenum chamber, as indicated by the streamlines in Fig. 4.15.

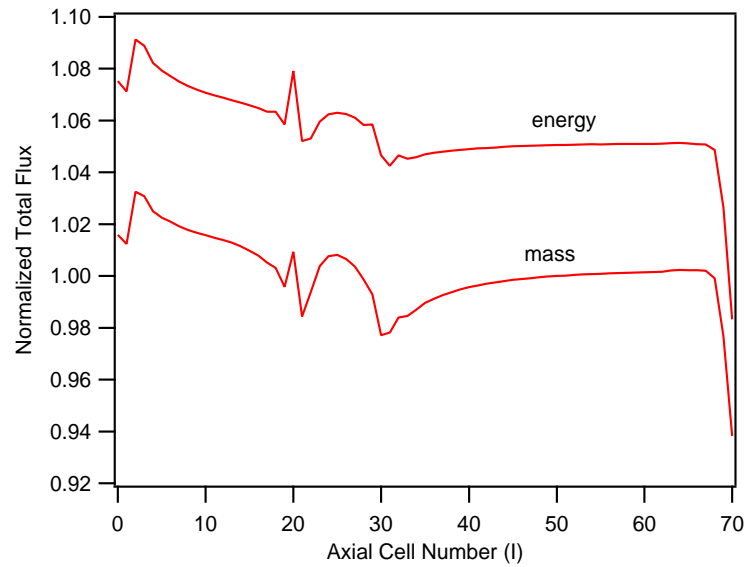


Figure 4.2: Normalized total mass and energy fluxes inside the nozzle of the 1 kW MET.

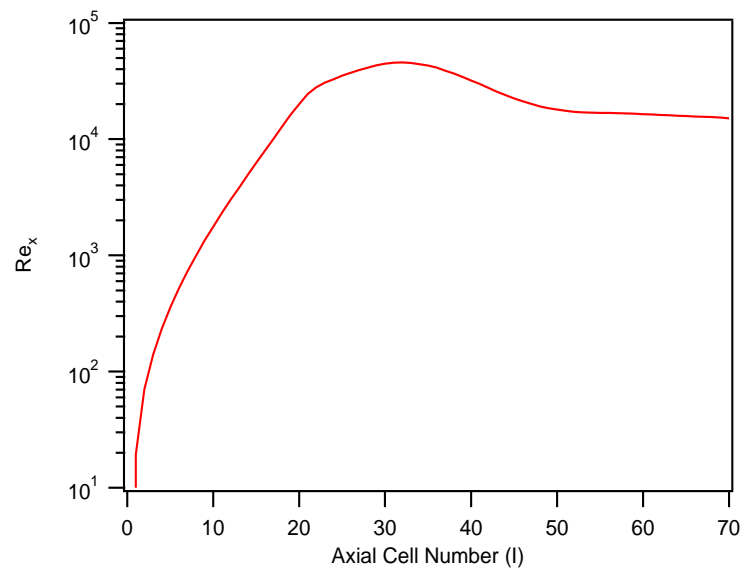


Figure 4.3: Reynolds number (Re_x) on the centerline inside the nozzle of the 1 kW MET.

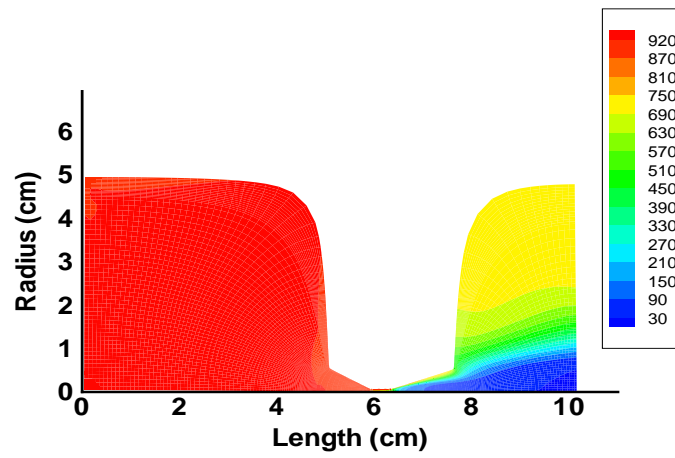


Figure 4.4: Gas temperature contours inside the 1 kW MET (in K).

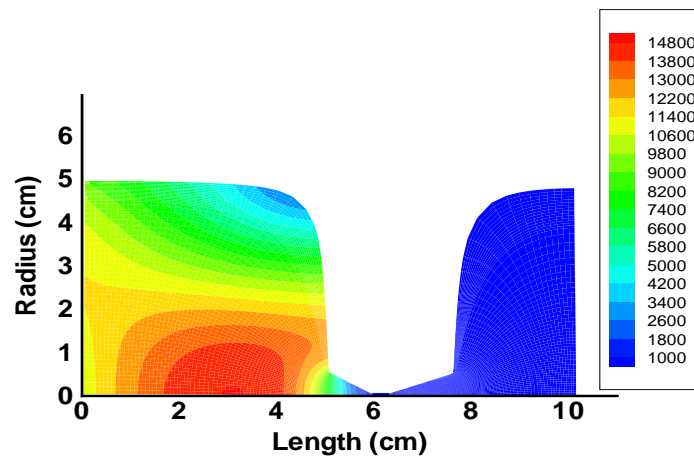


Figure 4.5: Electron temperature contours inside the 1 kW MET (in K).

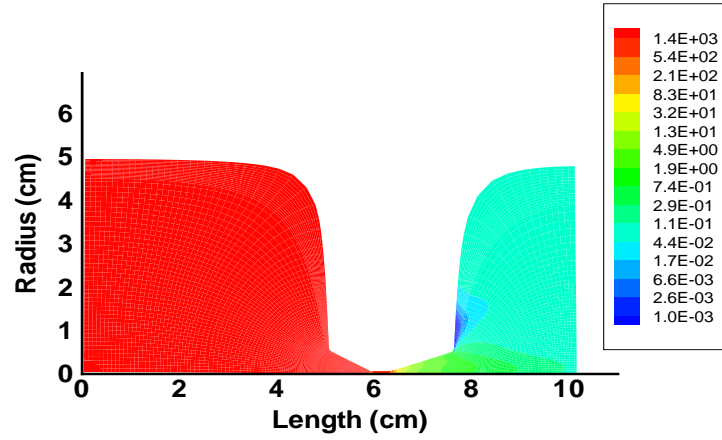


Figure 4.6: Pressure contours inside the 1 kW MET (in Torr).

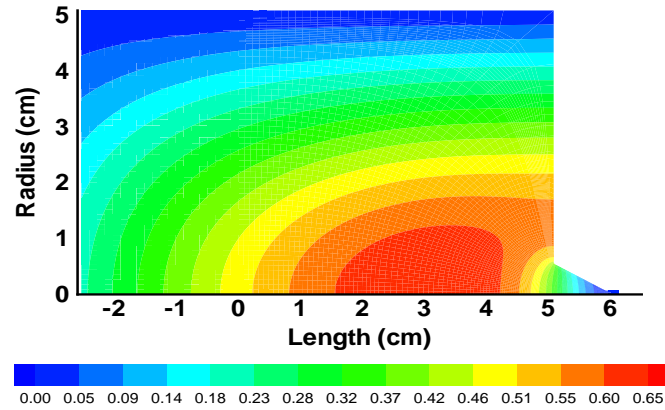


Figure 4.7: Time-averaged value of the axial component of the complex electric field inside the 1 kW MET (in kV/cm). The back plate is located at $x=0$.

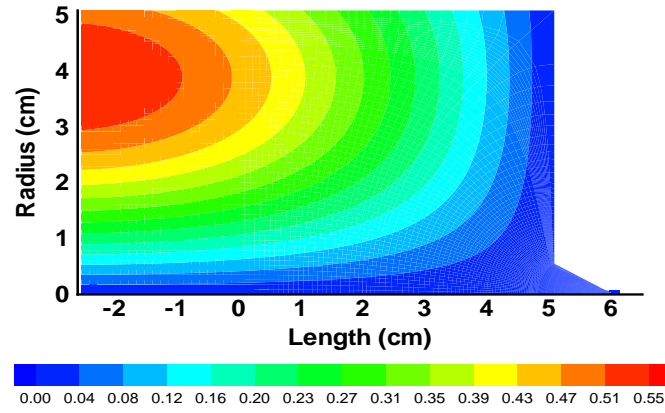


Figure 4.8: Time-averaged value of the radial component of the complex electric field inside the 1 kW MET (in kV/cm). The back plate is located at $x=0$.

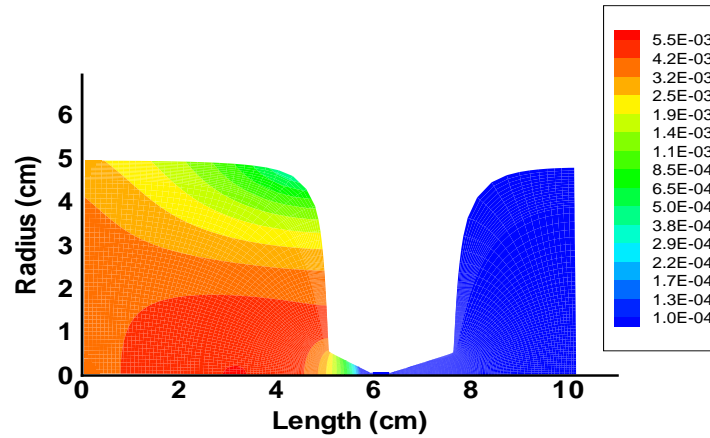


Figure 4.9: Joule heating rate of electrons inside the 1 kW MET (in kW/cm^3).

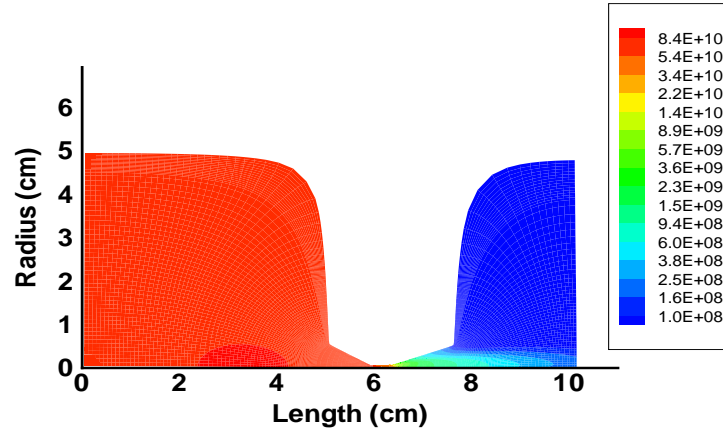


Figure 4.10: Electron number density contours inside the 1 kW MET (in cm^{-3}).

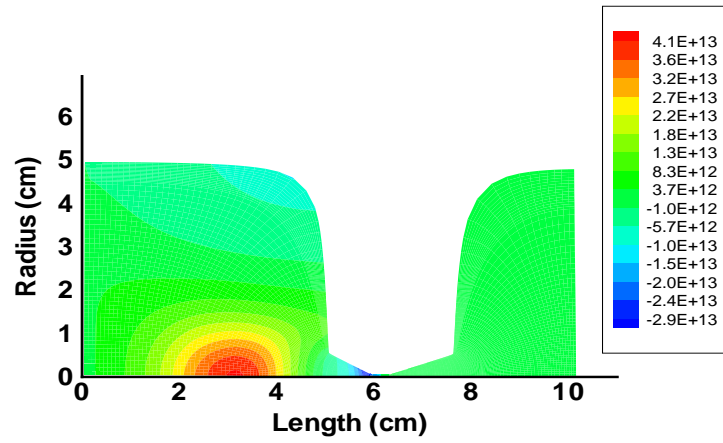


Figure 4.11: Net ionization rate inside the 1 kW MET (in $\text{cm}^{-3} \text{sec}^{-1}$).

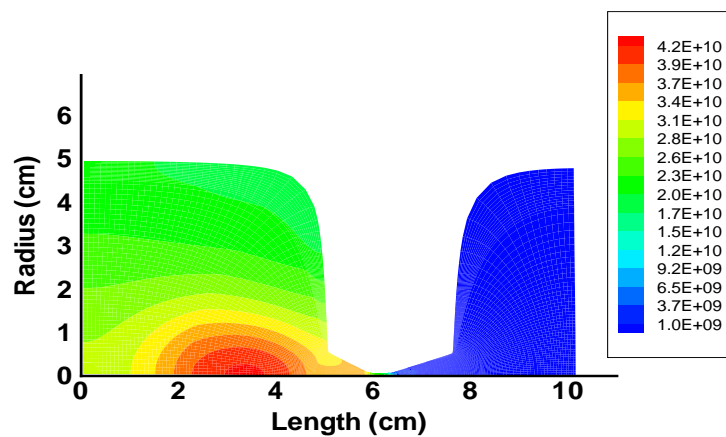


Figure 4.12: 2^1S (He I) number density contours inside the 1 kW MET (in cm^{-3}).

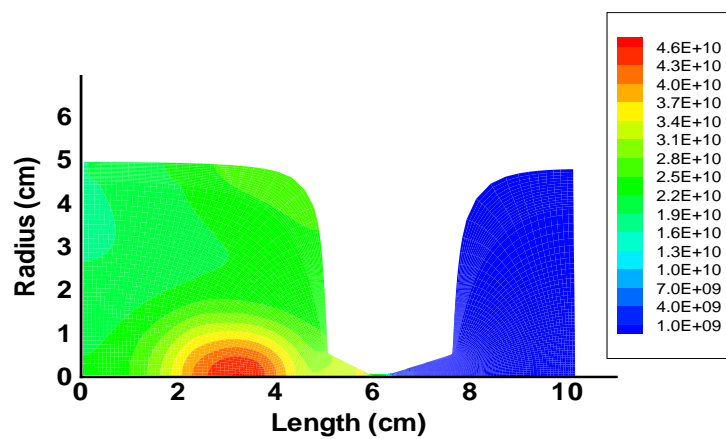


Figure 4.13: 2^3S (He I) number density contours inside the 1 kW MET (in cm^{-3}).

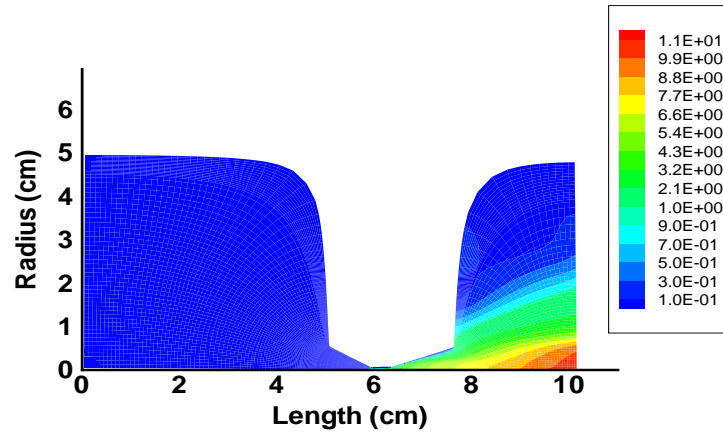


Figure 4.14: Mach number contours inside the 1 kW MET.

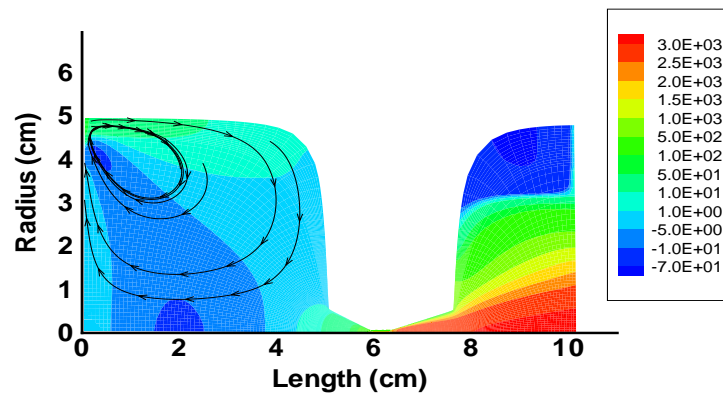


Figure 4.15: Axial velocity contours inside the 1 kW MET (in m/sec).

4.1.4 Comparison with Equilibrium Model

A comparison can be made with the corresponding results, using a single-temperature equilibrium model. A few years ago a fully coupled calculation, solving both the Navier-Stokes equations and Maxwell's equations, was performed for microwave-sustained helium discharges in a geometry similar to the 1 kW MET [15]. In this model the electron number density was determined from the Saha equation, and the electron and heavy particle temperatures were equal. There are several points where this equilibrium model and the present model differ.

In the equilibrium model the peak electron temperature on the centerline of the discharge was found to be about 13,000 K and the electron number density, $9 \times 10^{11} \text{cm}^{-3}$. Those values agree well with what was found here, where the temperatures of the electrons and heavy particles differ, and 12 different electron impact ionization and excitation processes are considered. An important difference, however, is that the gas temperature here is not nearly as high as the electron temperature and is relatively constant throughout the discharge region. The current result for the peak electron temperature, on the centerline about 3 cm in front of the back plate, is within about 25 % of the electron temperature measured by Balaam [12] using continuum emission spectroscopy in microwave helium discharges under similar conditions. The data collected by Balaam is shown in Fig. 4.16 together with the calculated electron temperature profile for the 1 kW MET, 3 cm in front of the back plate, which was just presented. According to the experimental data there is little radial variation in electron temperature as one moves a centimeter away from the centerline, and this trend is indeed borne out by the numerical simulation done here, much more so than in the result from the equilibrium model.

In addition, the present result predicts an electron number density that is relatively uniform throughout the entire plenum region. This is in strong contrast with the result from the equilibrium model, where the plasma is well localized on the centerline. The difference is most likely due to the fact that in the current model, finite-rate kinetics are included for ionization, and in the equilibrium model it is assumed that electron number density has an equilibrium value, controlled by the local value of gas temperature, everywhere. Since in the equilibrium model, there is a strong temperature gradient associated with the plasma, the electron number density is significant only in the region of peak temperature, on the centerline. It is interesting to note that while the current model does not predict that there is any significant gradient in electron number density, it does predict, however, that the concentrations of excited species are well localized on the centerline. This is corroborated by observations of the visible light emission, which is compact and on the centerline, during the operation of the 1 kW MET [9, 12]. The simulation done here, therefore, suggests that electrons are present outside the visible region of plasma emission. Doubtless, measurements of the radial distribution of the electron number density are required to investigate this point and confirm experimen-

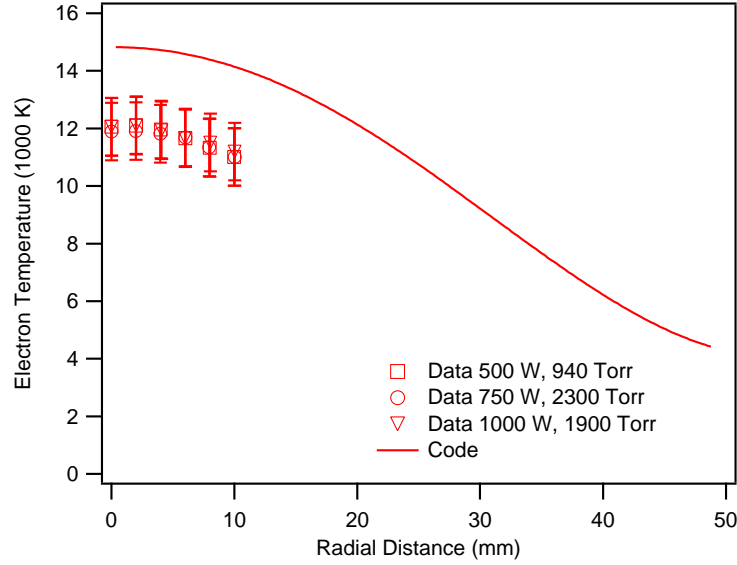


Figure 4.16: Electron temperature in a microwave helium discharge as a function of radial position as measured by Balaam [12]. The solid line indicates the computational result for the 1 kW MET from this chapter.

tally this interesting result.

One thing is certain, the importance of including separate electron and heavy particle temperatures, even at relatively high pressure of more than one atmosphere in the plenum, has been illustrated. Any model that describes this kind of microwave heating problem must include a separate electron energy equation.

4.1.5 Comparison with Thrust Data

For the case just considered, with 1 kW energy addition in the plenum, the calculated thrust of the MET is 0.29 N. Using the specified value of mass flow rate at the inlet, 100 mg/sec, the specific impulse is about 300 sec. It is instructive to compare the predicted specific impulse from the full calculation with a simple estimate using the computed stagnation temperature in the plenum, about 920 K. The specific impulse can be related to the stagnation temperature in the plenum of the thruster according to

$$I_{sp} = \frac{\sqrt{2c_p T_0}}{g_0}, \quad (4.2)$$

which follows by simply setting the kinetic energy leaving the thruster equal to the stagnation enthalpy in the plenum. When Eqn. 4.2 is used together with $T_0 = 920$ K

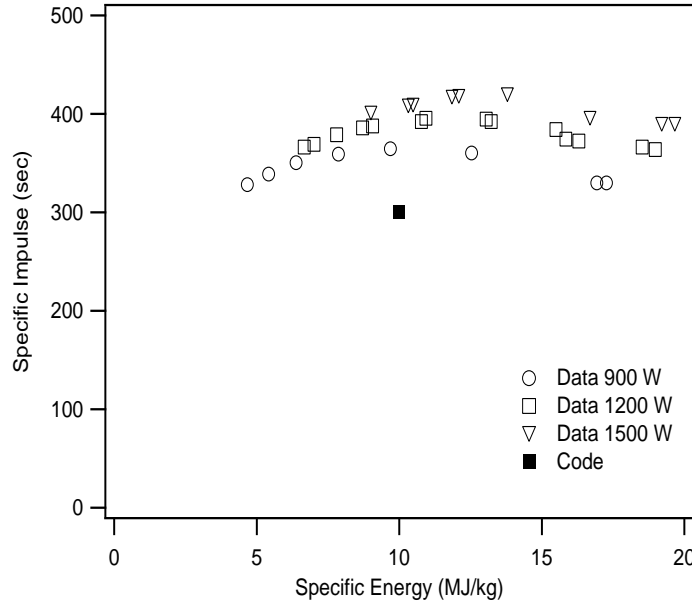


Figure 4.17: Measured values of specific impulse as a function of specific energy for the 1 kW MET, taken by Diamant *et al.* [9]. The error bars for these measurements are not shown and were reported as 5 %.

the result is 315 sec, which differs by 5 % from the corresponding result from the full fluid calculation including the viscous boundary layer in the nozzle. The results of the full simulation also show that of the power absorbed in the plenum, 72 % is transferred to the wall in the subsonic plenum section due to thermal conduction of the heavy particles.

Thrust data were taken for this thruster by Diamant *et al.* [9], using a conventional thrust stand. The results are shown in terms of specific impulse in Fig. 4.17, and the calculated thrust value at 10 MJ/kg from this thesis is shown also for comparison. For a specific energy of 10 MJ/kg, the specific impulse should be about 360 ± 20 sec, according to the experimental thrust data taken at 900 W input power, as shown in Fig. 4.17. The result from this calculation for specific impulse, 300 sec, is about 20 % lower than the measured value at 900 W input power.

The measured value of specific impulse, 360 ± 20 sec, can be used to make a simple estimate of the stagnation temperature in the plenum of the 1 kW thruster by using Eqn. 4.2, and the result is a plenum stagnation temperature of 1200 K. The fact that this is about 30 % higher than the melting point of aluminum implies that there is a temperature gradient in the plenum, with the temperature dropping down to a tolerable level near the wall. Large temperature gradients in the plenum are not present in the results of the current model, however.

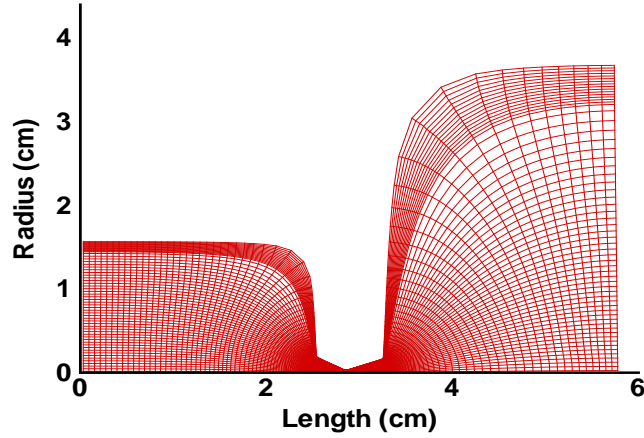


Figure 4.18: The structured grid generated for the 100 W MET.

4.2 100 W MET Simulation

The second case explored in this chapter, involves the simulation of a miniaturized MET, with a 3.2 cm diameter cylindrical cavity, operating at 7.5 GHz. This thruster was built as part of a DARPA Phase I SBIR project, to build and test a water-fueled MET, meant to operate at power levels of 100 to 150 W, involving Princeton University and Research Support Instruments (RSI), a private company [14]. This miniature MET thruster is referred to as the 100 W MET in this thesis. Helium thrust data were collected by Sullivan as part of this project for a range of specific energies between 5 and 20 MJ/kg [14] in the same vacuum facility used for operating the two-stage thruster and making the LIF measurements, which is described in Chapter 5. The nozzle throat diameter, for the 100 W thruster, is 0.37 mm, and it was designed for flow rates in the range from 1 to 50 mg/sec. The geometry of the thruster is such that it supports only a TM_{011} type mode, at 7.5 GHz.

A calculation was performed for this thruster, operating with helium at 10 MJ/kg, using the same code written to simulate the 1 kW thruster. The structured grid used for the 100 W MET simulation, consisting of 61 radial cells and 165 axial cells, is shown in Figure 4.18. This grid was generated in the same fashion as the previous grid, and is such that there are 16 radial cells within $30\ \mu\text{m}$ of the nozzle wall in the throat region. The three plenum injection ports on this thruster were modeled as an annular ring, consisting of 16 radial cells, in the same manner as for the 1 kW

MET. In this case a mass flow rate of only 10 mg/sec is considered, rather than 100 mg/sec for the 1 kW MET.

At a specific energy of 9.6 MJ/kg Sullivan [14] measured a specific impulse of roughly 290 sec, and this value can be related to the stagnation temperature in the plenum of the thruster using Eqn. 4.2. When this is done the stagnation temperature in the plenum is calculated to be about 780 K. For the calculation of the 100 MET in this thesis the wall temperature was taken to be smaller than the stagnation temperature, about 725 K instead of 780 K, and this situation would correspond to a wall recovery factor of 0.93. With a mass flow rate of 12 mg/sec and a plenum pressure of 670 Torr, as measured by Sullivan [14] at 9.6 MJ/kg, Eqn. 4.1 would give a stagnation temperature of 160 K which is less than room temperature, and therefore the validity of Eqn. 4.1 in this case is in question.

4.2.1 Simulation Results

For this simulation 10 mg/sec of helium is introduced into the thruster, at 300 K, representing a total energy flux of roughly 17 W. The calculation predicts that 80 W, of the 100 W absorbed by the plasma in the plenum is transferred through the plenum wall due to thermal conduction. Therefore, in the nozzle, the energy flux should be about 37 W, which is the difference between the absorbed microwave power, 100 W, and the power lost by thermal conduction through the nozzle wall, 80 W, plus the total enthalpy flux entering the thruster, 17 W. The mass and energy fluxes through the nozzle, calculated from the results of the numerical simulation, are shown in Fig. 4.19. As before these fluxes have been normalized by their expected values. The mass flux in the nozzle is on average 12 % lower than the expected value of 10 mg/sec, and the energy flux is on average 8 % lower than the expected value of 37 W, throughout most of the nozzle. In both cases the agreement is worse than with the 1 kW simulation. The effect of numerical dissipation and grid refinement on the ability of the fluid code to accurately predict mass flux is explored at the end of this chapter. The Reynolds number on the centerline is shown in Fig. 4.20, and its peak value of about 5000 near the throat is an order of magnitude lower than the previous case. With this low Reynolds number the boundary layer in the nozzle of the 100 W MET is most likely laminar.

The complete results of a simulation involving the 100 MET are now presented, starting with temperature contours. Fig. 4.21 shows the gas temperature contours in degrees Kelvin. The gas temperature is constant throughout most of the plenum at about 740 K, and decreases somewhat to 730 K near the wall. There are no large temperature gradients in the plenum. The electron temperature contours are shown in Fig. 4.22, and unlike the 1 kW simulation the peak electron temperature occurs near the origin. The electron temperature is approximately 17700 K at the origin, and remains relatively high (greater than 10000 K) within a narrow radius

as one moves along the centerline until the entrance to the converging part of the nozzle is reached. For the 100 W MET, the pressure is roughly 360 Torr in the plenum, with little variation, as shown in Fig. 4.23. The measured pressure during the experiments performed by Sullivan [14] with this thruster was 670 Torr, for the case of a 12 mg/sec mass flow rate and an absorbed microwave power of 116 W (specific energy of 9.6 MJ/kg). For the current case of the 100 W MET the code predicts a plenum pressure that is roughly half of that value, 360 Torr, with 10 mg/sec of mass flow and 100 W of absorbed microwave power.

The electric field pattern in the 100 W MET differs from what the ideal pattern in an empty cavity would be, using the equations from Chapter 2. The contours of the axial component of the electric field are shown in Fig. 4.24. As before, the back plate is located at the origin, and the plenum section is to the right of the origin, in front of the back plate. The maximum value of the axial electric field inside the thruster ($x > 0$) is about 0.24 kV/cm, which occurs close to the back plate (at $x = 0$). The axial field is fairly constant throughout most of the plenum chamber, dropping to zero of course near the wall. The corresponding radial component of the complex electric field is shown in Fig. 4.25. The joule heating rate is shown in Fig. 4.26. The electrons receive roughly 0.014 kW/cm³ of power from the microwave field near the origin. Just as with the electron temperature the heating rate is maintained at fairly high value within a narrow radius from the origin, where its peak value is located, to the entrance of the converging nozzle, and the region of high joule heating can be described as an arrowhead, with the sharp point of the arrow directed into the converging part of the nozzle. Practically all of the energy gained by the electrons from the microwave field in this region is transferred to the heavy particles, due to elastic collisions, as described by Eqn. 3.6.

For microwaves at 7.5 GHz the critical electron number density is $7 \times 10^{11} \text{cm}^{-3}$. The electron number density computed for the 100 W MET is shown in Fig. 4.27. As was the case with the 1 kW MET, the electron number density is fairly uniform throughout the plenum section where it is $5.7 \times 10^{11} \text{cm}^{-3}$, slightly less than the critical value. The net ionization rate is shown in Fig. 4.28, and the region of significant electron production has the now familiar shape of an arrowhead. Electrons are created at the origin, at a rate of about $2.5 \times 10^{16} \text{cm}^{-3} \text{sec}^{-1}$, and as with the 1 kW MET the dissociative recombination rate is not strong enough in the other areas of the plenum to localize the electron concentration.

The 2^1S helium metastable state is concentrated in the region of maximum joule heating, at the origin, as shown in Fig. 4.29. Near the origin its maximum value of $2.1 \times 10^{11} \text{cm}^{-3}$ occurs, and unlike the electron number density there is significant variation in the number density of the 2^1S metastable state, with its value decreasing by an order of magnitude as one moves into the top right-hand corner of the plenum. The number density of the 2^3S metastable state is shown in Fig. 4.30, and both its magnitude and spatial distribution are similar to the case of

the 2^1S state. The number density of 2^3S near the origin is actually the same as that of the 2^1S state, $2.1 \times 10^{11}\text{cm}^{-3}$. If a Boltzmann equilibrium was maintained among the metastable states at an electron temperature of 17700 K and a helium ground-state density of $4.7 \times 10^{18}\text{cm}^{-3}$, then the concentrations of the metastable states would be $6.4 \times 10^{12}\text{cm}^{-3}$ for 2^1S and $3.2 \times 10^{13}\text{cm}^{-3}$ for 2^3S . In both cases, therefore, the metastable number density differs from the Boltzmann equilibrium value by more than an order of magnitude. The concentration of metastable states is significant in a spatial region which is shaped like an arrowhead, as evident in both Fig. 4.29 and Fig. 4.30, and in a real thruster there would be strong light emission associated with this region due to the high metastable number density there. This arrowhead region, with its long, sharp point on the centerline extending towards the converging nozzle, is suggestive of the filament phenomenon observed in the subsonic stage of the two-stage thruster running on argon as described in Chapter 6.

The Mach number contours inside the thruster are shown in Fig. 4.31. The Mach number on the centerline at the nozzle exit is about 4.0. The axial velocity contours for the 100 W MET are shown in Fig. 4.32. The axial velocity on the centerline at the exit is about 2.5 km/sec. There is a prominent re-circulation zone inside the plenum of the 100 W MET as was the case with the 1 kW MET.

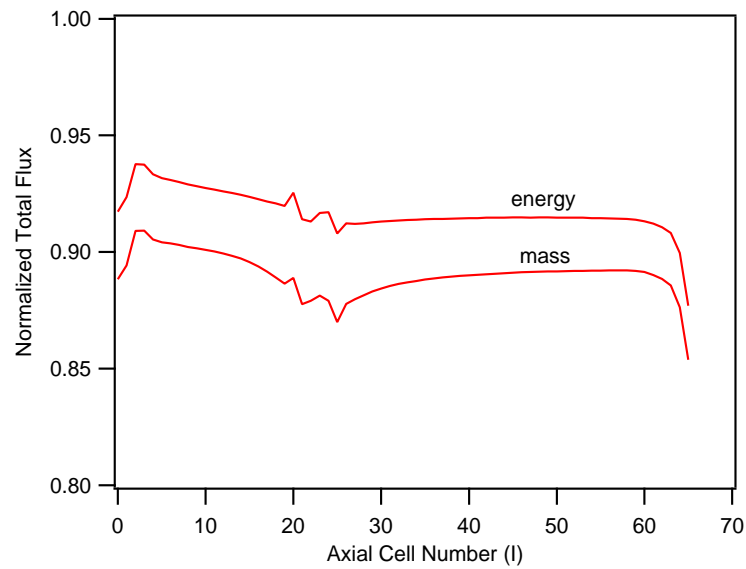


Figure 4.19: Normalized total mass and energy fluxes inside the nozzle of the 100 W MET.

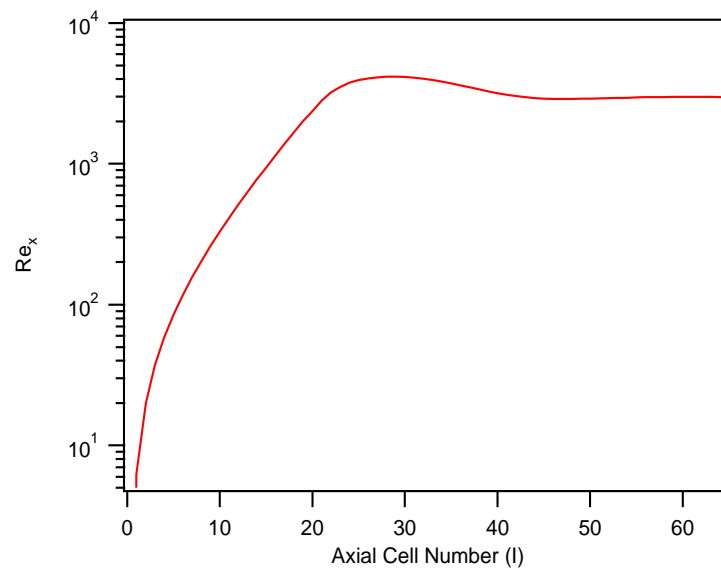


Figure 4.20: Reynolds number (Re_x) on the centerline inside the nozzle of the 100 W MET.

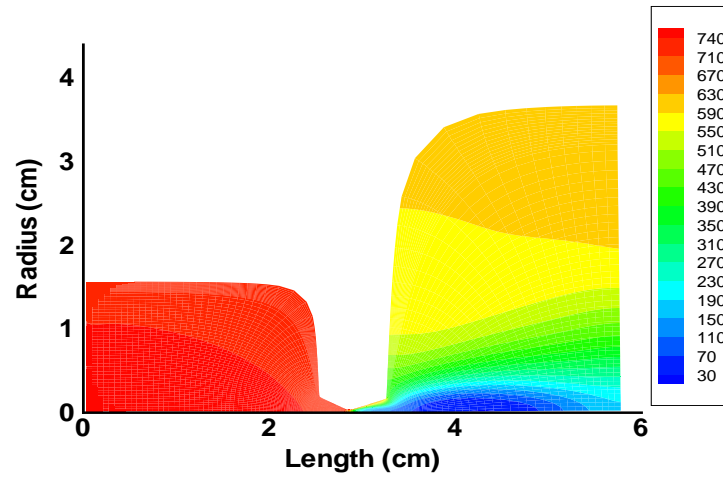


Figure 4.21: Gas temperature contours inside the 100 W MET (in K).

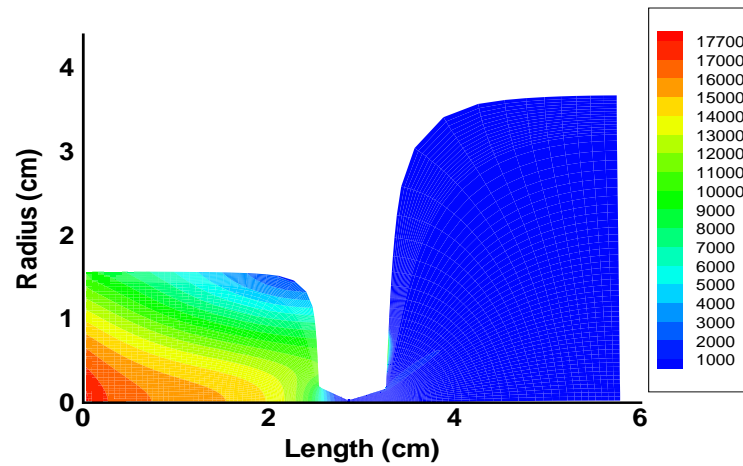


Figure 4.22: Electron temperature contours inside the 100 W MET (in K).

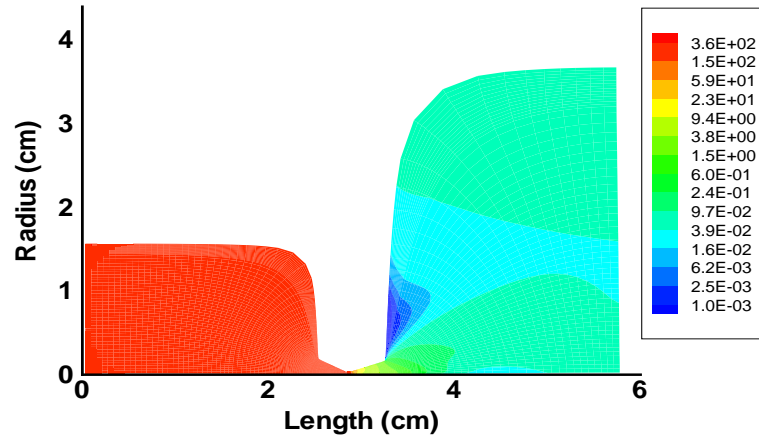


Figure 4.23: Pressure contours inside the 100 W MET (in K).

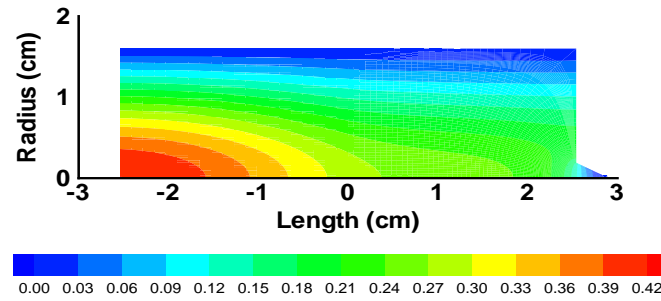


Figure 4.24: Time-averaged value of the axial component of the complex electric field inside the 100 W MET (in kV/cm). The back plate is located at $x=0$.

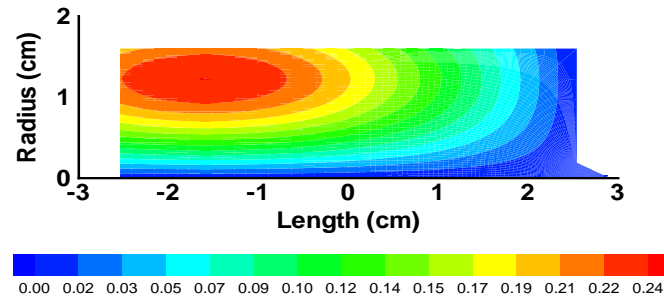


Figure 4.25: Time-averaged value of the radial component of the complex electric field inside the 100 W MET (in kV/cm). The back plate is located at $x=0$.

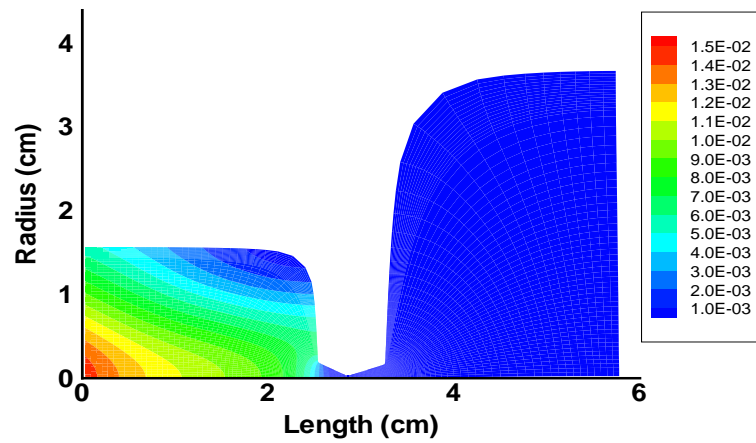


Figure 4.26: Joule heating rate of electrons inside the 100 W MET (in kW/cm^3).

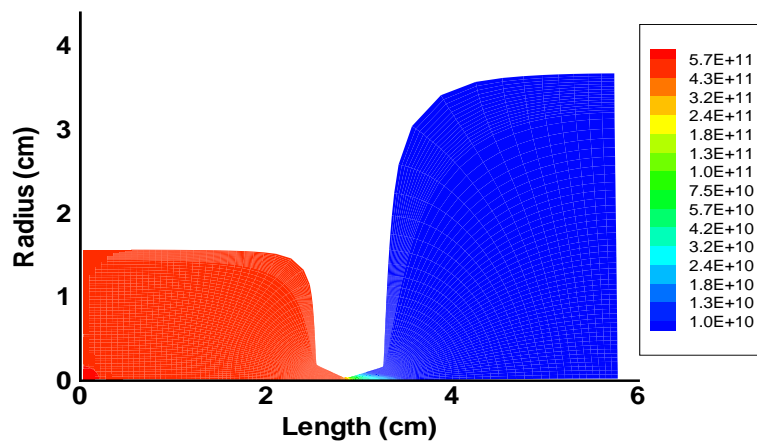


Figure 4.27: Electron number density contours inside the 100 W MET (in cm^{-3}).

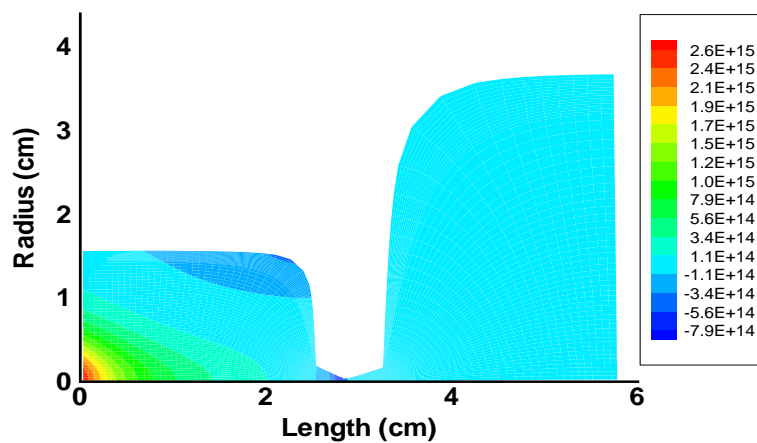


Figure 4.28: Ionization rate contours inside the 100 W MET (in $\text{cm}^{-3} \text{ sec}^{-1}$).

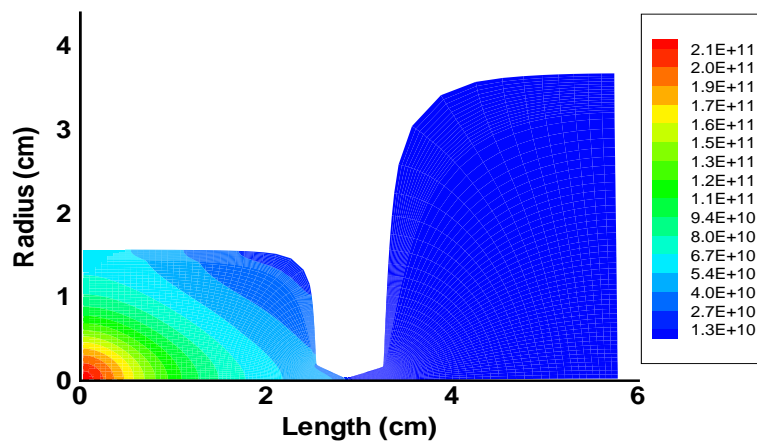


Figure 4.29: 2^1S (He I) number density contours inside the 100 W MET (in cm^{-3}).

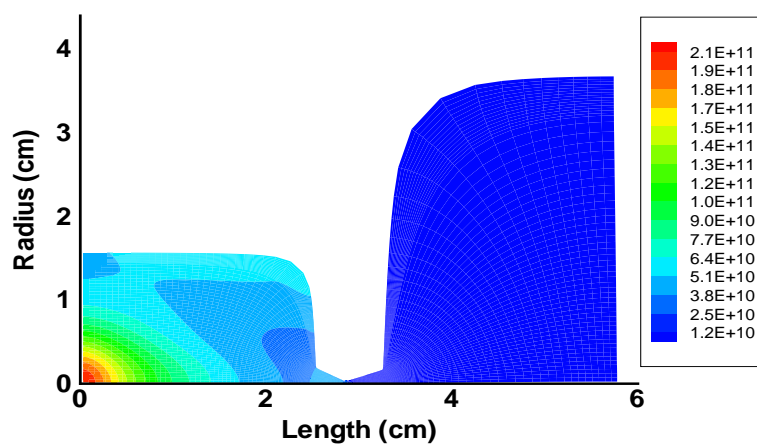


Figure 4.30: 2^3S (He I) number density contours inside the 100 W MET (in cm^{-3}).

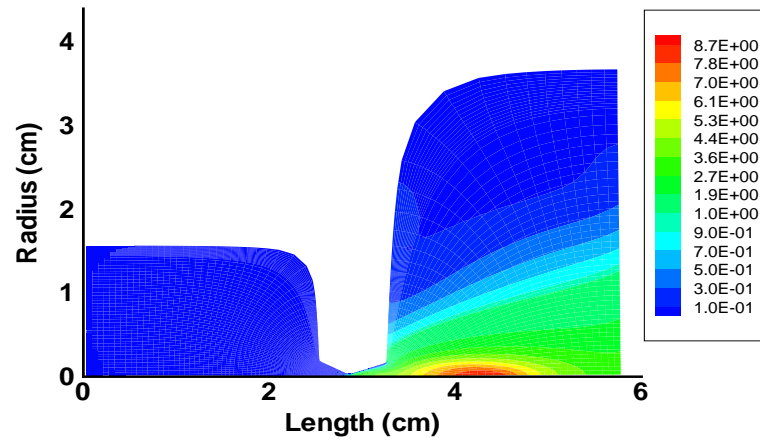


Figure 4.31: Mach number contours inside the 100 W MET.

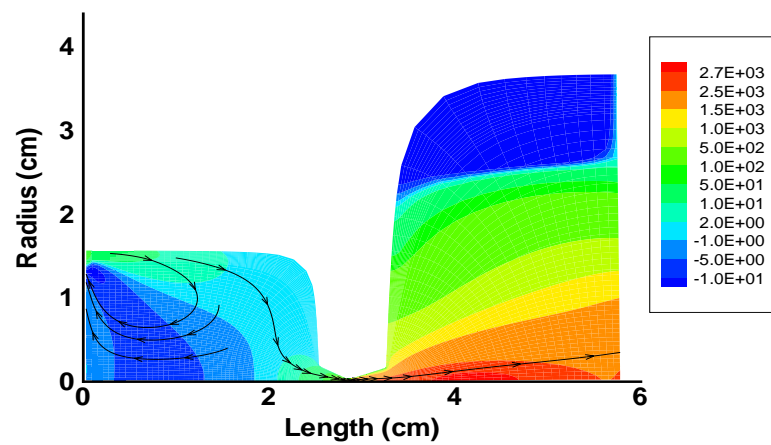


Figure 4.32: Axial velocity contours inside the 100 W MET (in m/sec).

4.2.2 Comparison with Thrust Data

A comparison is now made between the predicted value of specific impulse from the simulation and measured thrust data obtained by Sullivan [14]. It is important to mention here that the specific impulse measured by Sullivan at 9.6 MJ/kg, itself, was used to estimate the plenum wall temperature, together with the assumption of a wall recovery factor of 0.93, for the 100 W MET simulation, and as such the purpose of comparing the specific impulse from the simulation with the same measured specific impulse data point is to check, among other things, the validity of the wall temperature chosen for the calculation, and hence the wall recovery factor. For instance if the calculated specific impulse is less than the measured one, this could imply that the true wall temperature is higher than the assumed value and the wall recovery factor is greater. Alternatively it could imply that the fluid code does not capture the expansion fully, perhaps overestimating viscous effects by incorporating too much numerical dissipation.

The calculated thrust of the miniaturized 100 W MET is 22 mN, and the calculated mass flux through the nozzle is 8.9 mg/sec as inferred from Fig. 4.19. Using the calculated value of mass flux through the nozzle the specific impulse is 250 sec. As mentioned previously the calculated value of mass flux through the nozzle is different by about 12 % from the specified value at the inlet in this case, and some possible reasons for this are explored at the end of this chapter. If the specified mass flux at the inlet is used to calculate the specific impulse then result is 12 % lower, 220 sec.

Thrust data were obtained for the 100 W MET by Sullivan [14] using the plume momentum trap technique, which involves capturing the momentum of the exhaust jet from the thruster, and measuring it. In a recent study it was shown that the thrust of a standard MET, measured with a thrust stand and with the momentum trap, agree to within 5 % over a wide range of specific energies and different propellants [9]. The measured specific impulse of the 100 W MET, compiled using the momentum trap technique, is shown in Fig. 4.33. For a specific energy of about 10 MJ/kg, the specific impulse should be about 290 sec, according to the experimental thrust data, shown in Fig. 4.33. The calculated specific impulse for the 100 W MET is within 14 % of the measured value, and this may imply that the assumed wall recovery factor of 0.93, which was used to estimate the wall temperature for the calculation, is too low. The effect of the numerical dissipation level on the accuracy of the calculated mass flux through the nozzle is explored at the end of this chapter, and perhaps the numerical dissipation level also influences the accuracy of the specific impulse calculation.

Now some observations about the thrust data for the 100 W MET are made independent of the results of the calculation. The data collected by Sullivan [14] for the 100 W MET operating at 7.5 GHz are shown together with the measured values of specific impulse for the 1 kW MET at 2.45 GHz in Fig. 4.34. Also shown

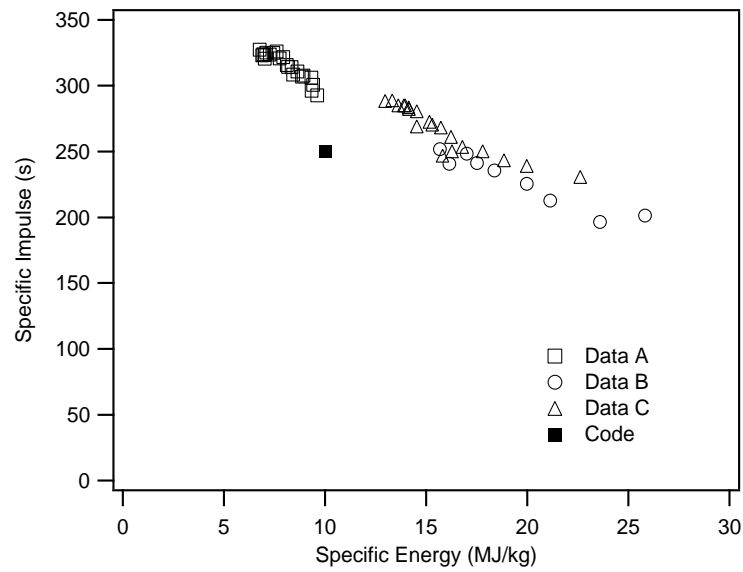


Figure 4.33: Measured values of specific impulse as a function of specific energy for the 100 W MET, taken by Sullivan [14]. The symbols indicate different sets of data that were collected at different times over a period of two days. No error bars were reported for the measured data. The blue square indicates the result from the present simulation, 250 sec, with a plenum wall temperature of 725 K.

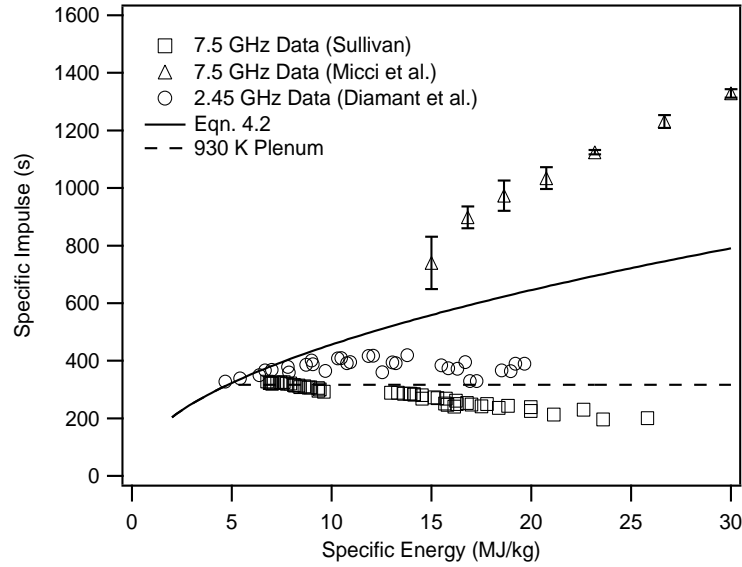


Figure 4.34: Measured values of specific impulse as a function of specific energy for the 100 W MET at 7.5 GHz, collected by Sullivan [14] and Micci *et al.* [58], and for the 1 kW MET at 2.45 GHz, collected by Diamant *et al.* [9].

in Fig. 4.34 is another set of specific impulse values determined by Micci *et al.* [58] for a helium thruster at 7.5 GHz similar to the 100 W MET discussed here. Micci *et al.* determined their values of specific impulse by measuring the axial exhaust velocity of the jet exiting the thruster; this was accomplished by observing the Doppler shift of the light emission from the plume.

The specific impulse values for the 100 W MET taken by Sullivan are consistently lower, being between 200 and 300 sec, as compared with those of the 1 kW MET which are generally between 300 and 400 sec. These two sets of data have the closest agreement near about 7 MJ/kg. The data of Micci *et al.* are considerably higher than those of either Sullivan or Diamant *et al.*. Shown together with all three sets of data, as the solid line, are the corresponding values of specific impulse calculated using Eqn. 4.2 with the specified specific energy. Also shown on the plot as the dashed line is the value of specific impulse which would be achieved if the plenum temperature was uniform and held fixed at 930 K, representing the melting point of aluminum. It is evident that above 15 MJ/kg the data for the 100 W MET taken by Sullivan do not approach the maximum value of specific impulse that can be achieved, as represented by Eqn. 4.2, but rather the value of specific impulse remains relatively flat, actually decreasing by about 20 %. Above 15 MJ/kg the measured specific impulse for the 1 kW thruster, while higher, does not approach the maximum attainable value either. The data of Micci *et al.* however consistently

exceed the maximum attainable specific impulse for this range of specific energy, and for this reason the data of Micci *et al.* are not considered further.

The specific impulse plateau, between about 8 and 14 MJ/kg, evident in the data taken by Sullivan and Diamant *et al.* could possibly be explained by the dominant role of thermal conduction through the plenum wall. After the plenum temperature reaches a certain value in the vicinity of 930 K, the conditions inside the plenum chamber are such that the further addition of microwave energy to the plasma does not impart additional enthalpy to the flow but rather adds entirely to the thermal conduction through the plenum wall.

The results of the calculation for the 100 W MET show that of the power absorbed in the plenum 80 % is transferred to the plenum wall due to thermal conduction. In addition the computed temperature profile is flat inside the plenum. These two characteristics of the current numerical simulation are consistent with the explanation that the temperature in the plenum is clamped by some mechanism near the aluminum melting point, and this gives rise the specific impulse plateau observed in the data taken by Sullivan and Diamant *et al.* presented in Fig. 4.34.

4.3 Mass Conservation

In the calculation for the 100 W MET presented in this chapter the steady state mass flux through the nozzle and the specified mass flux at the inlet are different, by as much as 12 % on average, even though there is little variation in total mass flux from one axial location to the next inside the nozzle and the calculation has thus converged to a steady state condition. The effect of grid refinement and numerical dissipation level on the accuracy of the steady state mass flux, determined by the current fluid model, is now explored by considering a simple problem of cold gas flow through a geometry similar to the 100 W thruster. It should be mentioned here that the numerical technique outlined in Chapter 3 is a conservative formulation, meaning that the total flux through the boundary of each cell should be conserved. The flux at each cell boundary is calculated using Eqn. 3.10. The mass flux in both Fig. 4.2 and Fig. 4.19, however, was not calculated using Eqn. 3.10, but rather it was determined directly from the values of density and velocity stored at the center of each cell. Because the mass flux through the center of each cell was determined and Eqn. 3.10 was not used, conservation is not guaranteed in a strict numerical sense, but nevertheless would occur in the true flow.

The plenum pressure and mass flow rate were measured experimentally for the 100 W MET, containing a larger nozzle than normal with a throat diameter of 0.79 mm. The measured values of mass flow rate as a function of plenum pressure are compared with the calculated mass flow rate from numerical simulations using the current fluid model. For these calculations, unlike the previous MET simula-

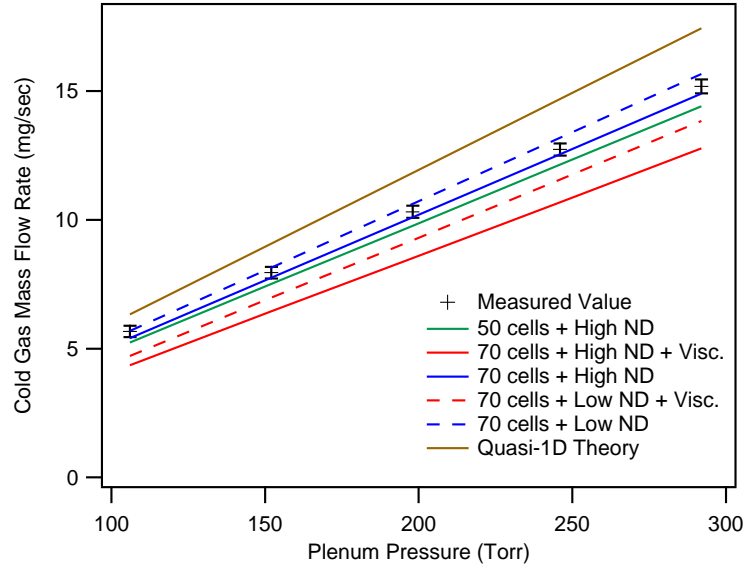


Figure 4.35: Calculated cold gas mass flux through the 100 W MET for different grid sizes and two levels of numerical dissipation with and without viscosity.

tions in this chapter, the boundary conditions at the left-hand side of the plenum are such that the pressure and temperature are specified, and the flow is allowed to enter the computational domain along the entire left-hand plane, not just the top 16 cells. There is no microwave energy addition or heat transfer through the plenum wall and the inlet temperature is taken to be 300 K, corresponding to experimental conditions. The axial velocity along the left-hand side of the plenum is extrapolated from the adjacent cells in the interior of the domain and evolves in time so that the code determines the appropriate steady state mass flux depending on the conditions in the plenum and the throat size. The results from these calculations and the measured data are presented in Fig. 4.35. Two levels of numerical dissipation were considered, one with $\alpha_1 = 0.5$ and $\alpha_2 = 0.1$, which is referred to as high numerical dissipation (ND), and another with $\alpha_1 = 0.3$ and $\alpha_2 = 0.3$ which is low numerical dissipation (ND). For most of the computations a grid consisting of 150 axial cells and 70 radial cells was used. Calculations were made with a grid that had only 50 radial cells and with no viscosity, as indicated by the green line in Fig. 4.35, and the resulting mass flux values are farther from the experimentally measured data than those of the more refined grid with 70 radial cells. Also the effect of the different levels of numerical dissipation is apparent for those calculations involving a viscous boundary layer. A lower level of numerical dissipation in the calculation helps to create a sharper boundary layer which leads to a higher mass flow rate, closer to the measured value, than in the case where a higher level

of numerical dissipation is used. Even with low numerical dissipation the actual measured mass flux is greater than that which is predicted by the viscous calculation. The corresponding inviscid calculation gives better agreement with the data. The mass flux predicted using Eqn. 4.1 is shown in Fig. 4.35 as well, and it is evident that the simple one-dimensional fluid theory over predicts the mass flow rate over the range of plenum pressure considered.

The results shown in Fig. 4.35 indicate that grid refinement and the level of numerical dissipation both influence the steady state mass flux predicted by the code. It was shown in general that by refining the grid and decreasing the level of numerical dissipation, the mass flux determined by the code can be brought into closer agreement with the experimentally measured values. Implementing a new numerical dissipation scheme that inherently has a lower level of numerical dissipation and refining the grid further, especially in the throat region, could improve the ability of the computation to match the specified value of mass flux for the 100 W MET case.

4.4 Summary of Model Performance

The results of this model for both the 1 kW and the 100 W thrusters portray a physical picture of what is occurring inside the MET which is markedly different than that expected from the previous equilibrium model [15]. According to that model a high temperature region is maintained near the centerline of the discharge, where there is significant electron number density and where most of the microwave energy is deposited. Both the electron number density and the gas temperature decrease substantially from their peak values on the centerline as one moves closer to the plenum wall. The current model is unique in that it does not predict large temperature gradients in the plenum, and in both of the cases explored in this chapter the temperature is relatively flat and close in magnitude to the prescribed plenum wall temperature. The electron temperature is an order of magnitude higher than the gas temperature, even at atmospheric pressures. In addition, for both cases, the electron number density is also relatively flat throughout the plenum, even though most of the electrons are produced in a confined region near the centerline, and the residence time associated with the re-circulation zone inside the plenum is high. There are significant gradients in the number density of each of the metastable species inside the plenum which occur despite the fact that the electron number density is flat. Although many of the elements of this new and distinct picture of the MET plenum are open to question, on the importance of having separate electron and heavy particle temperatures in the model there is no question.

There is some evidence that the current model, having painted this unique physical picture, does describe certain characteristics of the MET properly. The

spatial distribution of metastable species suggests a light emission pattern inside the plenum that would explain the physical appearance of real discharges in certain situations. For the case of the 1 kW MET the light emission is observed to be a compact ball in front of the converging nozzle and this seems to correlate well with the distribution of metastable states in Fig. 4.12 and Fig. 4.13. For the 100 W MET the arrowhead configuration with its sharp spike reaching towards the converging nozzle, as shown in both Fig. 4.29 and Fig. 4.30, invokes the image of the narrow, filament arc observed for argon discharges in the two-stage thruster, as described in Chapter 6. On a more quantitative note, the radial profile of electron temperature predicted for the 1 kW MET compares well with the measured profile by Balaam [12], as shown in Fig. 4.16. Finally given a rough estimate for the stagnation temperature, based on measurements of mass flow rate and plenum pressure, the current model does succeed in predicting the specific impulse for the 1 kW single-stage thruster to within 20 %, and it gives a plausible estimate for the thermal heat loss at the wall as well.

More work could be done to improve the current model in addition to those steps related to numerical dissipation and grid refinement as outlined in the previous section. Adding an azimuthal velocity component to the model, which is present in the real MET, may enable the model to capture gradients in temperature and pressure in the plenum if significant gradients exist, as thrust data seems to suggest they do. Finding a new estimate for the plenum wall temperature may also enable the current model to better predict the plenum pressure and the specific impulse for the single-stage thrusters.

Chapter 5

LIF Spectroscopy

A goal of this thesis is to quantify the effect of supersonic energy addition in the two-stage microwave thruster described in Chapter 2. LIF spectroscopy was used to do this, by measuring the temperature at several points in the exhaust plume of the two-stage thruster. In addition LIF spectroscopy allows the velocity components of the flow to be determined simultaneously as well. LIF spectroscopy relies on the use of a narrow linewidth laser which is tunable in frequency over the range of interest, typically 10 GHz or so, to excite an atomic or molecular transition. The fluorescence from this transition, which occurs as the excited state returns to the initial state, is detected using a photodiode or another light-sensitive instrument. In this chapter the experimental technique of LIF spectroscopy is described in detail, and the relevant principles necessary for interpreting the LIF signal to find the temperature and velocity are reviewed. First a brief history of the technique is presented, followed by a description of the experimental setup used in the two-stage thruster experiments. A theoretical treatment of a Doppler-broadened line-shape, representing the LIF signal from the exhaust plume of the thruster, is then given. Finally the Ti-Sapphire solid-state laser used to make the LIF measurements is described, and the method used to characterize its frequency stability and mode separation is discussed.

5.1 LIF History

This technique was first used more than twenty years ago by Miles *et al.* [59] to study supersonic flows in a windtunnel. In this work sodium vapor was seeded in small quantities into the flow and an atomic transition in sodium was excited using a laser. Velocity and temperature were determined from the LIF signal, which was collected at 90 degrees from the incident laser beam. This work also employed a novel approach of reflecting the laser beam back into the experiment so that an LIF signal could be generated from both forward and backward moving laser pho-

tons. The flow velocity could then be determined, as half the distance between the two peaks thus eliminating the need for a frequency marker. Subsequent to this work a new technique was developed by the same group where a transition from a vibrational excited-state of molecular oxygen was used, eliminating the need for seeding the flow [60]. In implementing this technique excited oxygen atoms were first created by optically pumping the molecules using a two-color beam, generated by passing the high power beam of a pulsed YAG laser through an oxygen Raman cell. In this way a line of tagged molecules could be created in the flow. These excited-state molecules were interrogated using an argon-fluoride excimer laser, operating at 193 nm corresponding to one of the electronic transitions from the oxygen vibrational state. The argon-fluoride beam was focused into a planar sheet and the fluorescence from oxygen molecules was then observed. By interrogating this line at different time intervals and observing the position of the line the velocity of the flow could be determined.

In more recent times LIF spectroscopy has been used as a diagnostic tool for studying the plume characteristics of electric propulsion thrusters. In a seminal work, Keefer *et al.* [61] measured the temperature and velocity profile in the exhaust plume of an arcjet thruster, running on argon. By crossing two separate laser beams at the point of interest, each with a different angle relative to the centerline of the flow the authors were able to measure both the axial and radial components of velocity simultaneously. In addition a part of the laser beam was sent through an optogalvanic discharge cell, and the optogalvanic signal provided a precise frequency marker that facilitated the determination of the velocity components from the LIF signals. The details of how an optogalvanic cell can be used for this purpose will be described later.

5.2 Experimental Setup

The LIF experiments with the prototype two-stage thruster were conducted using an arrangement shown in Fig. 5.1. There are four basic components in these experiments: a solid-state laser system, a computer interface for data acquisition and control of the laser scanning rate, the two-stage thruster, and a vacuum tank. The two-stage thruster was run with argon gas, and the pressure in the plenum section of the thruster was measured using a mechanical pressure gauge connected to the thruster through a 1 mm pressure tap, located about 1 cm above the gas injection ports. The plenum pressure was typically 240 Torr during the experiments. Electrical power to the microwave magnetron connected to the first stage of the thruster was supplied by a high voltage power supply, operating at nominally 4.2 kV and 300 mA. This magnetron is Panasonic model 2M261-M32 with a rated power of 1.2 kW and an efficiency of 70 percent, as specified by the manufacturer. An additional power supply was used to heat the magnetron filament.

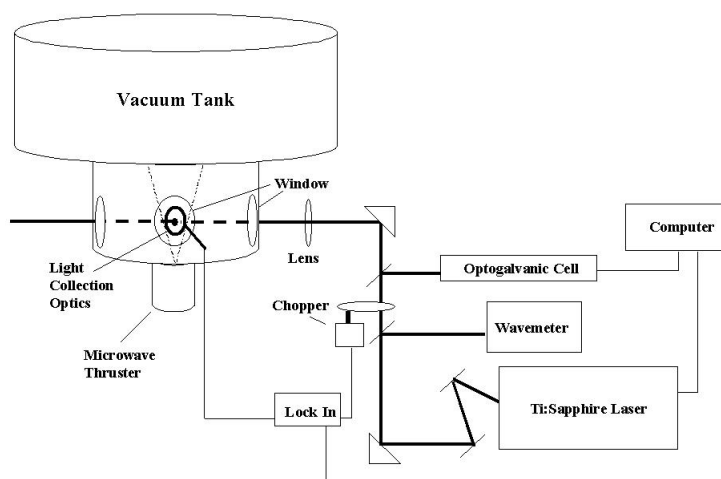


Figure 5.1: Schematic of the experimental setup for the LIF measurements with the two-stage thruster.

The thruster was mounted to a custom built cylindrical aluminum piece with an inside diameter of 15.24 cm, which connects directly to an aluminum vacuum tank. The cylindrical extension piece holds optical view ports for viewing the exhaust plume of the thruster. The windows are made from commercial glass, and the view ports are 1.91 cm in diameter. There are three view ports, two of which are on opposing sides of the cylindrical wall and the third is at 90 degrees relative to the other two. The vacuum tank is approximately 0.72 m in diameter and 1.4 m in length. This vacuum tank is connected to a 300 CFM mechanical pump which was able to maintain a background pressure of roughly 2.5 Torr in the vacuum tank during normal thruster operation.

The solid-state Ti:Sapphire laser is a commercial Titan ring-cavity laser manufactured by Schwartz Electro-Optics, which is pumped by a Lexel argon-ion laser of nominally 6 W running on multiple lines. The output from this laser is directed into a Burleigh Wavemeter, which can measure the laser wavelength to six significant figures. The frequency of the solid-state laser was adjusted in 240 MHz increments corresponding to the laser cavity mode separation by adjusting the voltage applied to an intra-cavity etalon. The details of how the cavity mode separation was determined experimentally are discussed later.

The transition of interest in this work is the argon transition (Ar I) at a vacuum wavelength of 772.589 nm, from the $4s[3/2]_2$ metastable level to the $4p[3/2]_1$ level. The fluorescence from the $4p[3/2]_1$ level consists of four different transitions whose

wavelengths are displayed in Table 5.1 together with the lower and upper levels for each transition and the corresponding spontaneous emission rate coefficient (A_{mn}). The data collected for this table was based on the original work of Wiese [51], with updated values for A_{mn} from the National Institute of Standards (NIST) Atomic Spectroscopy website. The spontaneous emission rate coefficient corresponding to

Table 5.1: Fluorescence Transitions from the $4p[3/2]_1$ Level

Vacuum Wavelength (nm)	Lower Level (n)	Upper Level (m)	A_{mn} (sec^{-1})
772.589	$4s[3/2]_2$	$4p[3/2]_1$	5.2×10^{-6}
810.592	$4s[3/2]_1$	$4p[3/2]_1$	2.5×10^{-7}
867.032	$4s'[1/2]_0$	$4p[3/2]_1$	2.4×10^{-6}
935.679	$4s'[1/2]_1$	$4p[3/2]_1$	1.1×10^{-6}

the fluorescence at 810 nm is an order of magnitude larger than the value for the other transitions in Table 5.1, and thus light at 810 nm is the dominant component of the fluorescence. In making the LIF measurements the transition at 772 nm from the $4s[3/2]_2$ metastable level was chosen because the lifetime of the $4s[3/2]_2$ level is such that after it is created in the microwave discharge in the plenum it is still present in sufficient numbers in the exhaust plume to see an LIF signal. The particular transition from the $4s[3/2]_2$ level to the $4p[3/2]_1$ level is especially useful not just because it originates from a metastable level, but also because most of the fluorescence from the resulting level, the $4p[3/2]_1$ level, occurs at a frequency other than the transition frequency, as evident in Table 5.1. Thus it is possible to achieve a good signal-to-noise ratio by filtering out various sources of scattered laser light from the windows, vacuum tank walls, etc. A suitable bandpass filter centered at 810 nm with a width of approximately 10 nm was placed in front of the photodiode for this purpose.

Following the path of the laser beam as it leaves the solid-state laser, illustrated in Fig. 5.1, the laser beam is split into two parts. One part is directed into the Burleigh Wavemeter, which provides a measurement of wavelength so that the laser can be manually tuned into the wavelength range corresponding to the chosen transition. The other part is directed through an optical chopper, which modulates the laser beam at a frequency of approximately 218 Hz, and then is directed through a window into the vacuum tank.

Before entering the tank the beam passes through a plano-convex lens with a focal length of 150 mm and is subsequently focused to a point in the exhaust plume of the thruster, 7 mm downstream of the exit. The laser beam diameter coming out of the solid-state laser is approximately 5 mm, and the focusing lens reduces this to roughly 30 μm . The depth-of-focus of the focused beam is roughly 1.8 mm. Flu-

orescence is collected at a 90 degree angle relative to the focused beam by a 25 mm bi-convex lens and focused onto a photodiode. The collection lens and photodiode are arranged so that the image of the plume is reduced by a factor of 4.6. A 150 μm pinhole aperture is placed in front of the photodiode to ensure that light from only a 0.7 mm diameter spot is collected from the plume. In the radial direction moving away from the centerline of the plume, the spatial resolution of the LIF measurements in this work is 0.7 mm and in the axial direction it is 30 μm , which is the diameter of the focused laser beam. Both the laser focusing lens and the light collection optics are mounted on linear translation stages bolted directly to the cylindrical piece connecting the thruster with the vacuum tank, in front of two perpendicular view ports, respectively. Each linear translation stage can move 5 mm in either direction. Both of the stages are intended to move together in unison, as a radial scan across the plume is made.

A second leg of the modulated laser beam is directed into an optogalvanic cell, which is meant to provide a precise frequency marker. The optogalvanic cell is basically a hollow-cathode argon discharge lamp with a discharge voltage anywhere between 350 and 450 V. The lamp current is held constant at a few tens of milliamperes by using the appropriate ballast resistor. As the laser is tuned through the argon transition line at 772 nm, the voltage on the lamp changes by a small amount (a few tens of millivolts). This change is detected using a lock-in amplifier, or phase-sensitive detector, which picks out the voltage variation corresponding to the laser modulation frequency. The optogalvanic signal is recorded simultaneously with the LIF signal, thus providing a precise frequency marker, facilitating the determination of the velocity from the data.

The lock-in amplifiers used in this experiment were Stanford Instruments model SR-830 dual channel, digital lock-in amplifiers. The signal from each of these, one corresponding to the optogalvanic cell and the other to the photodiode, is connected to a personal computer with a National Instruments PCI-MIO-16XE-50 data acquisition card, via a BNC-2110 conditioning board. The control signal for the laser frequency sweep is also connected to this board. A program was written using LabView software to supply the necessary voltage to the laser to accomplish a frequency scan at a rate of 60 points per minute and to collect the data from the lock-in amplifiers in a synchronous manner.

5.3 LIF Theory

For the case of the exhaust plume of the microwave thruster, under the conditions outlined above, it is entirely appropriate to assume that other contributions to the linewidth such as those due to pressure broadening effects are negligible since the pressure in the vacuum tank is maintained at 2.5 Torr. Pressure broadening is important in the plenum section of the thruster, and the following theory

for analyzing the LIF data would have to be augmented in that case to include pressure-broadening effects. The lineshape of the LIF signal in the plume reflects a Doppler-broadened transition, the details of which are now described.

The theory describing a Doppler-broadened lineshape of an atomic or molecular transition in a gas is relatively straightforward. Consider the argon gas in the plume of the thruster which can be modeled as having two components of velocity, an axial component directed along the plume, \bar{v}_z , and a radial component, \bar{v}_r , directed perpendicular to it. At a given temperature the velocity distribution of the argon atoms is Maxwellian, according to the following formula

$$f = \frac{N_A}{\pi\sigma^2} e^{-[(v_z - \bar{v}_z)^2 + (v_r - \bar{v}_r)^2]/\sigma^2}, \quad (5.1)$$

where N_A is the number density of atoms, and \bar{v}_z and \bar{v}_r are the average values of axial and radial velocity. σ is related to the gas temperature, according to $kT = 1/2 m \sigma^2$. Now consider a laser beam propagating at an angle ϕ with respect to the centerline. Because different atoms are moving at different velocities with the distribution of velocity governed by Eqn. 5.1, different atoms see photons of different frequencies in their respective reference frames. For an atom moving with velocity components v_z and v_r this frequency shift is $(v_z \cos \phi + v_r \sin \phi) / \lambda$, where λ is the laser wavelength. The total LIF signal, S , is proportional the integral of the velocity distribution function,

$$S = C_\phi \int \int_A f dv_r dv_z. \quad (5.2)$$

C_ϕ is a constant which depends on the geometry of the optics and the laser power. The band of integration, A , comprises the region in velocity space where the following inequality holds,

$$|v_z \cos \phi + v_r \sin \phi + \lambda(\nu_L - \nu_0)| < 1/2 \lambda \Delta\nu,$$

with $\Delta\nu$ being the laser linewidth (in sec^{-1}) and ν_L the laser frequency. The final result for the LIF signal, S , is a Gaussian curve which depends on the difference between the laser frequency and the frequency of the transition, $\nu_L - \nu_0$, given below

$$S = \frac{n_a C_\phi \Delta\nu}{\pi\sigma} \exp - \left[\frac{\lambda(\nu_L - \nu_0) + v_\phi}{\sigma} \right]^2, \quad (5.3)$$

where $v_\phi = \bar{v}_z \cos \phi + \bar{v}_r \sin \phi$. The width of this Gaussian curve is related to the gas temperature, and the horizontal shift of the curve along the frequency axis is related to the magnitude of the two velocity components and the angle of the laser beam relative to the flow. By recording this spectral lineshape as a function of laser

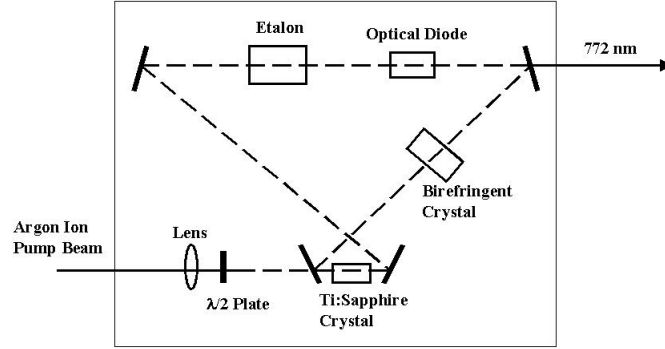


Figure 5.2: Ti:Sapphire solid-state laser system used as the light source for the LIF measurements.

frequency it is possible to determine the temperature and the velocity of the flow relative to the laser beam, v_ϕ , simultaneously. In order to determine both velocity components it is necessary to measure the LIF spectral profile for two different values of ϕ .

5.4 Ti:Sapphire Laser System

A critical element of the experimental system for making LIF measurements is the tunable laser. Dye lasers have been used for many years for this kind of work, since laser dyes are commercially available which collectively cover the wavelength range from 400 nm to 700 nm continuously. For longer wavelengths Ti:Sapphire has become the laser medium of choice since Ti:Sapphire crystals have a broad gain curve which allows lasing to occur from about 660 nm to almost 1100 nm. In this work a Ti:Sapphire laser system is utilized, configured with coated mirrors so that lasing is possible between approximately 730 nm and 830 nm. In order to complete the LIF experimental work described in this thesis it was necessary first to completely realign the Ti:Sapphire laser system. The complete system in full working order is now described, followed by the experimental determination of its spectral characteristics.

A diagram of the laser system is shown in Fig. 5.2. The Ti:Sapphire crystal with polished end surfaces, each cut at a Brewsters angle, is mounted on a water-cooled

aluminum block in the center of the cavity. The cavity is a ring type configuration, as opposed to a straight standing wave cavity. The ring configuration makes it possible to achieve a narrow linewidth laser beam, and this feature is common in commercial tunable dye lasers as well. The crystal is optically pumped using an argon-ion laser. The argon-ion laser beam is sent through a half-wave plate, which rotates its polarization from vertical to horizontal, and focused inside the crystal using a lens. It is necessary to rotate the polarization of the argon-ion beam so that reflection from the surface of the crystal is minimized. The path traced out by the laser photons after they leave the crystal is shown in Fig. 5.2. Light is directed along the ring by four mirrors. One mirror is a highly reflecting optical flat and another is the output coupler. An optical diode is placed in the ring to ensure that lasing occurs in only one direction. A birefringent crystal is also placed in the ring cavity; this component allows coarse tuning of the laser wavelength to be accomplished over many tens of nanometers. For fine adjustments an intra-cavity etalon is utilized. This etalon is a confocal, air-spaced optical cavity. One of the etalon mirrors is connected to a piezo-electric crystal. The mirror position, and hence the transmission frequency of the etalon, changes when a voltage is applied to the crystal.

The etalon is the essential element in scanning the laser over a frequency range of a few GHz in the vicinity of the chosen transition. For the ring configuration described above certain frequencies will be resonant in the optical cavity. The resonant frequencies are such that an integral number of wavelengths of light fit inside the ring cavity. These allowable frequencies are referred to as the cavity modes or the axial modes. The etalon makes it possible to change the laser frequency from one cavity mode to the next. The frequency separation between the cavity modes is a function of the laser geometry, and can be measured precisely by characterizing the spectral output of the laser.

To characterize the spectral output of the Ti:Sapphire system another confocal, air-spaced etalon was used, a Burliegh model RC-46 Spectrum Analyzer. This instrument was placed outside the laser cavity, in front of the beam and aligned so cavity modes were excited in the etalon by the laser beam. The free-spectral range of this etalon is 2 GHz, with a finesse of 200. Prior to using this etalon the spacing between the two mirrors was manually adjusted, according to the instructions provided by the manufacturer, to ensure that the etalon was in fact setup in a confocal arrangement. During normal operation of this instrument a voltage is applied to a piezo-electric transducer, which moves one of the mirrors slightly by a few microns. The transmission frequency of the etalon then changes according to the formula,

$$\Delta f = -f \frac{\Delta d}{d}, \quad (5.4)$$

where f and d are the unperturbed frequency and mirror spacing respectively.

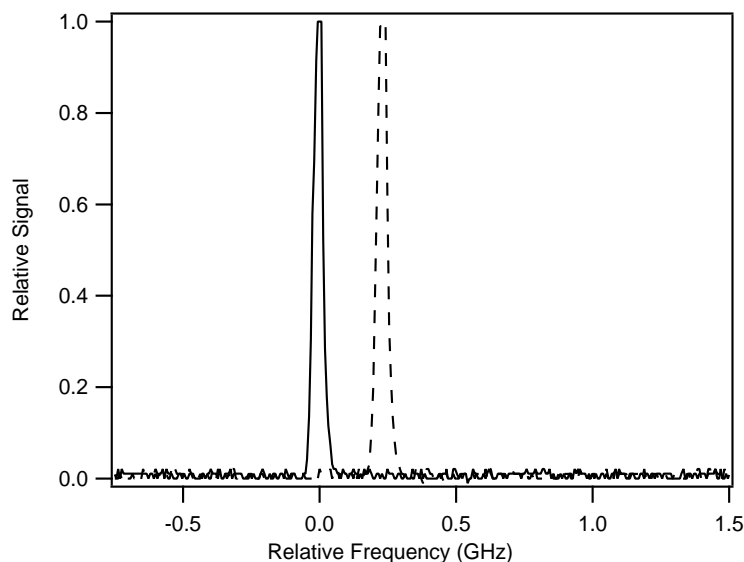


Figure 5.3: Measured linewidth of Ti:Sapphire laser. The solid and dashed lines indicate two separate cavity modes, recorded at two different times.

A photodiode measures the intensity of light transmission through the etalon. In practice, Δd is linear with the applied voltage and d is not known. The etalon spectrum must be calibrated, therefore, in terms of Δf versus applied etalon voltage. This was accomplished in a separate experiment in which the spectrum of a narrow linewidth laser was recorded using the etalon. The separation of two successive transmission peaks in this experiment represented a distance of one free-spectral range in frequency space, and this was used to calibrate the etalon.

The etalon, Burliegh model RC-46, was then used to characterize the Ti:Sapphire laser linewidth and determine the cavity mode separation, as shown in Fig. 5.3. Two traces are shown in Fig. 5.3, which were recorded at two different times. At any given instant the laser is operating with a single mode, represented by the solid line in Fig. 5.3. It is evident that the linewidth of this mode is about 40 MHz. The second trace, represented by the dashed line, is the cavity mode at a later time after the voltage sent to the intra-cavity etalon indicated in Fig. 5.2 is increased by 1 V. As seen in Fig. 5.3 the frequency of the Ti:Sapphire laser changes by about 240 MHz due to this voltage increment, and this value is the experimentally determined cavity mode separation. In the LIF experiments described in the next chapter the scans through the metastable argon transition line were performed by changing the voltage on the intra-cavity etalon in 1 V increments, thus changing the laser frequency in 240 MHz increments.

Chapter 6

LIF Data and Model Predictions

The LIF technique, described in the last chapter, was used to measure the temperature and velocity in the exhaust plume of the two-stage thruster, discussed in Chapter 2, and the results of this effort are now presented. Two sets of measurements were performed, for the two-stage thruster running on argon propellant, in situations where there was only subsonic energy addition and where there was both subsonic and supersonic energy addition. Argon was chosen as the propellant gas for these experiments so that the solid-state laser described in Chapter 5 could be used to excite an argon metastable transition. Temperature values were determined using LIF spectroscopy at several radial positions in the expanding jet, exhausting from the thruster. As supersonic energy is added, it is shown experimentally that the temperature, near the centerline of the plume, increases slightly, and there is a more significant temperature increase at the outer edge of the plume. The numerical model, developed in Chapter 3, is used to simulate the supersonic stage of the two-stage thruster, and a comparison is made with the experimental data. In a separate calculation the subsonic stage of the thruster is studied so that the plasma properties inside the plenum can be visualized.

Results from the LIF measurements for the case of only subsonic energy addition are given first. The two-stage thruster operates with approximately 900 W of microwave energy addition in the plenum section. A highly compact filament is observed when the thruster operates on argon. A comparison is made with the calculated temperature values in the plume. Because the temperature and velocity profiles of the exhausting jet depend largely on two parameters, the average temperature and pressure in the plenum, and not on the characteristics of the plasma in the plenum, the complete model of Chapter 3 is not used in this instance for comparison with the LIF data, but rather a simplified model incorporating just the fluid equations with transport is employed, starting from fixed plenum conditions. In this simulation the measured plenum pressure and an estimate of the stagnation temperature in the plenum are used. The numerical grid for these calculations is presented including the nozzle section of the two-stage thruster and the vacuum

expansion section where the LIF data is collected. The temperature values in the plume, determined from the LIF measurements, are shown together with the corresponding predicted values from the fluid simulation. These LIF measurements indicate lower temperatures in the plume than what would be expected if the full 900 W was imparted to the flow, and this supports the fact that thermal conduction to the thruster walls is an important component in the overall energy balance in the two-stage thruster. A measurement of axial velocity close to the centerline of the exhausting plume is made, using the optogalvanic cell to generate a frequency reference. This result is also compared with the predicted value of axial velocity from the model.

Having compared the LIF data for the subsonic stage with the results of the fluid simulation, starting from fixed conditions in the plenum, a more detailed study is then made of the subsonic stage of the two-stage thruster for the case using the complete model developed in Chapter 3, so that the plasma properties in the subsonic stage can be visualized. The focus of this calculation is not on the plume properties, but rather on the conditions inside the plenum. The numerical grid for the simulation of the subsonic stage of the two-stage thruster is presented. The contours of gas temperature and electron temperature are shown, as well as many of the other properties which were computed for the single-stage METs in Chapter 4. There are significant physical differences between the argon discharge in the two-stage thruster, and the helium discharges computed previously. These are highlighted.

The last part of this chapter concentrates on measurements made with the two-stage thruster operating with about 80 W of supersonic energy addition, in addition to subsonic energy addition. The central experimental result presented is the temperature profile of the jet. This is compared with the experimental result for the case of only subsonic energy addition. A numerical simulation is then used to help explain the difference between the two profiles. Calculations for the case of supersonic energy addition involve the full model of Chapter 3 applied to the supersonic stage of the two-stage thruster. A measurement of axial velocity close to the centerline was also made for the case of supersonic energy addition. The result from this measurement is discussed. Finally the important conclusions from this chapter are summarized.

6.1 Two-Stage Thruster with Subsonic Energy Addition

Experiments were done with the two-stage thruster involving only subsonic energy addition, as a first step in exploring the complete thruster. The typical operating conditions for the two-stage thruster encompass a mass flow rate of about

570 mg/sec and a plenum pressure of 240 Torr. Both of these quantities were measured. The appearance of the discharge inside the plenum is described briefly, and the measured values of temperature in the plume are presented. A measurement of axial velocity was made for this case as well, using the optogalvanic cell described in Chapter 5. Fluid calculations indicate that a relatively compact plume forms under these conditions.

For argon propellant a highly compact filament formed in the plenum section of the two-stage thruster under certain conditions. About two hundred holes, approximately 1 mm in diameter, were drilled into the plenum chamber, allowing the light emission from the plasma to be observed while the thruster was firing. The first step in creating the plasma was to evacuate the plenum chamber down to roughly 0.3 Torr. At this point a diffuse glow discharge was created, filling the entire plenum chamber, by activating the microwave magnetron connected directly to the subsonic stage of the thruster, as shown in Fig. 2.6. The valve was then opened for mass flow to move into the thruster, and as the pressure in the plenum chamber began to rise a compact ball appeared in the plenum chamber. As the mass flow rate was increased further toward the final value of 570 mg/sec, the ball moved closer to the entrance of the converging nozzle and remained in this location. The final pressure in the plenum was about 240 Torr, and at this point the light emission changed from a ball to an intense, narrow filament. The filament was located on the centerline and stretched from the entrance of the converging nozzle to the boron nitride pressure plate. The absorbed microwave power in this situation was roughly 900 W, estimated from the current and voltage displayed on the high voltage power supply, 300 mA and 4.2 kV, and the known efficiency of the magnetron, 70 %. In making this estimate it was assumed that the reflected power was small because the dimensions of the subsonic stage had already been optimized for minimum reflection [22]. Once created this filament was stable over a range of absorbed power. The filament extinguished when the flow rate through the thruster was reduced significantly. This filament was present in all cases where LIF data was collected. Such a phenomenon was not observed when helium or air discharges were created in the thruster. The presence of the filament also corresponded to an increase in the LIF signal recorded in the plume, which was due to an increase in the number of argon $4s[3/2]_2$ metastable levels produced in the plenum.

6.1.1 LIF Measurements

As mentioned in Chapter 5 the LIF measurements required that a laser beam was focused in the plume of this thruster, about 7 mm from the nozzle exit. The optics for focusing and light collection were attached directly to the transition piece, connecting the thruster to the vacuum tank, as described in Chapter 5. The laser

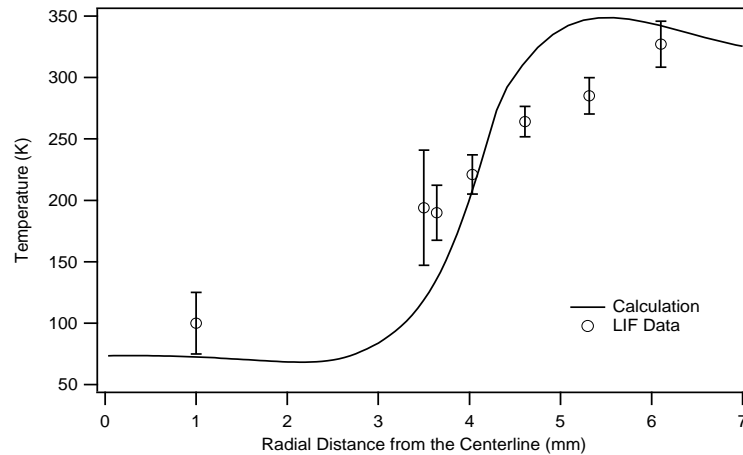


Figure 6.1: Measured temperature in the exhaust plume of the two-stage thruster. The solid line indicates the result from the fluid simulation, with a stagnation temperature of 500 K in the plenum.

beam was aligned to the centers of both the opposing windows on the transition piece, and scattered light was collected at 90 degrees relative to the incident beam. After alignment the nozzle centerline and the laser beam were perpendicular but offset slightly in the vertical direction, relative to the bottom of the vacuum tank. This is because the supersonic stage and the vacuum transition piece are not exactly concentric. Since this problem was not easily correctable a measurement of the vertical displacement between the centers of the two pieces was made, and the resulting value of 3.5 mm was considered in determining the spatial profile of the LIF data presented in this thesis.

LIF temperature measurements were made when the thruster operated as described above, for a few points in the plume 7 mm in front of the exit, and the results are shown in Fig. 6.1. A horizontal scan through the plume was made relative to the bottom of the vacuum tank by adjusting the focal point of the laser beam in one millimeter increments and moving the light collection system (photodiode and lens) in unison, using linear translation stages as described in Chapter 5. The temperature values from the LIF measurements are plotted as a function of radial distance from the plume centerline in Fig. 6.1, and the vertical displacement between the beam and the plume centerline was considered in determining the radial distance. A temperature of roughly 220 ± 20 K is measured at a point about 4 mm from the centerline. The temperature gradually increases to 330 ± 20 K, 6.1 mm from the centerline. Both of these temperature values agree reasonably well with the predicted values from the fluid simulation, which are 210 and 340 K at these locations respectively. At radial distances of 4.6 mm and 5.3 mm the agreement is

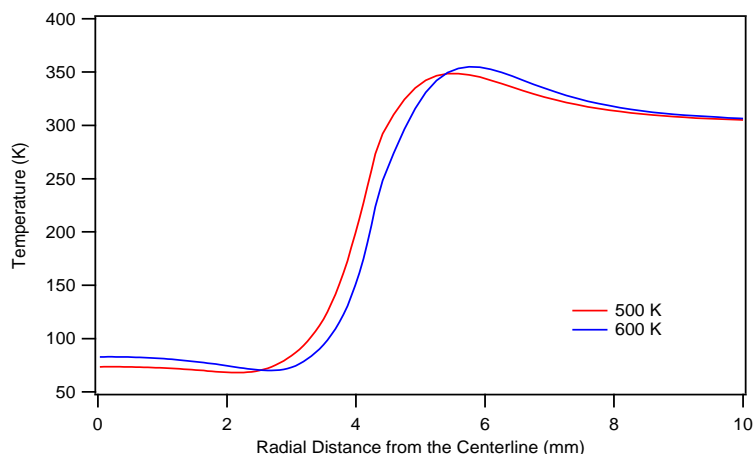


Figure 6.2: The calculated temperature profile in the plume for two different temperatures in the plenum.

not as good.

The fluid simulation started from a plenum temperature of 500 K, as calculated from the measured mass flow rate and plenum pressure using Eqn. 4.1. The sensitivity of the predicted profile in the plume to the plenum temperature used in the calculation is explored in Fig. 6.2. The plenum pressure was fixed at 240 Torr for the two cases plotted in Fig. 6.2. For the 600 K case the calculated mass flow rate was 500 mg/sec and for the 500 K case it was 520 mg/sec. The calculation with a 500 K plenum gives a closer agreement with the measured mass flow rate value of 570 mg/sec, and for this reason the calculation with a 500 K plenum is used to compare with the LIF data. The calculation with a 600 K plenum, however, gives a better agreement with the measured temperature on the centerline in the plume, with the difference in temperature between the two calculations being roughly 10 K.

The LIF signal corresponding to the 4 mm point is shown in Fig. 6.3. There are thirty points, total, in a laser single scan, about ten of which occur inside the LIF peak. The remaining points are averaged to determine the background noise level. The background noise level is subtracted from the data, and the result normalized by the peak signal to generate the final LIF signal, as exemplified by Fig. 6.3. The standard deviation of the background noise, normalized by the peak signal, is used as an estimate for the error bar. The error bar is the same for all the points. A Gaussian curve is fit to the LIF signal so obtained, as shown in Fig. 6.3. The fit is computed using the standard Marquardt method [48], which determines an error estimate for each of the parameters in the fit, in addition to generating the fit itself. The characteristics of Fig. 6.3 are indicative of the other data, taken at different

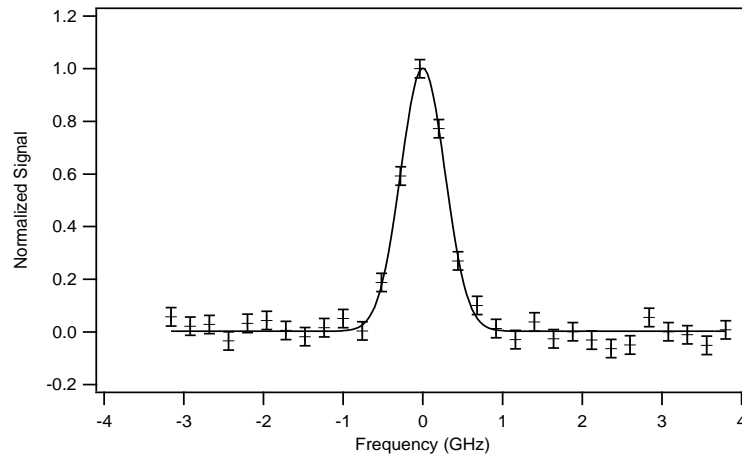


Figure 6.3: LIF data used to determine the temperature 4 mm above the centerline of the plume. The solid line is a Gaussian fit to the measured data.

points in the plume. This data reduction procedure was followed for all the LIF data presented in this chapter.

A separate experiment was performed to measure the flow velocity, using the optogalvanic cell to generate a frequency marker. The LIF signal was measured at a point 7 mm in front of the nozzle exit and about 1 mm away from the plume centerline. For the axial velocity measurements only, the laser beam was directed from the nozzle exit towards the throat, parallel to the centerline. A 500 mm lens was used to focus the beam, with $f\# = 100$. The spot size with this lens is about $100\ \mu\text{m}$, and the depth-of-focus is about 20 mm. The same light collection arrangement was used as the one described in Chapter 5 for making the radial temperature measurements, which were just presented. The resolution of this velocity measurement is, therefore, $100\ \mu\text{m}$ in the radial direction and 0.7 mm in the axial direction. The results of this experiment are shown in Fig. 6.4. The measured value of axial velocity is $500 \pm 20\ \text{m/sec}$, which is about 25 % smaller than the computed value of about 670 m/sec with a 500 K plenum. The corresponding temperature for this point is $100 \pm 30\ \text{K}$, and this point was included with the other radial temperature measurements in Fig. 6.1.

6.1.2 Comparison with Fluid Simulation

A fluid simulation was done of the flow inside the expanding nozzle and near the exit of the two-stage thruster, starting from specified conditions in the plenum so that a comparison could be made with the measured temperature and velocity in the exhaust plume. As mentioned at the beginning of this chapter since the exit

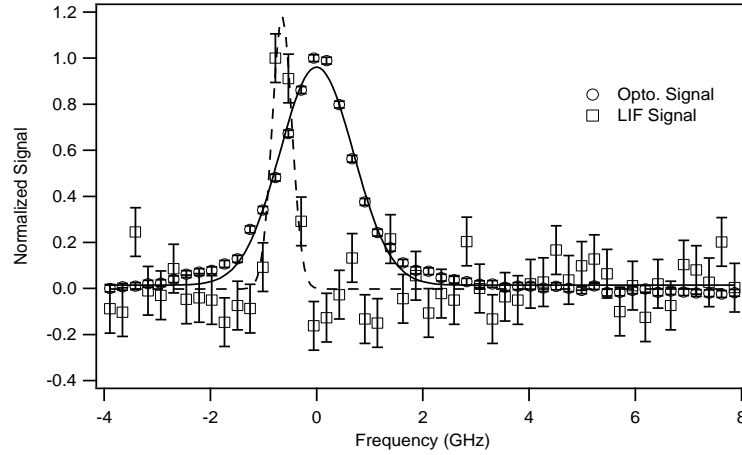


Figure 6.4: LIF and optogalvanic signals used to determine the axial velocity. The solid line is a Gaussian fit to the LIF data and the dashed line to the optogalvanic data.

temperature and velocity depend largely on the average temperature and pressure in the plenum, for the purposes of comparing with the LIF data it was not necessary to simulate the plasma processes in the plenum using the full model of Chapter 3. The details of the fluid calculation performed to generate theoretical curve used for comparison in Fig. 6.1 are now described, and the complete results for the temperature and Mach number in the simplified geometry are presented.

The grid used for the fluid simulations in this chapter which are compared with LIF data is shown in Fig. 6.5. Unlike the grids generated for the MET simulations in Chapter 4, this simplified grid is not based on a curvilinear, orthogonal coordinate system, and there are two distinct regions of the grid indicated by different colors in Fig. 6.5. The red lines indicate the grid for the nozzle section, and the green lines indicate the grid for the vacuum expansion section. The red region is composed of 300 axial cells and 70 radial cells. The green region is composed of 100 axial cells and 100 radial cells.

In this fluid simulation unlike previous simulations involving single-stage METs the temperature and pressure are specified at the inlet of the nozzle section, as shown in Fig. 6.5. There is no plenum chamber or back plate or energy addition processes. At the inlet there is a single component of velocity in the axial direction. The inlet velocity at any given instant is extrapolated from the interior of the domain, such that its derivative at the inlet is zero. In this way the pressure at the inlet can remain constant throughout the calculation. The total mass flow rate into the domain is not constrained in these simulations, and the code predicts what the final mass flow rate should be based on the specified stagnation conditions and the

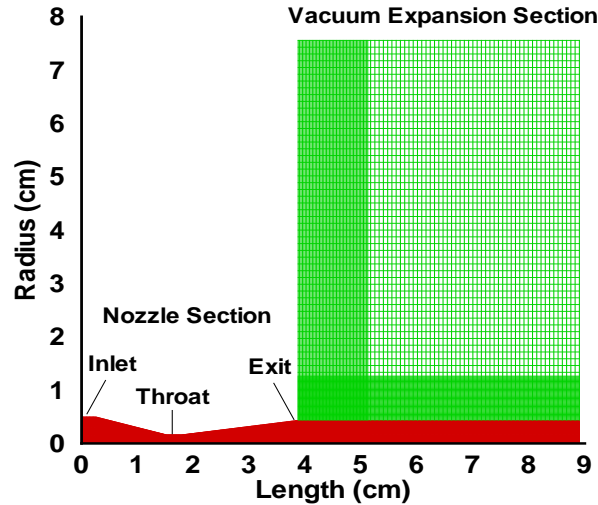


Figure 6.5: Simplified grid used to generate results for comparison with LIF data.

nozzle geometry. The pressure at the inlet is fixed at 240 Torr, the measured operating pressure of the two-stage thruster. At the exit, the inflow boundary condition is specified such that the pressure is 2.5 Torr and the temperature 300 K.

As mentioned before in this chapter the measured values of plenum pressure and mass flow rate were used with Eqn. 4.1 to determine a stagnation temperature of roughly 500 K. This value of temperature was used at the inlet, along with 240 Torr for the pressure, to simulate the fluid flow through the nozzle using the simplified grid. Since microwave energy addition was not calculated here the heat transfer rate through the nozzle wall was not calculated either, and for the purposes of this simplified model it was assumed that the temperature in the plenum would be equal to the inlet temperature. Results from this calculation were compared with the LIF data in Fig. 6.3. The fluid code predicts that the mass flow rate into the thruster is 520 mg/sec, after steady state conditions are reached. The same criterion is used here to determine when steady state conditions are achieved as was used in Chapter 4. The computed mass flow rate value differs by about 9 % from the measured mass flow rate during the experiment, 570 mg/sec. The complete set of temperature contours generated from this simulation is shown in Fig. 6.6. For this calculation the numerical dissipation coefficients were chosen so that $\alpha_1 = 0.3$ and $\alpha_2 = 0.3$, slightly different than the values used for the validation cases in Chapter 3. It was found empirically that using the values from Chapter 3 for the compressible boundary layer test cases would result in small oscillations in

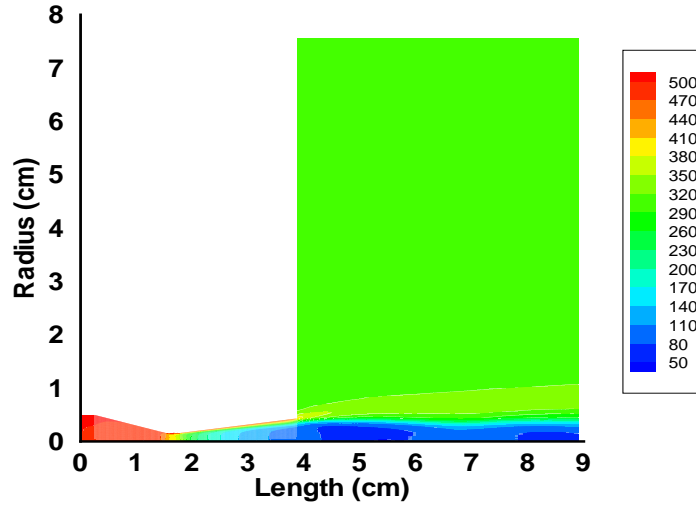


Figure 6.6: Temperature contours in the simplified geometry for the case of a 500 K plenum.

the flow properties, which were judged to be unphysical. The Reynolds number (Re_x) in this flow was computed in the same manner as in Chapter 4, and the maximum value of this quantity was found to be roughly 8×10^4 on the centerline near the exit of the expanding nozzle section. For this value of Reynolds number one would expect the boundary layer in the nozzle to be laminar [57]. The model used here should therefore be able to capture the boundary layer accurately. The temperature at the nozzle exit is roughly 75 K, and the flow is under expanded. One feature of the present simulation is the presence of a shock-diamond structure in the plume, which is clearly visible in Fig. 6.7. The Mach number increases to about 5.3 on the centerline about 2 cm away from the nozzle exit, and then decreases shortly after this point. Further downstream the Mach number increases again.

For the ideal situation in which there is no heat transfer to the thruster walls and 900 W of subsonic energy addition is added to an argon flow of 570 mg/sec the maximum temperature in the plenum would be about 3350 K and the plenum pressure would be 620 Torr. With these values of temperature and pressure at the inlet the fluid code predicts that the temperature where an LIF measurement was collected, about 4 mm above the centerline, is about 1200 K. Near the centerline the temperature is predicted to be 575 K. The fact that the measured temperature is much lower, at both locations, implies that a sizable fraction of the microwave input power is transferred to the walls of the thruster due to thermal conduc-

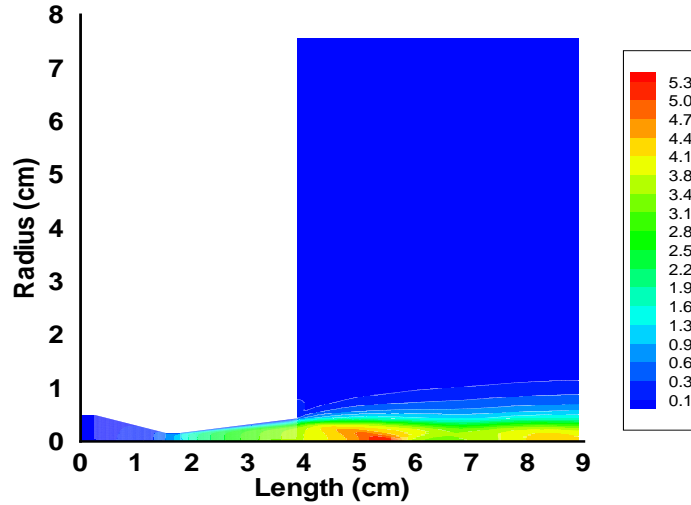


Figure 6.7: Mach number contours in the simplified geometry for the case of a 500 K plenum.

tion. This is also supported by the fact that the measured plenum pressure is only 240 Torr, instead of 620 Torr which would be indicative of the full 900 W being imparted to the flow. It is important to mention here that an alternative explanation to the above hypothesis of large heat transfer to the walls is that microwave power is not being absorbed into the plasma in the first place but rather is reflected back to the magnetron. This possibility would seem unlikely because the subsonic part of the two-stage thruster is based on a design that was empirically optimized for microwave coupling to the plasma [22].

6.2 Detailed Simulation of Two-Stage Thruster with Subsonic Energy Addition

While the previous simulation was well suited to study the temperature and velocity profiles at the exit of the thruster, a more detailed calculation was performed for the plenum section of the two-stage thruster with only subsonic energy addition, using the same code written to simulate the single-stage METs in Chapter 4. This calculation was meant to explore the plasma properties inside the plenum and the structure of the filament plasma described above. The code for the helium plasma kinetics was replaced with the appropriate model for argon, involving 15

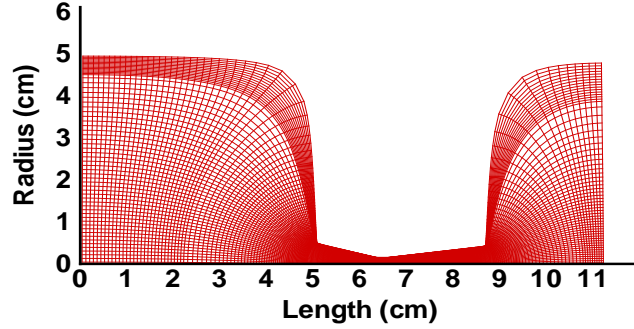


Figure 6.8: The structured grid generated for the two-stage thruster.

ionization and excitation processes as described in Chapter 3. The structured grid used for the detailed two-stage thruster simulation consisted of 61 radial cells and 190 axial cells, as shown in Figure 6.8. At the throat the radial distribution of cells is such that there are 16 cells within 0.1 mm of the nozzle wall. There is one difference between the actual two-stage thruster geometry and this numerical grid. The two-stage thruster has a straight throat section which is 1.25 cm long, whereas the throat section in the grid is only 1 mm. The throat length should not influence the calculated plenum conditions. The boundary conditions at the inlet for the two-stage thruster, concerning the mass injection scheme and the imposition of a constant wall temperature, are similar to those used for the thrusters in Chapter 4. The wall temperature in the plenum of the two-stage thruster was taken to be 500 K based on the measurements of plenum pressure and mass flow rate mentioned previously. A case with 500 W absorbed by the subsonic plasma was considered. The same convergence criterion was applied to this case as for all previous fluid simulations, and the relative error between the calculated fluxes and the prescribed quantities at the inlet was similar.

6.2.1 Simulation Results

The results of a simulation involving the subsonic stage of two-stage thruster with 500 W of energy addition are now presented, starting first with temperature and

electron temperature contours. Fig. 6.9 shows the gas temperature contours in degrees Kelvin. The temperature in the plenum is about 660 K, and the pressure is 290 Torr. Both of these quantities are relatively constant throughout the plenum section. The temperature varies by about 50 K. The calculated pressure is about 20 % higher than the measured plenum pressure, and the temperature is about 32 % higher than the stagnation temperature determined from Eqn. 4.1 and used in the earlier simulation in this chapter. It is important to point out here that in the current simulation it is assumed that 500 W is absorbed by the plasma, whereas the experimental conditions suggest that 900 W is absorbed. The contours of axial velocity and the re-circulation zone associated with the inlet region are qualitatively the same for the present case as in the MET examples studied in Chapter 4, and are omitted from further discussion for this reason. The electron temperature, however, is markedly different than for the helium discharge cases. The electron temperature contours are shown in Fig. 6.10. A maximum electron temperature of 13200 K occurs in a thin region adjacent to the back plate. This region is approximately five cells wide.

The contours of electron joule heating rate are shown in Fig. 6.11 and correlate well with the electron temperature contours. Most of the joule heating occurs in a thin region inside the plenum, adjacent to the left hand boundary. The electrons receive at most about 20 W/cm^3 of microwave power in this region. The peak electron number density in the discharge region is about $5 \times 10^{12} \text{ cm}^{-3}$, which occurs near the top left corner of the plenum. This point happens to coincide with a maximum in the radial electric field. The peak value of electron number density for the current case with argon is an order of magnitude larger than that encountered for the helium case studied in Chapter 4 at the same microwave frequency (2.45 GHz) with a similar geometry. This fact leads to the drastic difference in electric field pattern between the helium and argon cases studied in this thesis. The peak electron number density in the current case, $5 \times 10^{12} \text{ cm}^{-3}$, corresponds to an ionization fraction of roughly 10^{-6} . Away from the top left corner the electron number density drops to about 10^{11} cm^{-3} about 3 cm into the plenum, as shown in Fig. 6.12. Such a high electron density effectively makes it impossible for the microwave field to propagate any significant distance inside the plenum chamber. In this sense the argon plasma strongly perturbs the electric field pattern, as mentioned in Chapter 2, far beyond the ideal structure of a TM_{011} mode.

The densities of the $4s[3/2]_2$ and $4s'[1/2]_0$ argon metastable levels are relatively localized in the thin region described above, as shown in Fig. 6.14 and Fig. 6.13, respectively. The peak number densities of these species in this region are 7.7×10^{13} and $8.4 \times 10^{12} \text{ cm}^{-3}$, in that order. The number density of ground state argon atoms in the thin discharge region, for this case of 500 W microwave energy addition in the plenum, is approximately $4.3 \times 10^{18} \text{ cm}^{-3}$. The number densities that the metastable species would have if a Boltzmann equilibrium was maintained with

$T_e = 13200$ K turn out to be $8.5 \times 10^{14} \text{cm}^{-3}$ for $4s[3/2]_2$ and $1.5 \times 10^{14} \text{cm}^{-3}$ for $4s'[1/2]_0$. The calculated values from the simulation are about an order of magnitude less than the Boltzmann equilibrium values. The metastable number densities according to the calculation are reduced at the entrance of the converging nozzle to become $4 \times 10^{13} \text{cm}^{-3}$ for $4s[3/2]_2$ and $4.5 \times 10^{12} \text{cm}^{-3}$ for $4s'[1/2]_0$. For the value of electron temperature in this location, approximately 6800 K, these species would be $6 \times 10^{10} \text{cm}^{-3}$ and $9 \times 10^9 \text{cm}^{-3}$ respectively if a Boltzmann equilibrium were maintained among the excited species.

A principal result from this section is that the model predicts that the joule heating occurs predominately in a thin discharge region near the left hand boundary of the plenum, and that the electric field pattern is highly distorted because of this. This behavior is suggestive of the filament discharge observed during the operation of the actual thruster. However, for the real thruster the filament discharge occurs on the centerline, and the model predicts that such a discharge should form adjacent to the back plate. The model includes the most dominant volumetric recombination process, dissociative recombination, under the present conditions of neutral atom number density and electron temperature as was established in Chapter 3. One possible reason for the difference between observation and model prediction is that the model does not consider wall effects including electrostatic sheaths and recombination at the wall, and these effects may prevent the filament from forming near the back plate as predicted by the simulation. In a thin region immediately adjacent to the back plate electron loss due to recombination at the wall should be the dominant loss mechanism. If such an effect were included in the model it is possible that the filament would still appear and would be offset from the back plate by a certain amount. This issue could be resolved in future work.

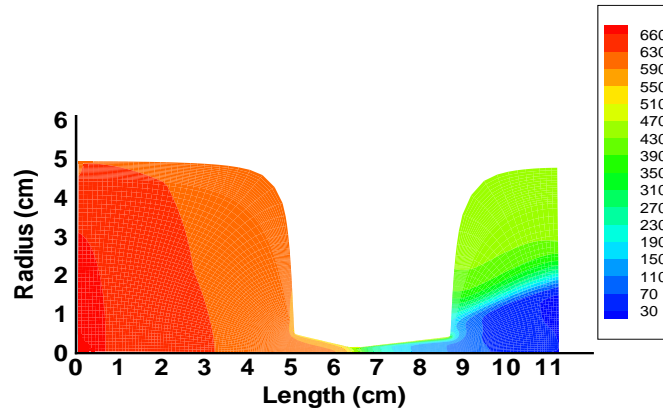


Figure 6.9: Temperature contours inside the two-stage thruster (in K).

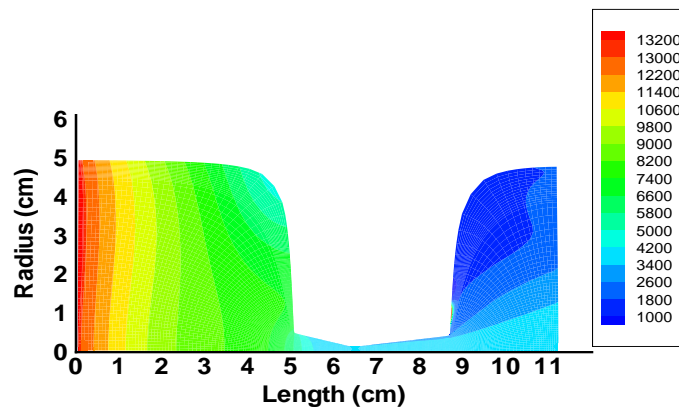


Figure 6.10: Electron temperature contours inside the two-stage thruster (in K).

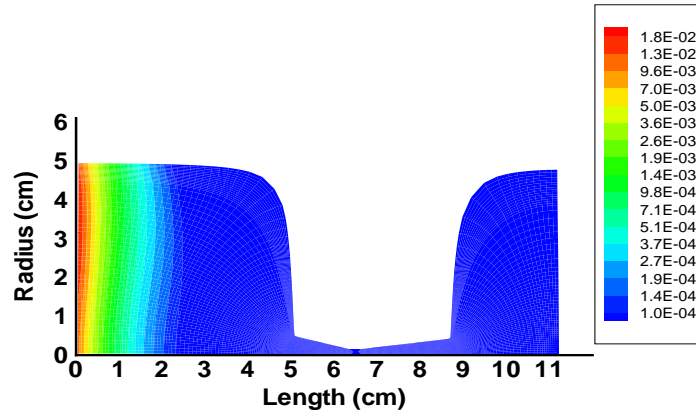


Figure 6.11: Joule heating rate of electrons inside the two-stage thruster (in kW/cm^3).

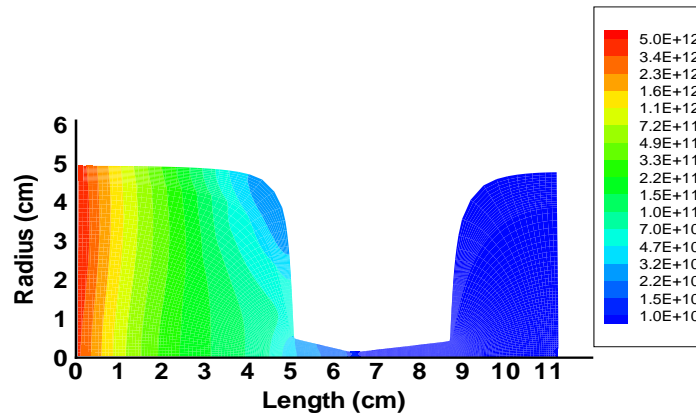


Figure 6.12: Electron number density contours inside the two-stage thruster (in cm^{-3}).

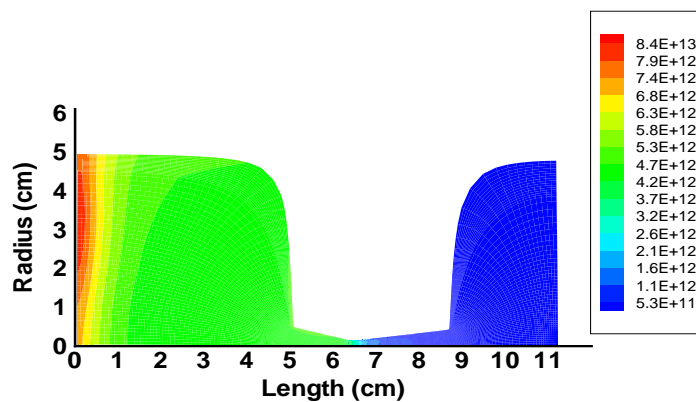


Figure 6.13: $4s'[1/2]_0$ number density contours inside the two-stage thruster (in cm^{-3}).

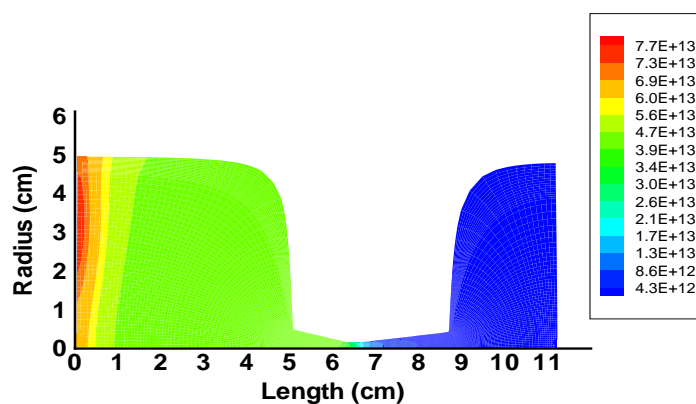


Figure 6.14: $4s[3/2]_2$ number density contours inside the two-stage thruster (in cm^{-3}).

6.3 Two-Stage Thruster with Supersonic Energy Addition

LIF experiments were done with the two-stage thruster, involving both subsonic and supersonic energy addition. This work represents the culminating effort of this thesis and the findings are now presented. For measurements with the supersonic stage the subsonic stage of the thruster was operated in exactly the same manner as before, with a mass flow rate of about 570 mg/sec and a plenum pressure of 240 Torr. About 80 W of power was added in the supersonic stage of the thruster for these experiments. This value of absorbed power was inferred from measurements of forward and reflected power, using the microwave circuit shown in Fig. 2.6. The appearance of the plume with the supersonic stage operating is described briefly, and the measured values of temperature in the plume for this case are presented. After this the details of the fluid simulation involving supersonic energy addition are discussed and the complete temperature contours from this calculation are presented.

Before the supersonic stage was activated the discharge in the subsonic stage was initiated. Without the subsonic discharge present in the thruster it was not possible to breakdown the gas in the supersonic stage. In other words it was found empirically that the supersonic stage does not work without the pre-ionization that takes place in the subsonic stage. For the experiments with supersonic energy addition the subsonic stage was run exactly as before, and no attempt was made to optimize the operating parameters of the subsonic stage to achieve better microwave coupling into the supersonic stage. Much effort was made, however, to tune the microwave circuit for the supersonic stage. This was done entirely by trial and error, adjusting the length of insertion of the tuning stubs into the waveguide. It was found that only two of the three stubs needed to be adjusted for this purpose. As adjustments were made the intensity of the plume would increase or decrease. Even at a condition far from the optimum the plume appeared different than in the case with no supersonic energy addition. As the optimum tuning condition was approached the measured reflected power dropped off sharply and the light intensity of the plume increased significantly. It was a bright red plume which extended about 10 cm from the exit of the nozzle, clearly visible. The plume appeared much wider than in the previous case with no supersonic energy addition, as though the original plume were surrounded by a red halo.

6.3.1 LIF Measurements

LIF temperature measurements were made when the thruster was operating with 80 W of supersonic energy addition. These measurements were made in the same location, about 7 mm in front of the nozzle exit, as the measurements in the pre-

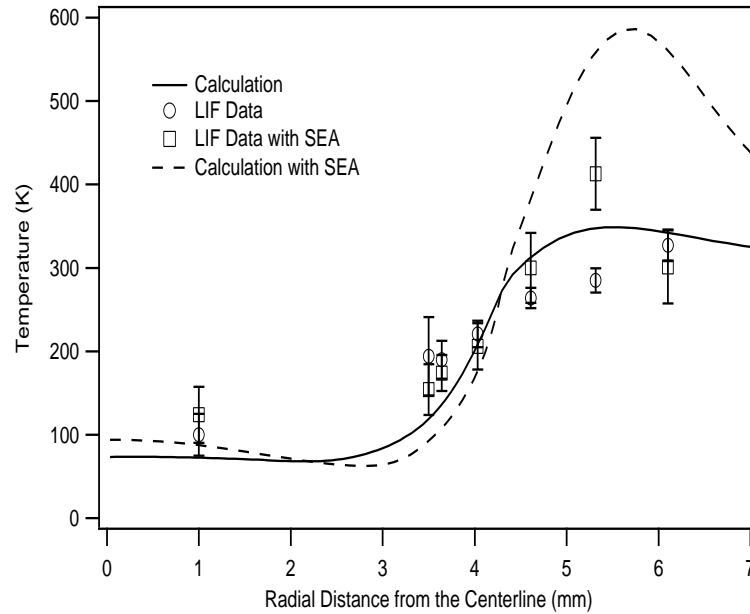


Figure 6.15: Measured temperature in the exhaust plume of the two-stage thruster with and without supersonic energy addition (SEA). The lines indicate the result from a fluid simulation for each case.

vious section. The results are shown in Fig. 6.15 together with the previously collected data for the case without supersonic energy addition. A temperature of 210 ± 30 K is measured 4 mm from the centerline, and this value is the same to within experimental error as the measurement made for the case without supersonic energy addition. The measured temperature increases to 410 ± 40 K at a distance of 5.3 mm away from the centerline, and then decreases again back to the level associated with no supersonic energy addition as one moves out 6 mm away from the centerline. The peak temperature at 5.3 mm is less than the value predicted by the code, 550 K, by about 33 %. Experimental measurements may suggest that the temperature in the plume decreases at 3.5 mm, relative to the case with no supersonic energy addition, as shown in Fig. 6.15. The measured value of temperature here is 150 ± 30 K, whereas in the previous case with no supersonic energy addition it was 190 ± 50 K. This temperature difference is comparable to the magnitude of the error bar, and so it is hard to make a firm conclusion. The numerical simulation, however, predicts a temperature decrease at this point from about 130 K to 100 K when supersonic energy is added. The temperature decrease in this location is due to the fact that energy addition in the boundary layer gives rise to a stronger expansion region outside the thruster. In both cases, with and without energy addition, the code under predicts the measurement, by 37 %. The LIF

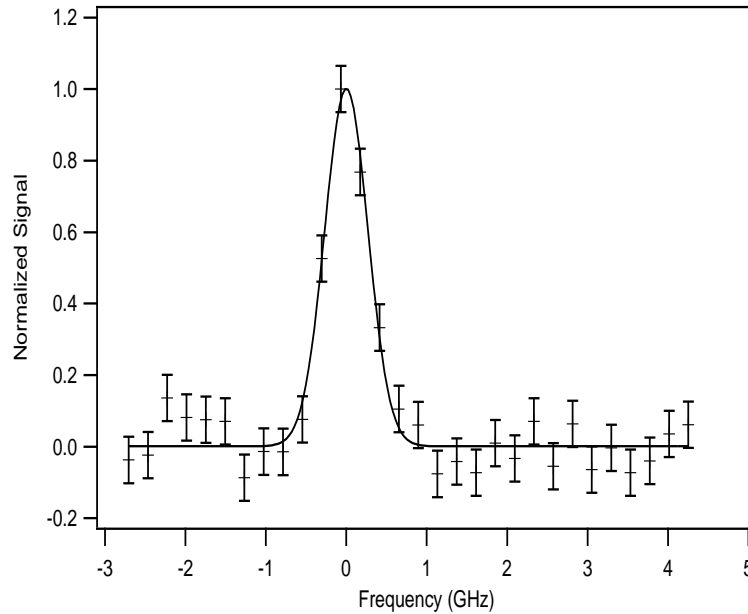


Figure 6.16: LIF data used to determine the temperature 4 mm above the plume axis for the case of supersonic energy addition.

signal corresponding to the 4 mm point taken with supersonic energy addition is shown in Fig. 6.16. Since the measured temperature at this point with and without supersonic energy addition is roughly the same there is no perceptible difference between the full-width-at-half-maximum (FWHM) in Fig. 6.16 and in Fig. 6.3. The fact that the measured temperature at this point is the same, to within the error bar, both with and without supersonic energy addition is corroborated by the results from the fluid simulation as presented in Fig. 6.15. Error bars were generated as before from the standard deviation of the background noise, and a Gaussian curve was fit to the normalized signal. The characteristics of Fig. 6.16 represent the other data points taken for case of the supersonic energy addition as shown in Fig. 6.15. The error bars tend to be larger for the case of supersonic energy addition. Most likely this is due to the presence of additional noise at 218 Hz, the laser modulation frequency, produced by the second magnetron used to power the supersonic stage. No effort was made to verify this hypothesis, or to take steps to reduce the overall noise level in the LIF signal.

As with the case of no supersonic energy addition a velocity measurement was made near the centerline for the current case as well. In order to measure the axial component of velocity it was necessary to direct the laser beam parallel to the plume centerline. The same arrangement was used for this purpose, as for the previous velocity measurement where the beam was focused 7 mm from the

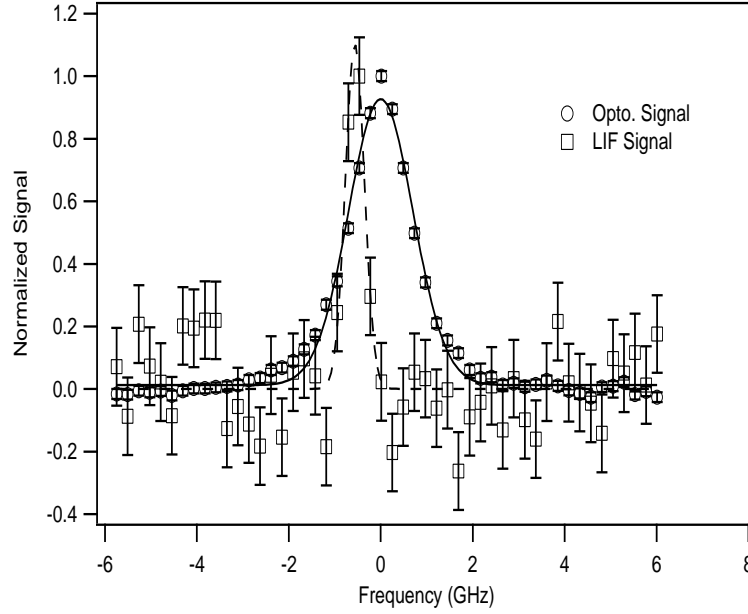


Figure 6.17: LIF data used to determine the axial velocity 1 mm away from the plume centerline for the case of supersonic energy addition.

thruster exit about 1 mm away from the plume centerline. In fact measurements of flow velocity with and without the supersonic stage were made sequentially. Fig. 6.17 shows the LIF signal measured for the supersonic energy addition case together with the signal from the optogalvanic cell. The velocity was measured to be 440 ± 20 m/sec and the corresponding temperature value was 120 ± 30 K. This temperature value is plotted together with the other radial measurements of temperature in Fig. 6.15. Without supersonic energy addition the axial velocity in this location is higher, 500 ± 30 m/sec. The numerical model does predict a velocity decrease from 670 to 660 m/sec when supersonic energy is added. However, in both cases the computation over predicts the velocity by as much as 50 % (for the supersonic energy addition case). One possible explanation for the over prediction of the velocity is the influence of the turbulent shear layer on the expanding free jet which is not included in the model. The presence of such a turbulent free layer may limit the expansion of the free jet thus accounting for the lower velocities that were measured in the experiment.

6.3.2 Comparison with Fluid Simulation

The details of the fluid simulation performed for the case of 80 W supersonic energy addition and used to compare with the LIF data in Fig. 6.15 are now discussed.

Unlike the previous simulation with the simplified grid for the case of no supersonic energy addition, in this simulation the microwave field components in the supersonic stage are determined, and the argon plasma kinetics model from Chapter 3 is used to predict the number densities of electrons and excited state species. All other aspects of the calculation involving the conditions at the subsonic inlet, the plenum wall temperature and the numerical dissipation coefficients are the same as discussed in the first section of this chapter. The numerical grid for this calculation was the same as the one presented in Fig. 6.5 with the same number of grid points.

The temperature contours corresponding to the plume profile for supersonic energy addition presented in Fig. 6.15 are shown in Fig. 6.19. The striking result here is that most of the temperature increase that one would expect from the energy addition occurs in the boundary layer of the expanding flow. The temperature near the nozzle wall approaches a maximum value of 3040 K. In the real thruster the expanding nozzle section is made from alumina ceramic, which could possibly sustain such high temperatures momentarily. More likely there is some heat transfer occurring through the ceramic wall, which is ignored in this simulation. Adiabatic conditions were assumed at the nozzle wall in the calculation to represent the ideal case where all the supersonic energy addition was imparted to the flow. Another feature to note in Fig. 6.19 is the region of elevated temperature which surrounds the plume, like a donut, about half a centimeter away from the centerline. This donut region could correspond to the luminous red halo observed during operation of the supersonic stage, described previously. Including heat transfer through the diverging nozzle wall in the model would lower the peak temperature in this region and bring the predicted temperature peak in Fig. 6.15 closer to the measured value.

With supersonic energy addition the temperature at the nozzle exit increases by about 14 degrees Kelvin and the Mach number decreases from 3.7 to 3.2. The Mach number contours are shown in Fig. 6.18. The flow is under expanded at the exit and continues to expand after leaving the nozzle just as in the case with no energy addition, producing a shock-diamond pattern. The point of maximum Mach number occurs a little more than 2 cm downstream of the nozzle exit. The Mach number on the centerline at this point is 7.6, which is higher than for the case with no energy addition.

The joule heating rate inside the nozzle in the supersonic stage is shown in Fig. 6.20. The region of significant electron heating is fairly well confined to the nozzle wall and exit plane. At these locations the electrons receive a peak power of about 20 kW/cm^3 from the microwave field, a peak value that is much higher than any other heating rate discussed in this thesis. This behavior resembles the argon filament predicted by the full code to exist near the back plate in the subsonic stage, as discussed earlier in this chapter. The heating region here is about

eight cells in width and appears to be particularly intense at the corners, near the throat and the exit. The electron number density which corresponds to this heating rate is shown in Fig. 6.21. A maximum electron number density of $3.8 \times 10^{15} \text{ cm}^{-3}$ occurs at the nozzle wall near the throat. The ground state number density in this location is $7.6 \times 10^{17} \text{ cm}^{-3}$, making the ionization fraction about 0.5 %. With such a high value of electron number density the electric field is almost completely excluded from inside the nozzle. The peak electron temperature in this thin heating region is approximately 15000 K. For this value of electron temperature and the value of ground state number density just given the electron number density would be $3 \times 10^{17} \text{ cm}^{-3}$ if an equilibrium were maintained between the electron impact ionization rate from the ground state and three body recombination rate according to the Saha formula. The value predicted by the numerical model is approximately two orders of magnitude smaller than the equilibrium value from the Saha formula.

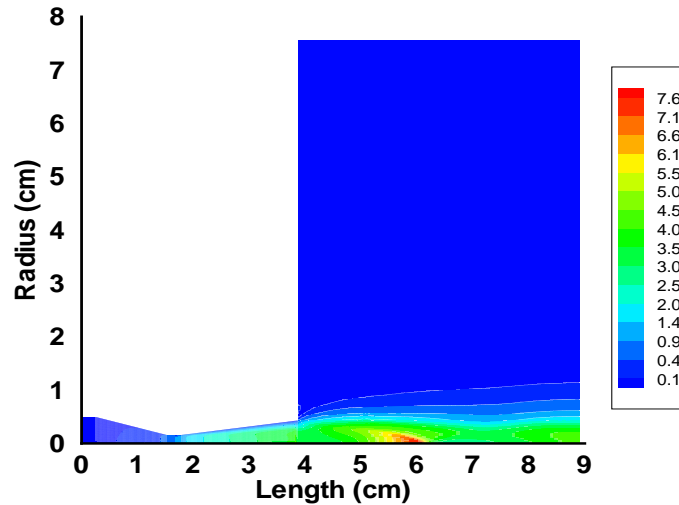


Figure 6.18: Mach number contours for the case of 80 W supersonic energy addition. The nozzle exit is at approximately 4 cm.

6.4 Conclusions from LIF Measurements and Model Predictions

The LIF measurements of temperature and velocity presented in this chapter lead to several conclusions about the characteristics of the two-stage thruster, with and without energy addition. Some of these conclusions are further corroborated by the results from numerical simulations involving a simplified model that treats the supersonic stage of the thruster separately from the plenum section. In addition several conclusions can be reached concerning the plenum section of the thruster based on a separate numerical simulation done for this part as well, similar to the simulations performed in Chapter 4.

Without supersonic energy addition LIF temperature measurements indicate that the temperature in the subsonic stage is not as high as originally envisioned, for the ideal case where there is negligible heat transfer through the plenum wall. The temperature in the plenum can be inferred to be roughly 500 K, without even considering the LIF measurements, using Eqn. 4.1 with the measured values of mass flow rate and plenum pressure. If the full 900 W were imparted to the flow the temperature in the plenum and the resulting temperature profile in the plume would be much higher. The LIF measurements in Fig. 6.1 show conclusively that this is not the case. The measured value of 100 ± 30 K near the centerline in the

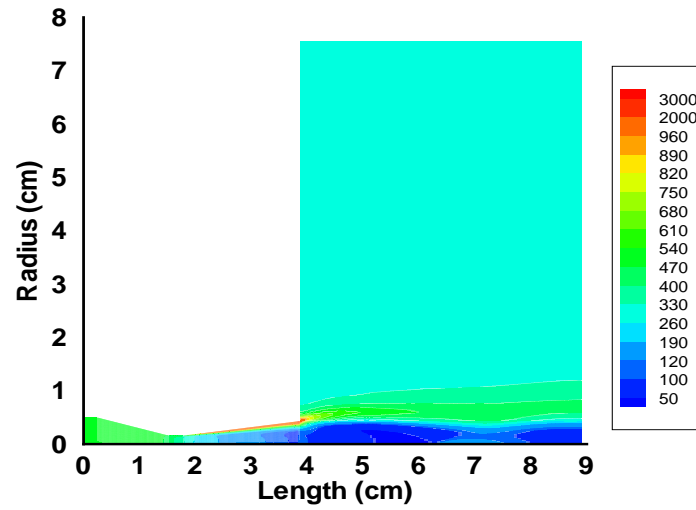


Figure 6.19: Temperature contours for the case of 80 W supersonic energy addition.

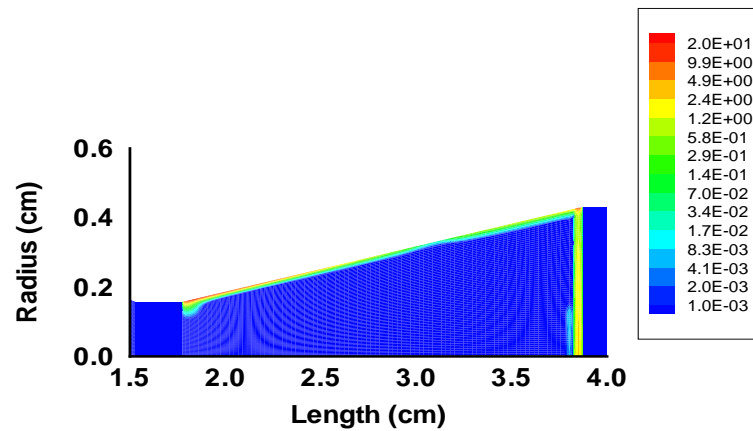


Figure 6.20: Joule heating contours for the case of 80 W supersonic energy addition (in kW/cm^3)

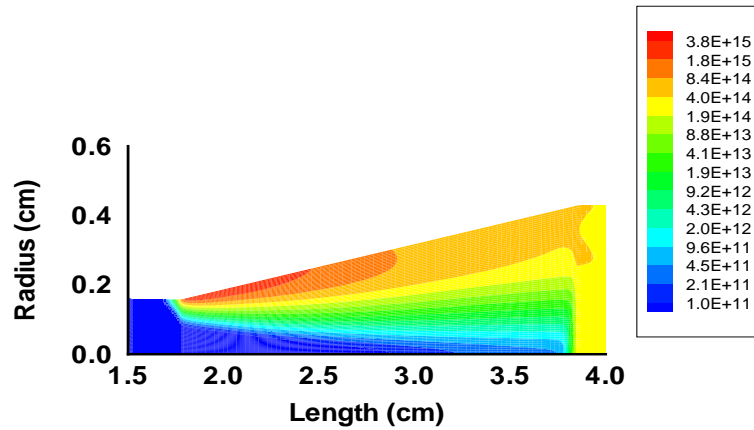


Figure 6.21: Electron number density contours for the case of 80 W supersonic energy addition (in cm^{-3}).

plume is consistent with the results of a fluid simulation starting from a 500 K plenum, and this suggests that a sizable fraction of the absorbed microwave power is transferred to the plenum wall due to thermal conduction.

For the case of 80 W supersonic energy addition LIF temperature measurements in the plume suggest that the core of the flow is relatively unaffected, with most of the supersonic energy addition being deposited in the boundary layer of the expanding flow. When shown together in Fig. 6.15 there is hardly any difference in temperature between the case where there is supersonic energy addition and the case where there is no supersonic energy addition. The only difference occurs at a radial distance of 5.2 mm from the plume centerline where there is an increase in temperature of about 150 K for the supersonic energy addition case. This temperature increase is captured by the numerical model of the supersonic stage as shown in Fig. 6.19. The simulation shows a region of elevated temperature that surrounds the plume, like a donut. This region may correspond to a luminous red halo that is observed experimentally during operation of the supersonic stage. The simulation further corroborates that most of the supersonic energy addition that gives rise this red halo region occurs inside the boundary layer of the expanding flow.

With regards to the plasma properties in the subsonic stage of the thruster, a numerical simulation was performed to explore this issue, as was done the single-

stage METs in Chapter 4. The simulation predicts that the joule heating occurs predominately in a thin discharge region near the left hand boundary of the plenum as shown in Fig. 6.11. The peak value of electron number density in this region is larger than that encountered for the helium cases studied in Chapter 4, and unlike the helium cases the electron number density here is well localized. With such a high electron number density as that predicted, $5 \times 10^{12} \text{cm}^{-3}$, the electric field does not penetrate a significant distance inside the plenum chamber. This high value of electron number density accounts for the differences between the helium and argon cases. The intense region of high electron number density, predicted by the simulation, is suggestive of the filament discharge observed during the operation of the actual thruster. For the real thruster, though, the filament discharge occurs on the centerline. The absence of wall effects including sheaths and recombination at the wall may have an effect on the location and properties of the filament, and this issue should be resolved in future work.

Chapter 7

Conclusions

As part of this thesis a novel two-stage microwave thruster was built and supersonic energy addition in a microwave thruster was demonstrated for the first time. It was verified experimentally that microwave energy could be added to an expanding supersonic flow in a thruster geometry. The further optimization of this energy addition by concentrating it in the core of the flow rather than in the boundary layer was not the goal of this thesis and is left for future work. LIF measurements of temperature and velocity were performed in the exhaust plume of this thruster in an attempt to characterize the nature of the physical processes occurring inside the thruster. A sophisticated numerical model was developed and applied to each stage of the thruster separately, so that a description of the microwave-sustained discharge inside each stage could be obtained. The model in this thesis includes the interaction among the three principal physical elements of the problem, the microwave field, the fluid dynamics and the plasma kinetics, and was used to study not only the two-stage thruster, but also the standard microwave thruster as well.

LIF measurements were instrumental in revealing that much lower than expected gas temperatures are present in the plume, suggesting that heat transfer to the thruster walls is much more significant than originally thought. The temperature near the centerline in the plume was measured to be 100 ± 30 K without supersonic energy addition, and this value changes slightly, by about as much as the error bar, when 80 W of microwave energy is added in the supersonic stage. The axial velocity was measured using the LIF technique as well, and it was shown that there is a decrease in velocity when supersonic energy is added, from 500 ± 30 m/sec to 440 ± 20 m/sec, a 12 % decrease.

A numerical simulation of the supersonic stage suggests that most of the energy addition is deposited in the laminar boundary layer, and this is supported by the LIF temperature measurements. The numerical model does predict a velocity decrease with supersonic energy addition, but the predicted velocity value both with and without supersonic energy is higher than the measured value. One

possible explanation for the difference between theory and experiment is that the turbulent shear layer, present in the real expanding free jet, is not included in the model.

Additional future work could be done to alleviate some of the shortcomings associated with the LIF measurements of temperature and velocity in this thesis. The ability to measure both components of velocity and do a complete scan through the plume, as done by Keefer *et al.* [61], was not achieved in this thesis. Another limitation was the fact that with the current laser system frequency scans could be accomplished only in 240 MHz increments. As a result for the low temperatures observed in thesis only a few points were present in the Gaussian peak. The ability to do a continuous scan in frequency would make it possible to obtain many points inside the Gaussian peak, and this would improve the accuracy of the velocity measurements as well.

There are several critical assumptions inherent in the plasma model. These assumptions are now summarized and the arguments made within this thesis to validate them are reviewed briefly. First the electron energy distribution function (EEDF) is assumed to be Maxwellian. It was shown in Chapter 3 that this is a good assumption for argon plasmas under the conditions considered here, as outlined in Table 3.1. For helium plasmas it was shown that the true EEDF is not Maxwellian, but the error in the calculated ionization and excitation rates by assuming a Maxwellian EEDF is probably no greater than an order of magnitude. This conclusion was reached after it was demonstrated that small changes in the level of applied electric field have a significant effect (by several orders of magnitude) on the tail of the EEDF as shown in Fig. 3.5. Under the conditions of interest in this thesis the dominant ionic species in the plenum of the microwave thruster is the molecular ion. This was shown to be the case for both helium and argon by calculating the ratio of molecular to atomic ions, assuming a thermodynamic equilibrium exists between them. The dominant volumetric electron loss mechanism in the plenum for both helium and argon is dissociative recombination. This was shown to be the case for helium in Fig. 3.4, where different electron loss processes were calculated including other processes which might be significant such as photo-recombination, three-body recombination and ambipolar diffusion. The corresponding case for argon was shown in Fig. 3.3. In the supersonic expansion section of the thruster convection is the dominant loss mechanism.

Now that some of the assumptions inherent in the plasma model have been reviewed some of the main results from the model, as applied to single-stage helium thrusters, are discussed. For both the 1 kW and the 100 W METs the numerical model of Chapter 3 portrays a physical picture that is markedly different than that one from a previous equilibrium model [15]. There are no large temperature gradients in the plenum, with the temperature being relatively flat and close in magnitude to the prescribed plenum wall temperature. The electron tem-

perature is an order of magnitude higher than the gas temperature, even at atmospheric pressure. In addition, for both the 1 kW and the 100 W METs, the electron number density is relatively flat throughout the plenum. This is true even though most of the electrons are produced in a confined region near the centerline, and the flow residence time in the plenum is high. The number density of each of the metastable species, however, varies significantly despite the fact that the electron number density is flat. The observed light emission on the centerline during experiments with 1 kW helium METs [9, 12] seems to correlate well with the distribution of metastable states calculated by the model in this thesis, as shown in Fig. 4.12 and Fig. 4.13. Whether or not the experimentally observed radiation pattern is the result of line emission from transitions involving the metastable states or whether it is from transitions involving ionic states can be answered by future spectroscopic measurements. In addition the radial profile of electron temperature predicted here for the 1 kW MET compares well with the profile measured experimentally by Balaam, as illustrated in Fig. 4.16. Finally given a rough estimate for the stagnation temperature the current model does succeed in predicting the specific impulse for 1 kW MET to within 20 %. Although the experimental thrust data for this thruster [9] suggests that there are gradients in temperature in the plenum as discussed in Chapter 4 and these are not predicted by the current model.

The subsonic stage of the two-stage microwave thruster, running on argon, was also studied using the model developed in this thesis, using the appropriate ionization and excitation processes for argon as outlined in Table 3.3. A compact filament discharge was observed in the plenum under these conditions. Such a discharge was predicted to form by the numerical model, albeit the model predicts that it would form by the back plate of the thruster, not on the centerline as observed. The inclusion of flow swirl by adding an azimuthal momentum equation to the fluid model may help to correct this discrepancy in future work. The addition of wall effects, such as electrostatic sheaths and recombination at the wall may alter the present results as well, since the filament was predicted to form in a thin region immediately adjacent to the back plate.

More work could be done to improve the current model so that it is better able to predict the steady state mass flux and plenum pressure for the 100 W MET in Chapter 4. Lowering the level of numerical dissipation and refining the grid could make an improvement. As far as numerical dissipation is concerned, numerical dissipation schemes other than the flux-limited scalar dissipation, used in this thesis, may ultimately lead to better results [36]. Adding an azimuthal velocity component to the model, which is present in the real MET, may enable the model to capture gradients in temperature and pressure in the plenum if significant gradients do in fact exist. Finding a new way to estimate the plenum wall temperature may also enable the current model to better predict the plenum pressure and the specific impulse for the single-stage thrusters. A direct measurement of the

plenum wall temperature would help in this regard.

In this thesis the numerical model has produced several interesting results that deserve further experimental investigation. The central issue here is to be able to corroborate the predicted electron number density profile inside the MET, which is surprisingly flat for both helium and argon plasmas. One possible diagnostic which could accomplish this measurement inside the microwave cavity, without altering the electric field pattern there, is Thomson scattering [62]. This laser diagnostic technique has the added benefit of enabling a simultaneous measurement of electron temperature as well, without assuming the existence of a Boltzmann equilibrium as required for certain kinds of spectroscopic techniques.

A high performance MET with a specific impulse greater than 400 sec has yet to be demonstrated conclusively. As part of this study it has become clear that heat transfer to the thruster walls is a significant process that must be included in any modeling effort. One way to lessen the wall heat transfer rate in the standard MET would be to build it in a similar fashion as the arcjet, with thin walls made from rare-earth metals able to sustain much higher temperatures. Another way would be to coat the aluminum walls of the plenum chamber with a ceramic material, such as alumina, which was used effectively for the supersonic stage in this thesis. Although improvements in the standard MET design would likely achieve higher specific impulse performance, as discussed in Appendix B at least 1500 sec is required for orbit-raising maneuvers. With hydrogen the required specific impulse could possibly be achieved, but doing so with a more easily storable propellant, such as water, would be impossible with a standard MET alone. Supersonic energy addition may prove to be the way to overcome this hurdle. Whether such performance is ultimately achievable or not has yet to be answered completely, and stands as the goal for microwave thruster research.

Appendix A

Overview of Electric Propulsion

Electric propulsion is a class of spacecraft propulsion systems that is characterized by values of specific impulse, between 600 sec and 10,000 sec or even higher, depending on the specific nature of the acceleration mechanism. A number of electric propulsion devices have been studied for over forty years [4,63–65]. Among the various kinds of electric propulsion devices, ion engines, Hall thrusters, and arcjets are routinely used in space. Each of these three systems will be described in more detail later, highlighting the application and the future direction of development in each case. Another electric propulsion system is the magnetoplasmadynamic (MPD) thruster, which utilizes a magnetic body force to accelerate a current-conducting fluid, and has been studied extensively for many years [66,67]. The MPD thruster, running on an alkali metal propellant such as lithium, could be promising for many future space missions, since studies have suggested that alkali metal propellants could mitigate the erosion of the thruster electrodes [68]. The gas-fed pulsed plasma thruster (GF-PPT) is one more example of a research device, in which a propagating current sheet, propelled by magnetic pressure, accelerates a propellant mass. GF-PPTs have been considered for a variety of missions, from attitude control to primary propulsion, but to date have demonstrated relatively low efficiencies, no greater than 30 % [69]. A related concept which has been flown in space is the ablative pulsed plasma thruster (APPT), in which a solid propellant such as teflon is utilized to form the current sheet [70]. Like the MPD thruster, the microwave thruster is exclusively a research device, for which more work needs to be done to understand the fundamental processes involved and to improve the long term reliability and performance of the device.

Central to the successful operation of any electric propulsion device is the availability of space-based electric power sources. Solar cell and battery technology, which powers the current generation of electric propulsion systems, is reviewed, and prospects for further improvements are discussed. In the future nuclear reactors could be used to power electric propulsion systems in space. The current status of this technology is discussed in the last part of this appendix.

A.1 Arcjet

An arcjet is an electrothermal thruster, where an electric arc heats a propellant gas to high temperature, and this high temperature gas then expands through a nozzle to produce thrust. Among electric propulsion systems, the arcjet is the most similar to the microwave thruster in the sense that in both devices the principle acceleration mechanism involves electrically heating a gas. The arcjet has been studied for more than forty years [71], and in the standard configuration it consists of two electrodes, a cathode and anode, which are both made from thoriated-tungsten [72]. The anode is concentric with respect to the cathode, and forms a nozzle. During normal operation an electric arc extends from the tip of the cathode through an elongated throat, or constrictor, and attaches along the diverging nozzle surface of the anode. Propellant gas is injected into the device upstream of the constrictor, through a series of orifices in the electrode insulator.

Arcjets used on spacecraft are radiation-cooled, and in practice have been made to run on storable space propellants such as hydrazine and ammonia. Because of the thermal nature of the device, the specific impulse of the arcjet depends on the average temperature in the constrictor and inversely on the molecular weight of the propellant. For this reason, it is advantageous to use low molecular weight propellants. A state-of-the-art, 1.8 kW hydrazine arcjet has demonstrated a specific impulse of roughly 600 sec, an efficiency of 30 % and a thrust of 180 mN during a 550-h test [73]. This kind of system has been used during the past ten years by Lockheed Martin on many of its A2100 geo-stationary satellites for north-south station-keeping (NSSK) [74]. A 30 kW ammonia arcjet demonstrated a specific impulse of 790 sec, an efficiency of 27 % and a thrust of about 2 N, during a recent test in space as part of the Air Force ESEX experiment [75]. Research arcjets have demonstrated even higher values of specific impulse, more than 2000 sec, at around 30% efficiency, with several Newtons of thrust and several hundred kilowatts input power, using hydrogen as the propellant [20,72].

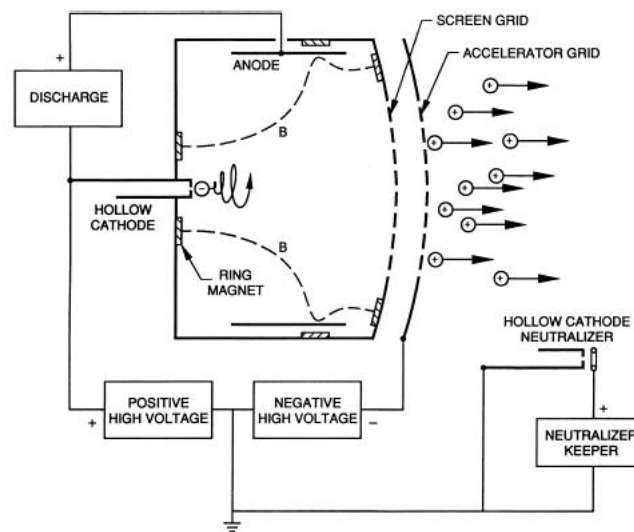
Two-dimensional, axisymmetric, numerical models have been developed to study the arcjet thruster, that include the effects of separate electron and heavy particle temperatures and non-equilibrium ionization [18,19]. These models are based the Navier-Stokes equations to describe the fluid properties inside the arcjet thruster and share many similarities with the model developed in this thesis for simulating the microwave thruster, described in Chapter 3. A key feature of the approach used in Ref. [18], is the inclusion of a sheath model for both electrodes, consisting of a simple algebraic equation for the voltage drop at each electrode, together with the sophisticated numerical treatment of the fluid flow and the electric field potential in the rest of the thruster. Specific impulse predictions, made using the complete model, for a 10 kW, radiation-cooled, hydrogen arcjet [20] were within 10% of the experimentally measured values, over a range of specific energies from 50 to 200 MJ/kg (0.005 to 0.02 kg/MJ) [18]. It is worthwhile to review

a few results from a typical arcjet simulation, since similar kind of behavior is expected in the microwave thruster. Numerical results for the hydrogen arcjet indicate a peak gas temperature of almost 30,000 K on the centerline in the constrictor region, just downstream of the cathode tip, with the electron temperature slightly higher at 42,000 K [18]. The temperature drops from these high values at the centerline to several thousand degrees, at the wall of the constrictor. Typically the constrictor region in an arcjet is at atmospheric pressure, and under this condition the flow is almost completely ionized on the centerline, at the high temperature point. In addition most of propellant mass flows around the high temperature core, and the high temperature core forms a fluid dynamic plug, which effectively decreases the throat area, increasing the stagnation pressure in the plenum and the thrust of the device. In experiments with microwave thrusters to date, it was hoped that a similar process was occurring, with the microwave-sustained plasma playing a role similar to that of the constricted arc.

A.2 Ion Engine

Within the last five years the focus has shifted from the development and use of arcjet technology to the development and flight qualification of ion engines and Hall thrusters, both of which have a higher specific impulse and in practical applications run on xenon. The ion engine consists of an ion source, an accelerating electrode, or pair of electrodes, which impart energy to the ions electrostatically, and a neutralizer, which balances the total charge in the exhaust beam. In the standard configuration, known as the Kaufman ion thruster [8, 64], the ions are produced by electron-bombardment of neutral atoms in a low pressure discharge chamber, as shown in Fig. A.1. Electrons are supplied from an electron-emitting cathode inside the chamber. The walls of the chamber are maintained at a large positive voltage, typically 1000 V, relative to the rest of the spacecraft. There are two electrode grids at the end of the chamber, as shown in Fig. A.1. The inner grid is kept at a few volts below the potential of the chamber walls, which draws ions out of the chamber. The outer grid is maintained at a large negative voltage, typically a few hundred volts, relative to the spacecraft. The ions are accelerated in the region between the two grids, through a potential difference, which is denoted as V in the equations that follow. The specific impulse is determined by this potential difference, and the charge to mass ratio, q/M , of the ion [8],

$$I_{sp} = \sqrt{\frac{2qV}{M}} \frac{1}{g_0}. \quad (\text{A.1})$$



The maximum current density, j , which can be drawn through the acceleration grid of the thruster is a function of V as well [8],

$$\frac{T}{A} = \frac{8\epsilon}{9} \left(\frac{V}{d} \right)^2. \quad (\text{A.3})$$

Much of the initial research with ion engines was done with mercury and cesium ions. This technology was developed to the point where a 150 kW mercury ion thruster, 1.5 m in diameter, was tested by NASA in 1968 with a specific impulse of 8150 sec, an efficiency of 70 % and a thrust level of 2.6 N [76]. Today xenon is used exclusively for commercial space missions. Boeing uses a xenon ion propulsion system (XIPS) on its 601HP and 702 geo-stationary satellites, of which

more than twenty are now in space or awaiting launch [74]. On the 601HP satellite model, 13 cm diameter ion engines are used for the NSSK mission. These devices have a specific impulse of 2600 sec and use 500 W of power delivering about 18 mN of thrust at 50 % efficiency [74]. The 702 satellite series has both 13 cm and 25 cm ion engines. The 25 cm ion engine has a specific impulse of 3800 sec and uses 4.2 kW of power while providing 165 mN of thrust at about 70 % efficiency [74]. These larger engines are used for the orbit-raising mission, which involves the final orbit insertion into geo-stationary orbit, from an elliptical transfer orbit. About two years ago such a maneuver was done for the first time, marking an important milestone for the electric propulsion community [77]. NASA has successfully used a similar, 30 cm ion engine, also built by Boeing, as the primary propulsion system on one of its latest deep space exploration missions [78]. The efficiency of this 30 cm engine is 61 % at 1.9 kW input power and it has a specific impulse of 3100 sec, while delivering about 80 mN of thrust [78]. A next generation 50 cm ion engine is currently being developed by NASA that would use krypton propellant and have a specific impulse of 14,000 sec, at 30 kW of input power [79]. This system could be used on future nuclear-powered space probes, traveling to the outer planets and interstellar space.

A.3 Hall Thruster

Another electric propulsion system that has matured to flight status is the Hall thruster, or closed-drift thruster, which utilizes an electrostatic force to accelerate ions, like the ion engine. But unlike an ion engine, which has electrode grids, the axial accelerating field in the Hall thruster is established by the interaction of an azimuthal electron current with a radial magnetic field. The standard Hall thruster configuration consists of an annular anode, two magnetic coils, and a neutralizer as shown in Fig. A.2. The two magnetic coils are concentric with each other, and the anode is in between them, such that a radial magnetic field exists in the annular region in front of the anode, as shown in Fig. A.2. Like the ion engine, xenon is commonly used as the propellant. Two variants of the Hall thruster exist, differentiated by the extent of the anode sheath region, the Hall current thruster and the anode layer thruster [80]. The Hall current thruster has a long annular channel, with dielectric walls, and most of the ion acceleration takes place in the quasi-neutral plasma region. The anode layer thruster, by contrast, consists of a shorter annular channel, with metallic walls, and the ion acceleration occurs predominantly in the anode sheath region (non-quasi-neutral plasma region). According to a theory developed by Kaufman [80, 81], which models both versions of the Hall thruster by considering electron diffusion toward the anode, the properties of the anode layer thruster can be simply approximated by considering a situation where the electron temperature increases as one approaches the anode with a potential jump

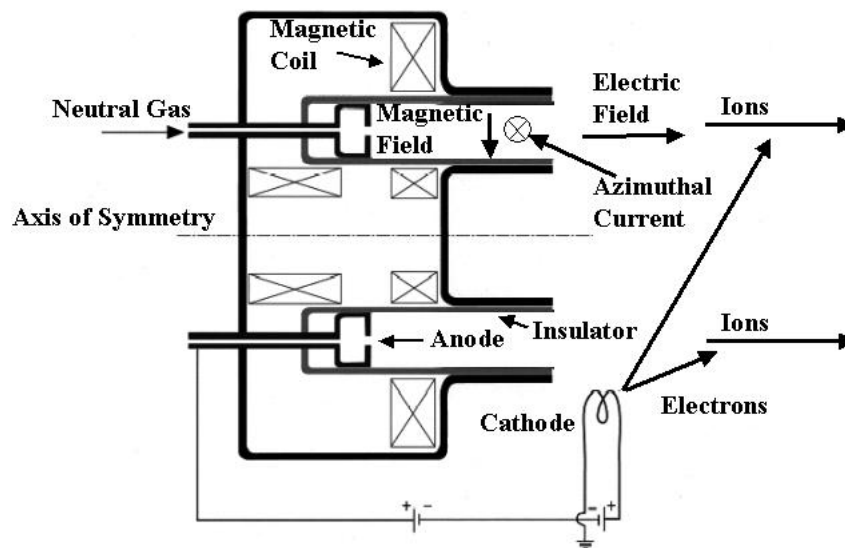


Figure A.2: Diagram of a Hall thruster as taken from Ref. [63].

occurring immediately in front of the anode, while in the Hall current thruster the electron temperature remains constant and the potential varies continuously throughout the acceleration region.

A version of the Hall current thruster called the Stationary Plasma Thruster (SPT), has been used on several Russian geo-stationary satellites, for station-keeping, over the past twenty years [4]. An SPT-140 Hall current thruster, developed by the Russian Design Bureau Fakel, has been selected by Space Systems/Loral for use on its new 20.20TM geo-stationary communications satellites for station-keeping and orbit-raising [77]. This thruster operates at 4.5 kW input power, using 16.2 mg/sec of xenon, with a measured specific impulse of 1640 sec, a thrust of 260 mN and an efficiency of 46 % [82]. A similar Hall current thruster, the BPT-4000, developed by General Dynamics Space Systems, is currently being qualified for use on the next generation of Lockheed Martin geo-stationary communications satellites [83, 84]. Anode layer thrusters have yet to be used commercially in space, but currently there are many research programs aimed at developing the technology further. A state-of-the-art anode layer thruster, operating in the 2 kW power range, developed by Busek as part of a NASA-funded initiative, has a specific impulse of 3100 sec and an efficiency of 55 % with an anode voltage as high as 900 V [85]. This device is similar to many others that have been built and tested by the Russian Design Bureau TsNIIMASH over the past twenty years. One such device, the D-80, which was recently tested by NASA, has a specific impulse of 3900 sec and an efficiency of 52 % at 8.7 kW of input power while delivering about 240 mN of

thrust at an anode voltage of 1700 V [86]. In addition another current NASA program involves the testing of a 50 kW anode layer thruster, designed to operate at discharges currents as high as 100 A, meant for future orbit-raising and interplanetary missions [87]. This thruster was recently tested at 26 kW input power, with the anode voltage at 650 V, and a specific impulse of 3200 sec was demonstrated at an efficiency of 67 % while delivering 1.1 N of thrust [88].

Given their relative state of maturity, and high efficiency in a useful specific impulse range, both Hall thrusters and ion engines have found a niche for orbit-raising applications on conventional geo-stationary satellites. It is likely that this role will be extended in the future, as spacecraft become more massive and more electrical power is made available. The performance of the electrical propulsion system, on these missions, is inextricably linked with the specific power of the electrical power generation system, in determining the maximum payload fraction achievable. For this reason the current state of the art for solar power generation is now reviewed.

A.4 Solar Power Technology

Solar power technology has evolved over forty years, during which time advances have been made in efficiency and specific power, making the geo-stationary communication satellites of today feasible. A solar cell utilizes the photovoltaic effect to convert sunlight into electricity, and is made from semiconductor materials, arranged in a series of layers. Solar cells are placed on a suitable support structure and connected together to form a solar array. An example of a contemporary geo-stationary satellite, that best illustrates the use of solar power technology for telecommunications, is the Boeing 702 model. Such a satellite, typically 3000 kg in mass, uses no less than 15 kW of power to operate more than a hundred communications transponders. This power requirement is met using a pair of thin film, multi-junction, solar arrays, that have a 27 % efficiency and a specific power of roughly 14 kg/kW. A fraction of the electrical power generated by the arrays is stored in nickel-hydrogen batteries, with a specific energy of 20 kg/kW h, for use during eclipse periods. Solar technology continues to develop, and current advances, such as improved multi-junction arrays, flexible membrane arrays, concentrator arrays, and lithium-ion batteries may be promising for future space missions.

The past decade has seen a steady increase in the efficiency of solar cells, as the traditional silicon cell was replaced with the multi-junction gallium arsenide cell. Modern multi-junction cells, such as those made by Boeing's Spectrolab Division and used on its 702 satellite models, are triple junction cells, consisting of layers of GaInP₂, GaAs and Ge semiconductors. These cells are typically 0.19 mm thick, and are mounted on a low-mass, graphite-epoxy, aluminum-honeycomb struc-

ture to form a panel [89]. The presence of a GaInP_2 layer in these cells offers a higher degree of radiation resistance, above what is possible with just GaAs/Ge or Si cells [90]. The latest multi-junction cells, themselves, are an improvement over bi-junction GaAs/Ge cells, first introduced a few years ago, whose efficiency was about 21 %, and cells with efficiencies greater than 30 % are now in development which could bring the array specific power down to 10 kg/kW [91].

Even greater increases in array specific power are possible, using the thin film, solar cells, arranged on flexible, membrane structures. The membranes could be as thin as $50\mu\text{m}$, constructed of flexible polymer materials, such as Kapton [90]. A prototype of such a system, using thin film, single-junction, GaAs/Ge cells, was built and tested on the ground, demonstrating a specific power of 7 kg/kW [90]. This array configuration uses a central mast and a wire tensioning system to keep the flexible membrane rigid. A recent study has been performed on a similar concept, with an inflatable tube replacing the central mast, and incorporating multi-junction solar cells, that would provide 1 megawatt of power for solar electric propulsion, as part of a future Mars mission [92].

Another approach for increasing the specific power of a solar array is to use lenses to concentrate sunlight onto the array. Such a concentrator array has been built and successfully demonstrated in space as part of NASA's Deep Space One mission [93]. The focusing optics on this array, known as SCARLET, are refractive Fresnel lenses, made from silicone, which provide a factor of eight concentration of the sunlight. The SCARLET array demonstrated a specific power of 22 kg/kW, producing 2.5 kW of power [93]. Subsequent work on this concept has led to the development of a next-generation 7 kW concentrator array, which is predicted to have a specific power of 5.6 kg/kW, based on initial testing of individual panels in the array [93]. If this system works as planned, than it could be another option for future solar electric propulsion missions requiring high power.

Solar cell technology has progressed from a state where the specific power of solar arrays, using silicon cells, was roughly 40 kg/kW ten years ago, to the thin film, multi-junction technology of today with a specific power of 14 kg/kW, representing almost a three-fold increase. More advances are likely in the near future [91], which may reduce the specific power even further, by almost a factor of two, making more electric propulsion missions feasible.

Another essential component in spacecraft power systems that augments the solar array is the energy storage system. Batteries are employed on contemporary satellites for this purpose, to supply power during eclipse periods of the orbit. For geo-stationary communications satellites, typically 12 % of the power generated by the solar arrays is used to recharge the batteries, but for low-earth orbit satellites 40 % or more is used, given the fact that low-earth orbit satellites undergo eclipses much more frequently [4]. Nickel-hydrogen batteries, which are commonly used on geo-stationary communication satellites, such as Boeing's model 702, have a

specific energy of typically 20 kg/kW h and lifetimes of 40,000 cycles at 60 to 80 % depth of charge [94, 95]. Even higher specific energies of about 7 kg/kW h, have been achieved with lithium-ion batteries, and a prototype rechargeable lithium-ion battery was demonstrated in space a few years ago [96]. Such batteries, with long cycle life, are now commercial items and they will undoubtedly be used on the next generation of communication satellites, increasing the power capacity even further.

With recent advances in solar cell and battery technology, the prospects for solar power in space look promising, but there are certain electric propulsion missions for which solar power is not ideal, including deep space missions to the outer planets. In these situations nuclear power may be the enabling technology.

A.5 Space-Based Nuclear Reactors

Realizing the potential of space-based nuclear power systems to enable deep space missions, many studies were done in the United States over the past forty years to assess the feasibility of such systems, and a few prototype systems were built and tested. In addition space-based nuclear reactors were developed in the former Soviet Union and used extensively on many of its low earth orbit, satellite reconnaissance missions. There is a rich heritage of work for future designers of space nuclear reactors. Several key technologies have been developed, including static power conversion systems, uranium metal matrix fuel elements, and liquid-metal cooling technology. The state-of-the-art in space-based nuclear reactor design is now reviewed, focusing on two reactor systems, the American SP-100, and the Russian Topaz I, and the historical developments which influenced their design.

The SP-100 space reactor program, carried out from 1983 to 1994, developed many nuclear reactor technologies for future space missions, including planetary surface operations and nuclear electric propulsion. This program built upon prior experience with space nuclear reactors in the United States, including a single space test of a reactor system in 1964, the SNAP-10A, involving a sodium-potassium (NaK) cooled reactor, with uranium zirconium-hydride (UZrH_x) fuel elements, using thermoelectric power conversion [97]. This system operated for about forty days, producing an average of 500 W of electrical power, and had a specific power of 870 kg/kW [98]. As part of SP-100 program, a 100 kW reactor was designed, representing a significant advance over the previous effort. Many of the components of this system were built and tested, but the complete SP-100 reactor was never assembled before the program ended in 1994. The 100 kW reactor design incorporates a lithium-cooled uranium reactor, using enriched uranium nitride (UN) fuel elements, and a thermoelectric power conversion system, external to the reactor, which converts the heat produced from the fission reactions directly into electricity [99]. Liquid lithium would have transported the heat generated inside the reac-

tor to the multi-cell thermoelectric converter. It was intended that the reactor and power conversion system would have been isolated from the rest of the spacecraft using a 22.5 m boom. The overall mass of the system would have been 4,575 kg, including radiation shield, giving a specific power of about 46 kg/kW, if everything worked as intended [99]. A key element of the SP-100 reactor design is the fact that the power conversion is done external to the reactor core, enabling different conversion systems to be used. In addition to thermoelectric conversion, dynamic conversion systems, such as Brayton and Stirling systems, were considered as well. A recent study suggests that a Brayton-cycle conversion system could reduce the specific power of an SP-100 type system to around 17.5 kg/kW, and could enable a one megawatt system to have a specific power of roughly 4 kg/kW [100]. A new NASA initiative to continue the development of space-based nuclear power was recently approved, and it is likely that many of these reactor technologies will now be revisited.

Unlike the American program, the Soviet space nuclear power program, produced several reactors which flew in space, and the Topaz I reactor was the most advanced of these. No less than 33 nuclear reactors were flown in low earth orbit by the former Soviet Union, from 1971 to 1989, for radar reconnaissance missions, and these systems were later boosted into a higher orbit for disposal [101]. Early Soviet space-based nuclear reactors had similar characteristics to the SNAP-10A, using thermoelectric power conversion, but the Soviet system used uranium carbide (UC_2) fuel elements, was radiation cooled and had a specific power of roughly 580 kg/kW [101]. Unlike the American program, the Soviets continued to develop flight models, eventually producing a system with uranium molybdenum (UMo) fuel elements, sodium-potassium (NaK) cooling and a specific power of around 80 kg/kW [101]. The majority of Soviet reactors flown in space were of this type, producing nearly five kilowatts of power. These reactors operated in space for more than a year in some cases. The latest and most advanced reactors were the Topaz-I reactors, of which two flew in space. These reactors differed from previous systems by using thermionic power conversion. Like thermoelectric power conversion, thermionic systems are static systems, but involve current emission from a heated electrode. Unlike the semiconductor materials used for thermoelectric converters, the electrode in a thermionic system can sustain high temperatures of close to 2000 K and therefore thermionic converters tend to have a higher efficiency. The Topaz I reactors used uranium oxide (UO_2) fuel elements, and had a specific power of around 50 kg/kW, producing 6 kW of electrical power [101].

Much work has been done internationally over the past forty years to develop space nuclear reactors, involving the development and flight verification of many critical elements, such as liquid-metal cooling systems, static power conversion systems, such as thermoelectric and thermionic converters, and uranium metal matrix fuels. Such systems with specific powers in the range of 50 kg/kW, are ma-

ture technology and could meet the requirements for electric propulsion missions involving several hundreds of kilowatts of power in the near future. In the long term, as larger reactors are developed, it is expected that the specific power will drop even further into the 10 kg/kW range or even less [97,100].

Appendix B

Orbit-Raising Mission Example

Orbit-raising, moving from a low-earth orbit (LEO) to a geo-stationary orbit (GEO), is one mission where electric propulsion systems could improve the payload mass fraction dramatically compared with conventional, chemical propulsion systems. This is true because orbit-raising generally requires a relatively large ΔV of between 3 to 4 km/sec, for LEO to GEO transfer starting from a circular, low earth orbit [8]. There have been several studies involving the use of electric propulsion for this kind of mission, all-electric transfer from LEO to GEO, and the results confirm that significant gains in payload mass fraction are possible [102,103]. To date the application of electric propulsion to the orbit-raising mission has involved the xenon ion propulsion system (XIPS) system described in Appendix A, in which case the maneuver is started from an elliptical transfer orbit, with an apogee greater than the radius of the final geo-stationary orbit and a perigee above the Van Allen radiation belt, and the XIPS is used to circularize the orbit. Studies have shown previously that this approach for LEO to GEO orbit-raising, using chemical propulsion to get into an elliptical transfer orbit and then electric propulsion to circularize the final orbit, can also lead to significant increases in payload mass fraction compared with the all-chemical approach [87, 104, 105]. With either nuclear or solar power systems that currently exist today, the full potential of electric propulsion for the orbit-raising mission could be realized, starting from a less energetic, circular, low-earth orbit. In this appendix the propulsion requirements for such an orbit-raising mission are outlined, by doing a simple analysis involving the integration of the equations of motion for the spacecraft.

The example mission considered here involves moving a 25000 kg payload, which may correspond to a next generation military communications satellite, or a habitat module for a civilian deep space mission, from a circular low earth orbit 200 km above the earth to a geo-stationary orbit, 36000 km above the earth. This idealized spacecraft consists of the payload, whose mass is denoted, M_p , and its propulsion system, a space electric power system, either a nuclear reactor or a large solar array, with mass, M_e , a propellant tank with mass, M_s , and the propellant,

whose total mass is M_f . The mass of the electric propulsion thruster and power processing system has been neglected, relative to the other masses, in this simple model. The total initial mass of the spacecraft is $M_0 = M_f + M_s + M_e + M_p$. It is assumed that the initial and final orbits of the spacecraft are coplanar, and no plane change occurs during the transfer. For such a problem it is convenient to work in polar coordinates. The equations that govern the motion of the spacecraft are [8]

$$T_r - \frac{G_e M}{r^2} = M \left(\ddot{r} - r\dot{\theta}^2 \right), \quad (\text{B.1})$$

$$T_\theta = M \left(r\ddot{\theta} + 2\dot{r}\dot{\theta} \right), \quad (\text{B.2})$$

where G_e is the product of the universal gravitational constant and the mass of the earth, M is the instantaneous mass of spacecraft, and T_r and T_θ are the components of thrust in the \hat{r} and $\hat{\theta}$ directions. In the above equations the dots refer to time derivatives, and \hat{r} points in the radial direction away from the center of the earth. For the case of constant thrust in the direction of motion, $T_r = 0$, and the equations of motion can be non-dimensionalized, in terms of the quantities, $\tau = t\sqrt{G_e/r_0^3}$, $\rho = r/r_0$ and $\nu = T_\theta r_0^2/MG_e$, where r_0 is the radius of the initial orbit, relative to the center of the earth. These two equations can then be combined into a single equation

$$\frac{d}{d\tau} \left(\rho^3 \frac{d^2 \rho}{d\tau^2} + \rho \right)^{1/2} = \nu \rho. \quad (\text{B.3})$$

This equation describes the time evolution of the orbital radius, when constant thrust is applied in the $\hat{\theta}$ direction.

The mass of the power supply for this mission is determined based on the power requirement for the electric propulsion system, and in this case is

$$M_e = \frac{T_\theta I_{sp} g_0 \alpha}{2\eta}, \quad (\text{B.4})$$

where α is the specific power of the power supply and η is the thrust efficiency of the propulsion system. In the example considered here, η is taken to be 0.5, which is representative, collectively, of the performance of arcjets, Hall thrusters and ion engines. The specific power of the power supply is chosen as 50 kg/kW, which is representative of the Topaz I space nuclear reactor and the SP-100 reactor design. A specific power in this range, or even better (40 kg/kW), could also be achieved using existing gallium arsenide solar arrays with lithium-ion batteries for energy-storage. The mass of the propellant tanks is estimated as $M_s = \beta M_{f0}$, where M_{f0} is the initial propellant mass and β is taken as 0.1 [4]. The final component in the spacecraft mass is the mass of the propellant, which at any given instant is $M_{f0} - \dot{m}t$.

For a given level of thruster performance, characterized by constant T_θ and I_{sp} , and starting from a circular, low-earth, orbit, with radius r_0 , the final orbital radius, $r_f(M_{f0})$, that can be achieved is a function of the initial propellant mass, M_{f0} . $r_f(M_{f0})$ can be determined by integrating Eqn. B.3. The mass required to achieve a final geo-stationary orbit with radius r_f^* is then the root of the equation, $r_f^* - r_f(M_{f0}) = 0$. A computer program was written to find this root, using the hybrid Newton-Raphson, bisection method [48]. In this program, Eqn. B.3 was numerically integrated using a fourth order Runge-Kutta algorithm [48].

Three cases were explored, using the above procedure, for different levels of constant thrust, where T_θ was set equal to 1, 10 or 100 N. For each thrust level, a range of specific impulse values were considered, from 500 to 6000 sec, to see the influence of specific impulse on the payload mass fraction. The results are plotted in Fig. B.1. For each thrust level the optimum payload mass fraction is indicated with a star, and the value of transfer time in Fig. B.3 corresponding to this point is so indicated as well. For the 100 N case a maximum payload fraction of 19.5 % is achieved at a specific impulse of 1020 sec, using 500 kW of electrical power. As the thrust level is reduced, the maximum payload fraction is shown to increase. For the 10 N case it is 55 %, at a specific impulse of 2040 sec, using 100 kW, and for the 1 N case the maximum payload fraction is 82 %, at a specific impulse of 5360 sec, using only about 26 kW. Another feature of the 1 N case is that once the specific impulse increases above about 3000 sec, there is little variation in the payload mass fraction, which here is around 80 %. If this curve were continued, further to the right, than the payload fraction would decrease sharply due to the increasing influence of the power supply mass at higher values of specific impulse. This point is illustrated for the 10 N case in Fig. B.2, where the propellant mass fraction, the power plant mass fraction, and their sum, are plotted as functions of specific impulse. The mass of the power supply increases linearly as the specific impulse increases, as expected for a constant level of thrust according to Eqn. B.4. The mass of the propellant decreases sharply as the specific impulse increases, and these two competing effects give rise to an optimum specific impulse, as shown in Fig. B.2, where the payload mass fraction is highest, 2040 sec in this case. One final point to examine, with this example problem, is the time required to complete the transfer to geo-stationary orbit for each of these three cases. This is shown in Fig. B.3, where it is evident that higher thrust levels enable shorter trip times. For the 100 N case, the transfer times are shortest, about 53 days for the optimum point as shown in Fig. B.3. As the thrust level is decreased to 10 N, the transfer time increases to around 215 days, near the corresponding optimum point for this thrust level at about 2040 sec. The longest transfer times of all occur for the 1 N case, where at the optimum point it takes about 1560 days (4.3 years) to complete the orbit transfer.

There is a trade-off between transfer time, and payload mass fraction. The

lower thrust missions, using smaller levels of power, have a higher optimum specific impulse, and a larger maximum payload fraction, but require longer periods of time to complete the orbital transfer.

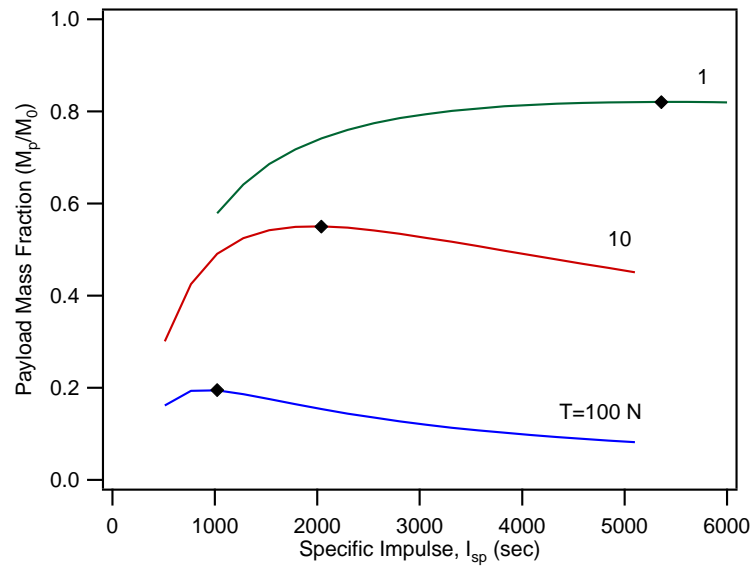


Figure B.1: Payload mass fraction as a function of specific impulse.

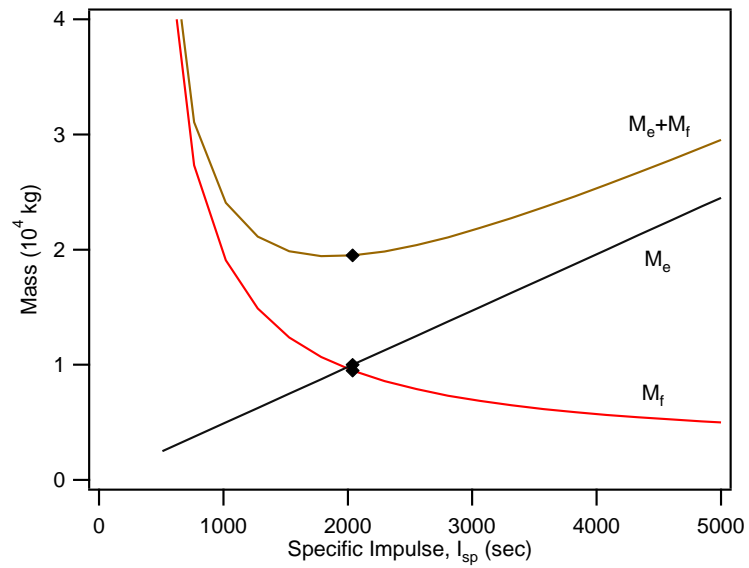


Figure B.2: Mass breakdown for the 10 N thrust case.

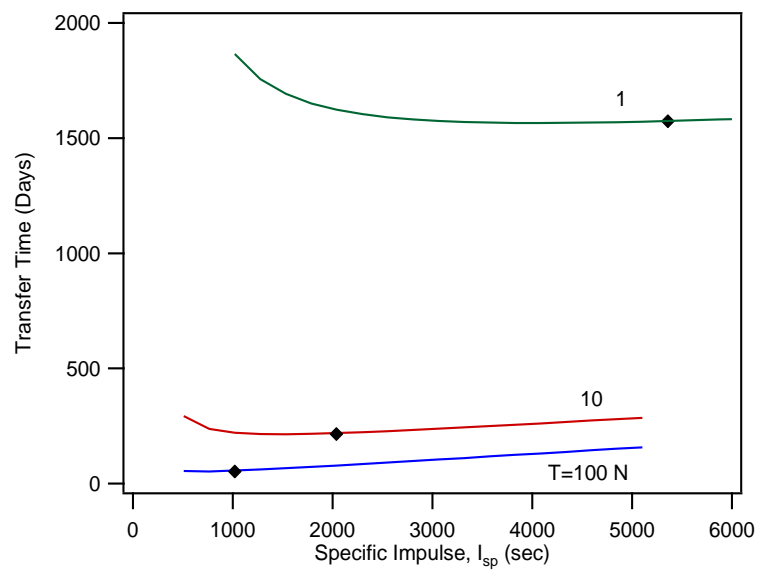


Figure B.3: Orbital transfer time as a function of specific impulse.

Bibliography

- [1] D.R. Jenkins. *Space Shuttle: The History of the National Space Transportation System*. Voyageur Press, 2001.
- [2] R.D. Launius and D.R. Jenkins. *To Reach the High Frontier: A History of U.S. Launch Vehicles*. University Press of Kentucky, 2002.
- [3] B.A. Smith. Eelv competitors seek to achieve performance goals. *Aviation Week and Space Technology*, 151(24):54–60, 1999.
- [4] M. Martinez-Sanchez and J.E. Pollard. Spacecraft electric propulsion - an overview. *Journal of Propulsion and Power*, 14:688–699, 1998.
- [5] S.K. Borowski, J.S. Clark, M.C. McIlwain, and D.G. Pelaccio. Nuclear thermal rockets- key to moon-mars exploration. *Aerospace America*, 30(7), 1992.
- [6] T.L. Kessler, P. Frye, and R. Partch. Solar thermal otv-applications to reusable and expendable launch vehicles. *Acta Astronautica*, 47:215–226, 2000.
- [7] G.R. Schmidt, J.A. Bonometti, and C.A. Irvine. Project orion and future prospects for nuclear pulse propulsion. *Journal of Propulsion and Power*, 18:497–504, 2002.
- [8] P. Hill and C. Peterson. *Mechanics and Thermodynamics of Propulsion*. Addison-Wesley, 1992.
- [9] K.D. Diamant, R.B. Cohen, and J.E. Brandenburg. High power microwave electrothermal thruster performance on water. In *38th AIAA Joint Propulsion Conference*, Indianapolis, IN, July 2002. AIAA-2002-3662.
- [10] M.C. Hawley, J. Asmussen, J.W. Filpus, S. Whitehair, C. Hoekstra, T.J. Morin, and R. Chapman. Review of research and development on the microwave electrothermal thruster. *Journal of Propulsion and Power*, 5:703–712, 1989.
- [11] S. Whitehair and J. Asmussen. Microwave electrothermal thruster performance in helium gas. *Journal of Propulsion and Power*, 3:136–144, 1985.

- [12] P. Balaam and M. M. Micci. Investigation of stabilized resonant cavity microwave plasmas for propulsion. *Journal of Propulsion and Power*, 11:1021–1027, 1995.
- [13] D. J. Sullivan and M. M. Micci. Development of a microwave resonant cavity electrothermal thruster prototype. In *23rd International Electric Propulsion Conference*, Seattle, WA, September 1993. IEPC-93-036.
- [14] D.J. Sullivan. Water based thrusters for space propulsion. Final Report SBIR SB021-20, DARPA, 2002.
- [15] S. Venkateswaran and C. L. Merkle. Numerical investigation of bluff-body stabilized microwave plasmas. *Journal of Propulsion and Power*, 11:357–364, 1995.
- [16] D.A. Schwer, S. Venkateswaran, and C. L. Merkle. Analysis of microwave-heated rocket engines for space propulsion. In *AIAA 29th Joint Propulsion Conference*, Monterey, CA, June 1993. AIAA 93-2105.
- [17] V. P. Chiravalle, R. B. Miles, and E. Y. Choueiri. Numerical simulation of microwave-sustained supersonic plasmas for application to space propulsion. In *39rd AIAA Aerospace Sciences Meeting*, Reno, NV, January 2001. AIAA-2001-0962.
- [18] S. A. Miller and M. Martinez-Sanchez. Two-fluid nonequilibrium simulation of hydrogen arcjet thrusters. *Journal of Propulsion and Power*, 12:112–119, 1996.
- [19] T.W. Megli, H. Krier, R.L. Burton, and A. Mertogul. Two-temperature plasma modeling of nitrogen/hydrogen arcjets. *Journal of Propulsion and Power*, 12:1062–1069, 1996.
- [20] M. Auweter-Kurtz, T. Golz, H. Habiger, F. Hammer, H. Kurtz, M. Riehle, and C. Slezonia. High-power hydrogen arcjet thrusters. *Journal of Propulsion and Power*, 14:764–773, 1998.
- [21] S. Gordon and B. J. McBride. Computer program for calculation of complex chemical equilibrium compositions and applications: Part 1 analysis. Reference Publication NASA-RP-1311, NASA Lewis Research Center, 1994.
- [22] D.J. Sullivan. *Development and Performance Characterization of a Microwave Electrothermal Thruster Prototype*. PhD thesis, Pennsylvania State University, 1995.
- [23] R. B. Miles, G. Brown, W. Lempert, R. Yetter, G. Williams, and S. Bogdonoff. Radiatively driven hypersonic wind-tunnel. *AIAA Journal*, 33:1463–1470, 1995.

- [24] P. Barker, P. Howard, B. Anderson, R. Miles, G. Brown, R. Lipinski, G. Pena, J. Grinstead, and R. Howard. Proof of principle energy addition experiments for the rdhwt/mariah ii hypersonic wind tunnel. In *21th AIAA Advanced Measurement Technology and Ground Testing Conference*, Denver, CO, June 2000.
- [25] D.R. Lide. *Handbook of Chemistry and Physics*. CRC Press, 2000.
- [26] S. Ramo, J.R. Whinnery, and T. Van Duzer. *Fields and Waves in Communications Electronics*. John Wiley & Sons, 1965.
- [27] B. McAndrew, J. Kline, J. Fox, D. Sullivan, and R. Miles. Supersonic vehicle control by microwave driven plasma discharges. In *40th AIAA Aerospace Sciences Meeting and Exhibit*, Reno, NV, January 2002.
- [28] R. Broglia, M. Manna, H. Deconinck, and G. Degrez. Development and validation of an axisymmetric navier-stokes solver for hypersonic flows. Technical Note 188, von Karman Institute for Fluid Dynamics, 1995.
- [29] M. Mitchner and C. H. Kruger. *Partially Ionized Gases*. John Wiley & Sons, 1973.
- [30] R.W. Crompton, M.T. Elford, and R.L. Jory. The momentum transfer cross section for electrons in helium. *Australian Journal of Physics*, 20:369–400, 1967.
- [31] D.E. Golden and H.W. Bandel. Low-energy e-ar total scattering cross sections: The ramsauer-townsend effect. *Physical Review*, 149:58–61, 1966.
- [32] L. Martinelli. *Calculations of Viscous Flows with a Multigrid Method*. PhD thesis, Princeton University, 1987.
- [33] G.L. Brown, A.P. Ratta, R.W. Anderson, L. Martinelli, W.R. Lempert, and R.B. Miles. Fluid mechanics in a radiatively driven hypersonic wind-tunnel - prediction and preliminary experiment. In *19th AIAA Advanced Measurement and Ground Testing Technology Conference*, New Orleans, LA, June 1996. AIAA-96-2199.
- [34] A. Jameson. Multigrid algorithms for compressible flow calculations. In *Multigrid Methods II: Proceedings of the 2nd European Conference on Multigrid Methods*, Koln, Germany, 1986. pg. 166-201.
- [35] S. Tatsumi, L. Martinelli, and A. Jameson. Flux-limited schemes for the compressible navier-stokes equations. *AIAA Journal*, 33:252–261, 1995.
- [36] A. Jameson. Positive schemes and shock modeling for compressible flows. *International Journal for Numerical Methods in Fluids*, 20:743–776, 1995.

- [37] J.C. Tannehill, D.A. Anderson, and R.H. Pletcher. *Computational Fluid Mechanics and Heat Transfer*. Taylor & Francis, 1997.
- [38] S.G. Sheffer. *Parallel Computation of Supersonic Reactive Flows with Detailed Chemistry Including Viscous and Species Diffusion Effects*. PhD thesis, Princeton University, 1997.
- [39] H.W. Darwin and F. Emard. Influence of atom-atom collisions on the collisional-radiative ionization and recombination coefficients of helium plasmas. *Zeitschrift fur Physik*, 254:202–217, 1972.
- [40] J. Vlcek. A collisional-radiative model applicable to argon discharges over a wide range of conditions. *Journal of Physics D: Applied Physics*, 22:623–631, 1989.
- [41] M.A. Biondi and L.M. Chanin. Mobilities of atomic and molecular ions in the noble gases. *Physical Review*, 94:910–916, 1954.
- [42] Y. Shiu and M.A. Biondi. Dissociative recombination in argon: Dependence of the total rate coefficient and excited-state production on electron temperature. *Physical Review A*, 17:868–872, 1978.
- [43] J.F. Lowry, D.H. Tomboulion, and D.L. Ederer. Photoionization cross section of helium in the 100 to 250 Å region. *Physical Review*, 137:1054–1057, 1965.
- [44] L.L. Alves, G. Gousset, and C.M. Ferreira. A collisional-radiative model for microwave discharges in helium at low and intermediate pressures. *Journal of Physics D: Applied Physics*, 25:1713–1732, 1992.
- [45] Y. P. Raizer. *Gas Discharge Physics*. Springer-Verlag, 1997.
- [46] L.C. Pitchford, S.V. O'Neil, and J.R. Rumble Jr. Extended boltzmann analysis of electron swarm experiments. *Physical Review A*, 23:294–304, 1981.
- [47] Z. Tang and R. B. Miles. One and two photon optogalvanic spectroscopy of argon and neon for the wavelength calibration in the near infrared. *Optics Communications*, 184:411–416, 2000.
- [48] W.H. Press, S.A. Teukolsky, W.T. Vetterling, and B.P. Flannery. *Numerical Recipes in Fortran 77: The Art of Scientific Computing*. Cambridge University Press, 1986.
- [49] L.D. Landau and E.M. Lifshitz. *Quantum Mechanics: Non-Relativistic Theory*. Pergamon Press, 1977.

- [50] W.L. Wiese, M.W. Smith, and B.M. Glennon. *Atomic Transition Probabilities: Volume 1 Hydrogen Through Neon*. U.S. Department of Commerce, National Bureau of Standards, 1966.
- [51] W.L. Wiese, M.W. Smith, and B.M. Miles. *Atomic Transition Probabilities: Volume 2 Sodium Through Calcium*. U.S. Department of Commerce, National Bureau of Standards, 1969.
- [52] J.O. Hirshfelder, C.F. Curtiss, and R.B. Bird. *Molecular Theory of Gases and Liquids*. John Wiley & Sons, 1954.
- [53] R.B. Bird, W.E. Stewart, and E.N. Lightfoot. *Transport Phenomena*. John Wiley & Sons, 1960.
- [54] J.N. Reddy. *The Finite Element Method in Heat Transfer and Fluid Dynamics*. CRC Press, 1994.
- [55] J.D. Anderson. *Modern Compressible Flow with Historical Perspective*. McGraw-Hill, 1990.
- [56] H. Schlichting. *Boundary Layer Theory*. McGraw-Hill, 1979.
- [57] F. M. White. *Viscous Fluid Flow*. McGraw-Hill, 1974.
- [58] F.J. Souliez, S.G. Chianese, G.H. Dizac, and M. M. Micci. Low-power microwave arcjet testing: Plasma and plume diagnostics and performance evaluation. In *35th AIAA Joint Propulsion Conference*, Los Angeles, CA, June 1999. AIAA-99-2717.
- [59] R. B. Miles and M. Zimmermann. Hypersonic helium flow field measurements with the resonant doppler velocimeter. *Applied Physics Letters*, 37:885–887, 1980.
- [60] R. B. Miles, C. Cohen, J. Connors, P. Howard, S. Huang, E. Markovitz, and G. Russell. Velocity measurements by vibrational tagging and fluorescent probing of oxygen. *Optics Letters*, 12:861, 1987.
- [61] D. Keefer and R.M. Ruyten. 2-beam multiplexed laser-induced-fluorescence measurements of an argon arcjet plume. *AIAA Journal*, 31:2083–2089, 1993.
- [62] S.H. Zaidi, Z. Tang, A.P. Yalin, P. Barker, and R. B. Miles. Filtered thomson scattering in an argon plasma. *AIAA Journal*, 40:1087–1093, 2002.
- [63] R.G. Jahn and E.Y. Choueiri. Electric propulsion. *Encyclopedia of Physical Science and Technology, Third Edition*, 5:125–141, 2002.

- [64] R.G. Jahn. *Physics of Electric Propulsion*. McGraw-Hill, 1968.
- [65] E. Stuhlinger. *Ion Propulsion for Space Flight*. McGraw-Hill, 1964.
- [66] R.L. Burton, K.E. Clark, and R.G. Jahn. Measured performance of a multi-megawatt mpd thruster. *Journal of Spacecraft and Rockets*, 20:299–304, 1983.
- [67] E.Y. Choueiri and J.K. Ziemer. Quasi-steady magnetoplasmadynamic thruster performance database. *Journal of Propulsion and Power*, 17:967–976, 2001.
- [68] J.E. Polk. *Mechanisms of Cathode Erosion in Plasma Thrusters*. PhD thesis, Princeton University, 1996.
- [69] J.K. Ziemer. *Performance Scaling of Gas-Fed Pulsed Plasma Thrusters*. PhD thesis, Princeton University, 2001.
- [70] R.L. Burton and P.J. Turchi. Pulsed plasma thruster. *Journal of Propulsion and Power*, 14:716–735, 1998.
- [71] M. Birkan. Arcjets and arc heaters: An overview of research status and needs. *Journal of Propulsion and Power*, 12:1011–1017, 1996.
- [72] R.R. John, S. Bennett, and J.F. Connors. Arcjet engine performance: Experiment and theory. *AIAA Journal*, 1:2517–2525, 1963.
- [73] P. G. Lichon and J. M. Sankovic. Development and demonstration of a 600-sec mission-average i_{sp} arcjet. *Journal of Propulsion and Power*, 12:1018–1025, 1996.
- [74] F.M. Curran. Electric propulsion activities in u.s. industry. In *26th International Electric Propulsion Conference*, Kitakyushu, Japan, October 1999. IEPC-99-001.
- [75] D.R. Bromaghim, J.R. LeDuc, R.M. Salasovich, J.A. Zimmerman, D.C. Matias, A.M. Sutton, G.G. Spanjers, J.M. Fife, W.H. Hargus, R.A. Spores, M.J. Dulligan, S.F. Engelman, J.H. Schilling, D.C. White, and L.K. Johnson. An overview of on-orbit results from the electric propulsion space experiment (esex). In *26th International Electric Propulsion Conference*, Kitakyushu, Japan, October 1999. IEPC-99-182.
- [76] S. Nakanishi and E.V. Pawlik. Experimental investigation of a 1.5 m diameter kaufman thruster. *Journal of Spacecraft and Rockets*, 5:801, 1968.
- [77] R.M. Myers. Overview of major u.s. industrial programs in electric propulsion. In *36th AIAA Joint Propulsion Conference*, Huntsville, AL, July 2000. AIAA-2000-3147.

- [78] J.E. Polk, D. Brinza, R.Y. Kakuda, J.R. Brophy, I. Katz, J.R. Anderson, V.K. Rawlin, M.J. Patterson, J. Sovey, and J. Hamley. Demonstration of the nstar ion propulsion system on the deep space one mission. In *27th International Electric Propulsion Conference*, Pasadena, CA, October 2001. IEPC-01-075.
- [79] V.K. Rawlin, L.R. Pinero, G.J. Williams, and R.F. Roman. Status of ion engine development for high power, high specific impulse missions. In *27th International Electric Propulsion Conference*, Pasadena, CA, October 2001. IEPC-01-096.
- [80] H.R. Kaufman. Theory of ion-acceleration with closed electron-drift. *Journal of Spacecraft and Rockets*, 21:558–562, 1984.
- [81] H.R. Kaufman. Inert-gas thruster technology. *Journal of Spacecraft and Rockets*, 20:77–83, 1983.
- [82] D. Manzella, C. Sarmiento, J. Sankovic, and T. Haag. Performance evaluation of the spt-140. In *25th International Electric Propulsion Conference*, Cleveland, OH, August 1997. IEPC-97-059.
- [83] J. Fisher, A. Wilson, D. King, S. Meyer, C. Engelbrecht, K. de Grys, and L. Werthman. The development and qualification of a 4.5 kw hall thruster propulsion system for geo satellite applications. In *27th International Electric Propulsion Conference*, Pasadena, CA, October 2001. IEPC-01-010.
- [84] K. de Grys, N. Meckel, G. Callis, D. Greisen, A. Hoskins, D. King, F. Wilson, L. Werthman, and V. Khayms. The development and testing of a 4500 watt flight type hall thruster and cathode. In *27th International Electric Propulsion Conference*, Pasadena, CA, October 2001. IEPC-01-011.
- [85] B. Pote and R. Tedrake. Performance of a high specific impulse hall thruster. In *27th International Electric Propulsion Conference*, Pasadena, CA, October 2001. IEPC-01-035.
- [86] D.T. Jacobson, R.S. Jankovsky, V.K. Rawlin, and D.H. Manzella. High voltage tal performance. In *37th AIAA Joint Propulsion Conference*, Salt Lake City, UT, July 2001. AIAA-2001-37777.
- [87] S.R. Oleson and J.M. Sankovic. Advanced hall electric propulsion for future in-space transportation. In *Third International Spacecraft Propulsion Conference*, Cannes, France, October 2000.
- [88] R.R. Hofer and R.S. Jankovsky. A hall thruster performance model incorporating the effects of a multiply-charged plasma. In *37th AIAA Joint Propulsion Conference*, Salt Lake City, UT, July 2001. AIAA-2001-3322.

- [89] J.C. Garner. Clementine gallium arsenide/germanium solar array. *Journal of Propulsion and Power*, 12:847–851, 1996.
- [90] H.W. Brandhorst, P.R.K. Chetty, M.J. Doherty, and G.L. Bennett. Technologies for spacecraft electric power systems. *Journal of Propulsion and Power*, 12:819–827, 1996.
- [91] G.A. Landis, S.G. Bailey, and M.F. Piszczor. Recent advances in solar cell technology. *Journal of Propulsion and Power*, 12:835–841, 1996.
- [92] L.S. Mason and S.R. Oleson. Spacecraft impacts with advanced power and electric propulsion. TM 2000-209912, NASA, 2002.
- [93] M.J. O'Neill, A.J. McDanal, P.J. George, M.F. Piszczor, D.L. Edwards, D.T. Hoppe, M.I. Eskenazi, M.M. Botke, P.A. Jaster, and H.W. Brandhorst. Development of the ultra-light stretched lens array. In *29th IEEE Photovoltaics Specialists Conference*, New Orleans, LA, May 2002.
- [94] J.J. Smithrick and P.M. O'Donnell. Nickel-hydrogen batteries - an overview. *Journal of Propulsion and Power*, 12:873–878, 1996.
- [95] S.J. Stadnick and H.H. Rogers. 26 % potassium hydroxide koh electrolyte for long-term nickel-hydrogen geosynchronous missions. *Journal of Propulsion and Power*, 12:893–896, 1996.
- [96] H.F. Bittner and M.J. Mildner. Development and flight of a 250-ah lithium thionyl chloride battery. *Journal of Propulsion and Power*, 12:897–900, 1996.
- [97] J.A. Angelo and D. Buden. *Space Nuclear Power*. Orbit Book, 1985.
- [98] G.L. Bennett, R.J. Hemler, and A. Schock. Space nuclear power: An overview. *Journal of Propulsion and Power*, 12:901–910, 1996.
- [99] A.T. Josloff, N.F. Shepard, T.S. Chan, F.C. Greenwood, N.A. Deane, J.D. Stephen, and R.E. Murata. Sp-100 generic flight system design and early flight options. In *11th Symposium on Space Nuclear Power and Propulsion*, Albuquerque, NM, January 1994.
- [100] L.S. Mason. A comparison of brayton and stirling space nuclear power systems for power levels from 1 kilowatt to 10 megawatts. TM 2001-210593, NASA, 2001.
- [101] G.L. Bennett. A look at the soviet space nuclear power program. In *24th IEEE Intersociety Energy Conversion Engineering Conference*, Washington, DC, August 1989.

- [102] H.R. Kaufman and R.S. Robinson. Electrical thruster performance for orbit raising and maneuvering. *Journal of Spacecraft and Rockets*, 21:180–186, 1984.
- [103] R.M. Jones. Comparison of potential electric propulsion systems for orbit transfer. *Journal of Spacecraft and Rockets*, 21:88–95, 1984.
- [104] S.R. Oleson, R.M. Myers, C.A. Kleuver, J.P. Riehl, and F.M. Curran. Advance propulsion for geostationary orbit insertion and north-south station keeping. *Journal of Spacecraft and Rockets*, 34:22–28, 1997.
- [105] S.R. Oleson. Advanced electric propulsion for rlv launched geo-synchronous spacecraft. In *26th International Electric Propulsion Conference*, Kitakyushu, Japan, October 1999. IEPC-99-185.